A multi-wavelength study of protoplanetary disks with astronomical unit resolution

Narges Jamialahmadi

UNIVERSITÉ NICE SOPHIA ANTIPOLIS
Eole Doctorale de Sciences Fondamentales et Appliquées
European Southern Observatory (ESO)

T H E S E

pour obtenir le titre de

Docteur en Sciences

de l'UNIVERSITE Nice Sophia Antipolis

de l'ESO

Discipline : SCIENCES DE L'UNIVERS

présentée et soutenue par

Narges JAMIALAHMADI

Une étude multi longueur d'onde des disques protoplanétaires à l'échelle de l'unité astronomique

A multi-wavelength study of protoplanetary disks with astronomical unit resolution

Thèse dirigée par: Bruno Lopez, Philippe Berio

Thèse dirigée a l'ESO par: Jean-Philippe Berger

Soutenue le 16 Décembre

Jury:

Président :	Alessandro Morbidelli	Directeur de Recherche, Lagrange, OCA
Rapporteurs :	Jean-Francois Gonzalez	Maître de Conférence, Observatoire de Lyon
	Stefan Kraus	Professeur Associé, University of Exeter
Examinateur :	Jean-Philippe Berger	Directeur de Recherche, ESO
Directeur de thèse :	Bruno Lopez	Directeur de Recherche, Lagrange, OCA
Co-Directeur de thèse :	Philippe Berio	Ingénieur de Recherche, Lagrange, OCA

Abstract

Planetary systems are born in circumstellar gas and dust disks surrounding Young Stellar Objects (YSOs). To understand how planetary systems form, a detailed knowledge of the structure and evolution of these disks is required. Although, this is almost well understood for the regions of the disks observed with a spatial resolution of several AUs, the structure of these disks probed at a few AU scale and especially inward of 1 AU remains a puzzle. In recent years, it has become possible to directly spatially resolve the inner region of protoplanetary disks with optical interferometry technique. The context of this thesis is a multi-wavelength investigation of the protoplanetary disks evolution by determining their density distribution, their temperature distribution, the size and composition of the dust components and finally the kinematics of the gas. I have developed my thesis following three complementary wavelength domains: study of the photosphere of the star and its nearby gaseous disk through visible interferometry, study of the radial and vertical structure of the inner rim of a pre-transitional disk at fractions of an AU through near-IR interferometry, and, the characterization of the disk regions at a few AUs from the central star through spectroscopic and mid-IR interferometry.

To analyse the visible-, near- and mid-IR interferometric observations, I have focused my attention on three well known sources, 51 OPh, HD 100546 and MWC 480 respectively that they have not been observed in these wavelengths. Visible interferometric observations can probe the photosphere of a resolved source in the continuum as well as the geometry and the kinematics of the gaseous disk producing the Hα line or Ca II triplet line on sub-AU scale. These observations allow to derive the stellar parameters, e.g, diameter, mass, temperature and to constrain the extension of the emission line and to understand the physical process of the gas such as accretion/outflow mechanism nearby the central star. Near-IR interferometric observations probe the hot gas and dust distribution at a fraction of an AU from the central star and allow to understand the kinematics of the gas as well as hot dust properties and its physical mechanism for the disk evolution and planet formation. Mid-IR interferometric observations mostly probe warm dust from the most inner region up to a few AU and allow to investigate the dust properties and in their emission regime.

Acknowledgements

This thesis would not have done without helps of people around me during my stay in Nice and Munich. In the first day of my arrival to Nice in 2th December 2011, the first person I met in the airport was Bruno Lopez, one of my advisors. Based on the way of his behaviour (kindness) in the first day, I considered him like a father who is so supportive. I felt that I am so convenient to talk to him about work or any other topics. Then, I came to know with Philippe Berio my another supervisor. I think every one has at least one sample in her/his life. During my PhD, Philippe for me was a sample of kindness and patience, an understanding person who never considered my weakness but my strengths. My questions never stopped him answering me and he was a person who motivated me to keep doing my research.

This research has largely benefited from the advices of my colleague Olivier Chesneau, who passed away last spring. I wish to acknowledge his help.

Thanks Philipe Berio, step by step, I started working with VEGA group in Nice and I found them so friendly. I learnt lots of things about observations since I never had any experiences on observations before coming to Nice. Beside my supervisors, working with A. Meilland, N. Nardetto, Ph. Stee and others in VEGA group motivated me to work on YSOs and stellar physics more than before. I am mostly grateful to Anthony Meilland for all his helps in VEGA observations and teaching me to use his code during my thesis. Thanks to planetology group, A. Morbidelli, A. Crida, P. Tanga, Alexis Matter and others in this group for useful discussions. I appreciate all helps of Sebastien Flament during my thesis helping me in writing numerical codes. I express my gratitude to Thorsten Ratzka in the last year of my PhD. I am always grateful of M. Vennier, F. Millour, S. Lagarde, T. Lanz, F. Vakili and E. Fossat for many useful discussions during these years. During these three years in Nice, I got many friends with whom I could share my happiness and some times problems of my life and work. I am really grateful of my friends (their names in order of coming to know them): Sibilla, Masinissa, Wassilla, Suvendu, Arwa, Aurelie, Korhan, Laurent, Kaveh, Judit, Mamadu, Sinan, Zeinab, Samir, Husne, Onelda, Alkis, Gaetan, Alvaro, Sarunas, Reda, Srivatsan and many others friends.

It was a pleasure to be officemate with Suvendu, Roxanne, Carolyne and Laurence. Our warm and friendly chatting (even in French) was inducing lots of positive energies to me.

I do thank Nathalie, Michel and Khaled, Karima, Nadia and others in canteen whom their smiles and their great foods were boosting my energy to keep woking.

In the last year of my PhD, I got accepted for ESO studentship and started working with Jean-Philippe Berger. Thanks to him I learnt a lot of things concerning radiative transfer code and PIONIER/VLTI. The beginning days of arriving to cold Munich was hard to me to be far from all my belongs in Nice, but I found him friendly that I felt comfortable to chat with him about works and other topics. I am really grateful of Andrea Chiavassa who did lots of helps either code problems or other useful discussions for my future career during the first month of my staying at ESO. Thanks Marco Di Pascal who helped me the first days of arrival to Garching to introduce me to PhD and fellows at ESO. I really appreciate all useful chats with my Iranian friends, Maryam, Mahsa, Ghazale, Masuod and Mohammad at MPE. During these years, I never forget supports of my loves, i.e., my parents, sisters and brothers.

The most my greatest acknowledge to Juries to take time and review my thesis and attend to my defence.

A the end, I strongly appreciate my efforts to overcome most of problems I faced during these years at OCA and at ESO.

'The first rule is to have vision for your life,
'the second is to believe in your ability to figure things out,
'the third is to be patient but always persistent,
'the forth is to respect and love other people.'
–Narges

Dedicated to
My parents, sisters and brothers

Contents

List of Figures

List of Tables

Résumé

Dans ma thèse, j'étudie les environnements circumstellaires autour des étoiles jeunes basé les observations interférométriques à haute résolution. Mon objectif est d'améliorer notre compréhension de la structure et de l'évolution des disques circumstellaires en déterminant leur distribution de densité, leur distribution de température, la taille et de la composition de la poussière et la cinématique et de lévolution du gaz. J'ai développé ma thèse suivant trois domaines de longueur d'onde complémentaires: étude de la photosphère de l'étoile et de son disque gazeux à proximité grâce à l'interférométrie visible, étude de la structure radiale et verticale du bord intern du disque pré-transition à une fraction d'UA au travers de interférométrie infrarouge, et la caractérisation des régions du disques entre des fractions d'UA jusqu'à quelques UA de l'étoile centrale par spectroscopique et interférométrie du moyen infrarouge.

Pour analyser les observations, j'ai utilisé plusieurs types de modèles et d'outils numériques: J'ai utilisé le logiciel d'ajustement de modèles LITpro2 développé par le Jean-Marie Mariotti Center (JMMC) pour interpréter les données interférométriques visibles dans le continuum. Pour interpréter les données interférométriques visibles des raies spectrale, j'ai utilisé un modèle cinématique d'un disque équatoriale mince en expansion et /ou en rotation. Ce modèle a déjà été utilisé pour certaines étoiles Be classiques et décrite en détail par M. Delaa et al. (2011). J'ai utilisé avec succès un code de transfert radiatif Monte-Carlo, MCFOST, pour modéliser la poussière dans la structure interne d'un disque de pré-transition et interpréter les données interférométriques en bande proche infrarouge H. Jai développé une méthodologie pour calculer les observables interférométriques à partir des images simulées de MCFOST. J'ai également développé un outil de modélisation semi-analytique. Ces modèles simule l'émission de disque en supposant différentes possibilités de géométrie et d'opacités de poussière et ont comparé lles données aux prévisions des modèles. Avec ces modèles, j'ai interprétér les observations proche et moyen infrarouge.

Dans le chapitre 1, je détaille un aperçu scientifique de l'origine des disques protoplanétaires et de leur volution.

Le chapitre 2 décrit les bases de l'interférométrie, les quantités mesurables et présente des techniques de modélisation utilisées pour analyser les observations interférométriques.

Dans le chapitre 3, je décris l'analyse des observations interférométriques d'une étoile en rotation rapide 51 Oph. Dans ce travail, j'en déduisais, pour la première fois,

l'extension et l'aplatissement de la photosphère de 51 Oph . En outre, en utilisant des mesures spectro-interférométrique dans la raie H alpha, j'ai contraint la géométrie et la cinématique de l'environnement circumstellaire et ai montré que l'émission est produite par une rotation képlérienne.

Dans le chapitre 4, je discute du bord intérieur du disque interne de pré-transition de HD 100546. En utilisant des données PIONIER uniques et un code de transfert radiatif 3D appelé MCFOST, je conclus que le bord intérieur du disque interne de cet objet n'est pas lisse mais grumeleux. L'existence d'asymétrie dans le bord intérieur du disque interne est évidente à partir du graphe de clôture de phase, qui ne peut être reproduite par les modèles de transfert radiatif symétriques.

Dans le chapitre 5, je décris la structure de la partie la plus interne du disque circumstellaire des étoiles Herbig MWC 480 combinant les données Keck proche infrarouge et MIDI mid-IR. Je premier, pensé sur l'effet de la variabilité proche infrarouge sur la SED et les visibilités Keck et MIDI. Je trouve que l'état maximum ou minimum luminosité de MWC 480 affecte sur les visibilités en particulier l'un Keck. L'effet sur le SED est significatif que pour les longueurs d'onde 2–20 μm. Pour l'état de luminosité maximale dans le proche infrarouge, la valeur des visibilités Keck est inférieure de l'etat au minimum un. Pour une visibilité MIDI, l'effet de la variabilité est moins importante que le proche infrarouge visibilité d'un. Toutefois, pour l'état de luminosité minimale, le disque dans le mi-IR est plus résolu que pour l'état un minimum. Dans ce chapitre, je propose plusieurs modèles pour reproduire le SED, le Keck et les données MIDI simultanément. Un modèle de disque à deux composants comprenant un disque interne optiquement mince et un disque externe optiquement épaisse peut reproduire mes données. Dans un modèle de disque composant, augmentant l'émission IR quasi en explorant tous les paramètres libres jusqu'à l'état de luminosité maximale était même pas compatible avec la SED dans les longueurs d'onde plus longues. En fait, le second composant du disque contribue principalement à l'émission à des longueurs d'onde plus longues.

Dans le chapitre 6, de nouvelles observations pousse mon étude de particulier certains récent Very Large Telescope Interferometer (VLTI) / données MIDI acquis en Décembre 2013 pour Herbig étoiles MWC 480. L'utilisation de modèles symétriques pour le disque pourrait ne pas reproduire simultanément toutes mes données: la Spectral distribution d'énergie, les données du proche infrarouge interféromètre Keck et les données de l'infrarouge moyen obtenu avec l'instrument MIDI. Afin d'expliquer toutes les mesures et en supposant que la structure du disque de MWC480 n'a pas varié avec le temps, l'utilisation de modèles asymétriques semble nécessaire. Plusieurs scénarios sont testés, l'un étant la présence d'un élément lumineux azimutal, dans la partie intérieure du modèle du disque, fournit un bon ajustement des données.

Enfin, dans le chapitre 7, nous résumons les principaux résultats discutés dans la thèse et nous discutons d'éventuelles nouvelles observations.

Introduction

The aim of this thesis is to study the structure of circumstellar disks around YSOs. Taking advantage of high spatial resolution interferometric observations I have focused my attention on the gas and dust properties in the inner disk, at fractions of AU and few AUs from the central star. The thesis is presented in five Chapters:

Chapter 2 describes the basics of intererferometry, the measurable quantities and a presentation of the modelling techniques used to analyse interferometric observations.

In Chapter 3, I describe the analysis of interferometric observations of a fast rotating star called 51 Oph. In this work, I derived, for the first time, the extension and flattening of 51 Oph photosphere. Furthermore, using spectro-interferometric measurements in the Hα line, I constrain the circumstellar environment geometry and kinematics and show that the emission is produced in a Keplerian rotation.

In Chapter 4, I discuss the inner rim of the inner disk of pre-transitional disk of HD 100546. Using my unique PIONIER data and a 3D radiative transfer code called MCFOST, I conclude that the inner rim of the inner disk of this object is not smooth and clumpy. The existence of asymmetry in the inner rim of inner disk is obvious from the closure phase plot, which can not be reproduced by symmetrical radiative transfer models.

In Chapter 5, I describe the structure of the innermost part of circumstellar disk of Herbig star MWC 480 combining Keck near-IR and MIDI mid-IR data. I first, figured out the effect of near-IR variability on the SED and the Keck and MIDI visibilities. I found that the maximum or minimum brightness state of MWC 480 affects on the visibilities especially the Keck one. The effect on the SED is significant only for wavelengths 2–20 μm. For the maximum brightness state in the near-IR, the value of the Keck visibilities is less than of the minimum state one. For MIDI visibility, the variability effect is less significant than near-IR visibility one. However, for the minimum brightness state, the disk in the mid-IR is more resolved than for the minimum state one. In this Chapter, I propose several models to reproduce the SED, the Keck and

the MIDI data simultaneously. A two-component disk model including an optically thin inner disk and an optically thick outer disk can reproduce my data. In one component disk model, increasing the near- IR emission by exploring all free parameters until maximum brightness state even was not consistent with the SED in the longer wavelengths. In fact, the second component of the disk mostly contributes to the emission at longer wavelengths.

In Chapter 6, new observations drives my study of particular some recent Very Large Telescope Interferometer (VLTI)/MIDI data acquired in December 2013 for Herbig star MWC480. The two-components disk model that we used to reproduce our previous data in Chapter 5 could not reproduce simultaneously all my data : the Spectral Energy Distribution, the near-infrared Keck Interferometer data and the mid-infrared data obtained with the MIDI instrument. In order to explain all measurements and assuming that the structure of the disk of MWC480 has not varied with time, one possibility is to add an azimuthal asymmetry in the inner disk of MWC 480. Several scenarios are tested, the one considering the presence of an azimuthal bright feature, in the inner component of the disk model, provides a good fit of the data.

Chapter 7, summarizes the main results discussed in the thesis and we discuss possible future new observations and developments.

Chapter 1

Scientific overview

The planets in our solar system are rotating around the sun since they have formed. But this does not mean that their conditions have always been like they are now. They all rotate around their host star in a roughly same plane and same orientation. This raises several questions about how our solar system came into existence, how it has evolved and how it will end up. Do all stars in the night sky have planets like the planets in our solar system? If yes, how do they look like? Are some of them habitable like our earth?

To answer all these questions, we need a precise knowledge on physics of our solar system as well as other stars and their circumstellar environment using a wide range of observations with the highest resolution possible. But we are aware that the formation and evolution of a system similar to our solar system can not be tracked with the short human life. However, we know that star and planet formation is not something that happened only in the past. In some specific regions in the sky star formation is expected to occur. Stars are made of gas and they form from the Interstellar Medium (ISM) in galaxies. In our galaxy, the material available for star formation is mostly observed as molecular gas in the ISM located in giant clouds. These molecular clouds are low density and cold ($\sim$ 10 K) and made of gas and dust where the gas dominates the mass (99 %) (Birnstiel et al., 2010). Stars are expected to form when the gas and dust in the clouds undergo gravitational collapse.

1.1 Star formation

A standard model of the star formation process from cold and relatively dense molecular clouds (mostly H_2 gas) can be divided into four phases (Shu et al., 1987). These phases are illustrated in Fig. 1.1. The first phase or class, starts with collapsing a molecular

cloud when its density exceeds a certain critical value due to external factors, and thermal and magnetic pressures can not balance against the gravitational **force** any longer (Class 0, t=0, Fig. 1.1). In this class, the cold material radiates in the far-infrared at a wavelength of around 300 μm, creating a Spectral Energy Distribution (SED) that is very red in color. To conserve the angular momentum, the rotating core is transformed into a young stellar object, which is surrounded by a disk-like structure with an extended spherical envelope (Class I, Fig. 1.1). In this class, the luminosity from the central star heats up the inner regions. These will start to emit in the near-infrared, at wavelengths of roughly one micron. The thinner outer envelope still absorbs a significant fraction of this light, re-emitting it at longer wavelengths. Therefore, the SED of a class I source still peaks in the far-infrared, but has a significant contribution in the near-infrared. In 10^6 years, the material in the envelope is accumulated in a protoplanetary disk and the central star becomes visible (Class II, Fig. 1.1). In this class, the star accretes from the disk and heating from the star will be the main source of energy in the disk. The SED therefore peaks in the optical, where the star shines, but a dominant near infrared excess from the disk remains and decreases roughly as a power law from the mid infrared to millimeter wavelengths. In the last step, the disk becomes mostly dissipated and shows only a partial emission from dust and almost no gas ("debris-disc", Class III , Fig. 1.1). In this class, the star and its planetary system remain. Planets are too faint to be detected in the SED, but smaller bodies may collide and generate a dusty debris disk that emits at IR.

The main work of the present thesis is to investigate the evolution and properties of dust and gas in Class II objects surrounding intermediate mass stars (1.5 $M_{\odot}$ - 4 $M_{\odot}$), i.e., Herbig AeBe stars, which are one class of Young Stellar Objects (Strom, 1972, YSOs).

There are different categories of objects that correspond to different types of YSOs:

1) **Protostars** are embryos of stars, which are receiving material from their infalling molecular cloud core.

2) **T Tauri** stars have spectral types ranging from F-M and stellar masses of 0.08-2 $M_{\odot}$. T Tauri stars can be classified based on their accretion properties. In weak T Tauri stars, material is no longer being accreted onto the star while classical T Tauri stars are still actively accreting material. The equivalent width of Hα is commonly used to identify the presence of accretion/ejection.

3) **Herbig Ae/Be** stars have spectral types A-B and masses of 2-10 $M_{\odot}$. Frequently observed emission lines in these stars are from hydrogen, oxygen, silicon, calcium, sulphur and magnesium. The lines show time variability and complex profiles. The photospheric

absorption features are fairly straightforward and the line strengths are consistent with F, A and B main sequence stars. In this thesis, I study two of these sources.

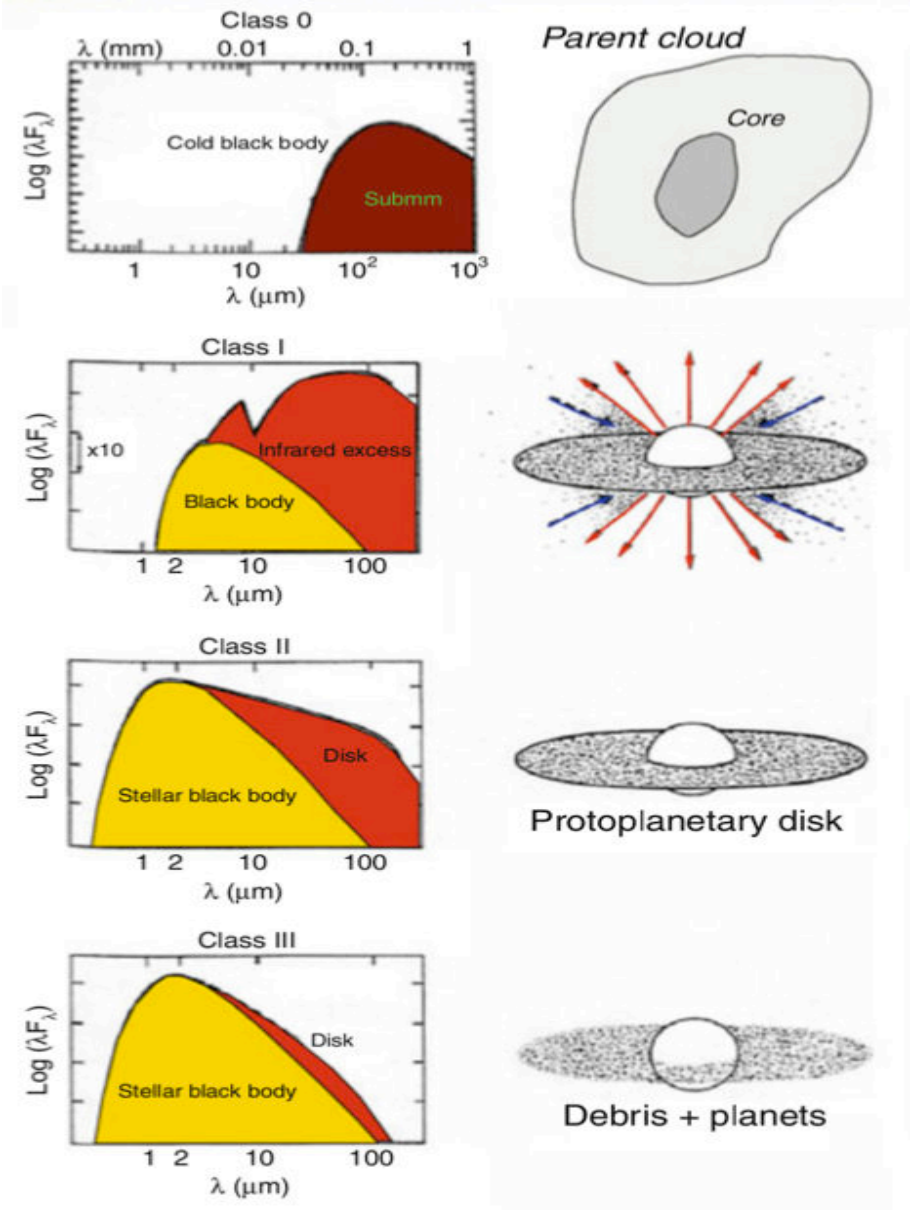

FIGURE 1.1: Different phases of star and protoplanetary disks with typical SEDs. The peak of IR emission shifts to short wavelengths as star and its disk start forming. This figure is taken from the thesis of Mulders 2013.

1.2 Protoplanetary disk phase

Planets usually form during the protoplanetary disk formation in a star formation region, for instance, Orion (See Fig. 1.2), and these disks are the main subject of this thesis.

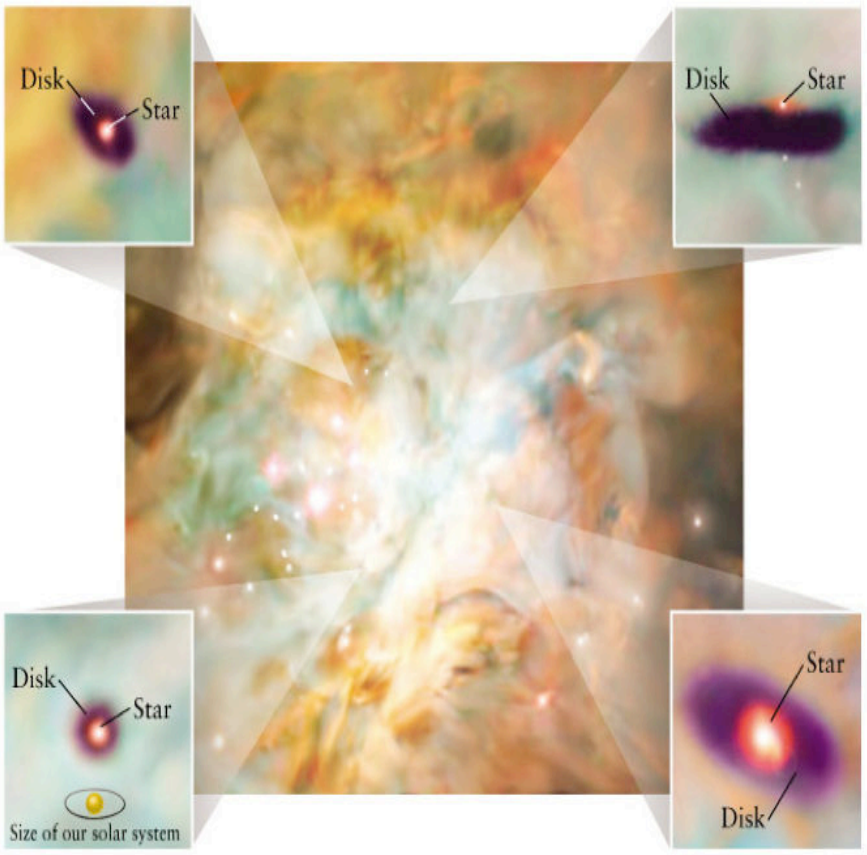

FIGURE 1.2: The disks around new stars in Orion nebula. Credit: C. R. O'Dell and S. K. Wong (Rice U.), WFPC2, HST, NASA.

At the beginning phase of the disk evolution, circumstellar disks are characterized by gas- rich disks with sub-micron dust grains and the gas mass to the dust mass ratio is $\sim$ 100:1 (Birnstiel et al., 2010), similar to the characteristics of the interstellar medium. With an abundance of gas close to the star, the accretion rate for protoplanetary disks of Herbig Ae stars is initially high with typical rates of more than $\sim 10^{-8} M_{\odot} yr^{-1}$ (Pogodin et al., 2012). Since the disk extends from a sub-AU to the star to greater than several hundred AU or more, the SED is characterized by strong levels of NIR to FIR excess (Zuckerman, 2001). The disk material near the star ($< \sim$ 1 AU) is characterized by temperatures higher than about 500 –1000 K and the emission tends to peak in the NIR. The warm dust further away from the star ($\sim$ 20 AU) emit with a peak in the MIR. Disks in this phase of evolution are generally called protoplanetary disks. Since small grains are mixed with the gas, and the disk is in hydrostatic equilibrium state, dusts material can be kept at significant distances from the disk mid-plane. Fig. 1.3, shows the SED versus wavelength for a Herbig star, whose emission in different regions of the disk is plotted with different colors. This Figure has been plotted to give the reader an idea about how the emission in different region of the disk varies with wavelength. The

stellar contribution is well approximated by a black body with a temperature equal to that of the stellar photosphere and dominates at shorter wavelengths (yellow color, Fig. 1.3). The inner disk contributes excess NIR emission (red color, Fig. 1.3). The outer disk contributes excess MIR and FIR emission and peaks in the 10–50 μm region (blue color, Fig. 1.3. The peak of MIR emission is not at 10 μm because the SED has been plotted for an Herbig star with a pre-transitional disk. The concept of pre-transitional disks will be explained at Sect. 1.7.1). The disk midplane is the coldest region and contributes excess emission at the sub-mm and millimeter wavelengths (violet color, Fig. 1.3).

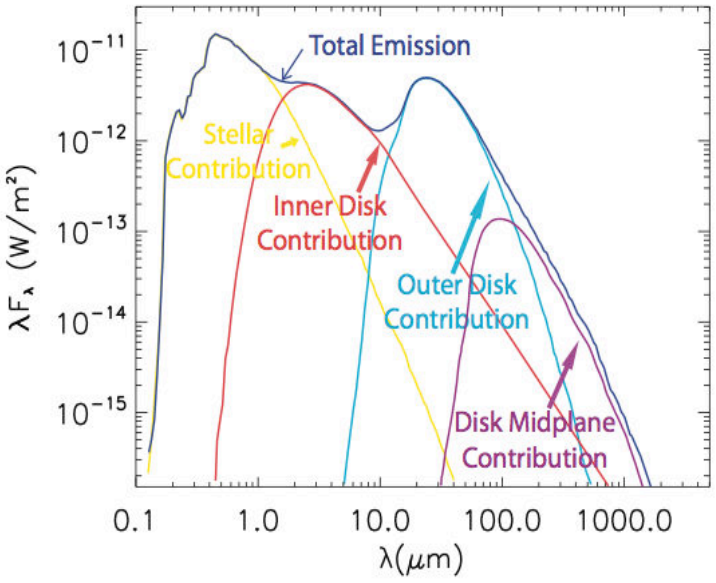

FIGURE 1.3: An example of the SED for a Herbig Ae star plus circumstellar disk. This figure is provided by M. Sitko, private communication.

1.3 Planet formation

Planets are not massive enough to form directly by a gravitational collapse like stars except in gravitational instability scenario. The gravitational instability happens when during bringing together the materials to form a structure, there are small irregularities in the distribution of matter. In this case, those regions with more matter will have a greater gravitational force on their neighboring regions and causes gravitational instabilities The most massive planets that are placed far from their central stars (Marois et al., 2008; Carson et al., 2013) may be an exception. However, most of the exoplanets discovered have much lower masses and are found closer to their central stars. These planets can form from the growth of microscopic dust grains to reach the size of terrestrial planets (Weidenschilling, 1980). A giant plant can be formed through the core-accretion

scenario (Pollack et al., 1996) if the rocky cores become massive enough to grow more by pulling in gas from the surrounding disk. This process has been presented in Fig. 1.4. This growth range is usually subdivided into a number of steps, in which different physics dominate the growth of dust (e.g. Chiang and Youdin, 2010; Morbidelli and Nesvorny, 2012).

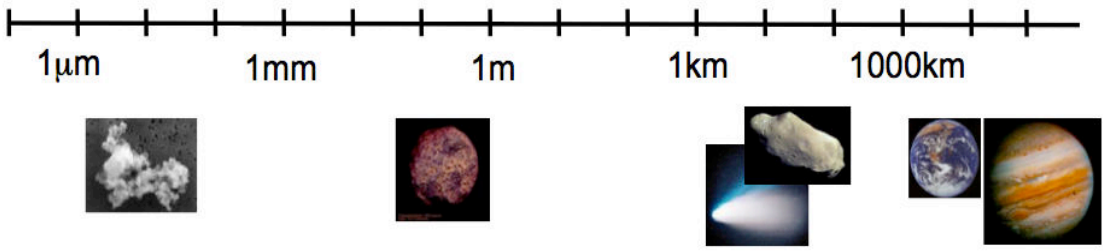

FIGURE 1.4: Approximate size range spanned in the planet formation process. Indicated below are objects found in the solar system, from left to right: an interplanetary dust particle, an asteroids and a comet, a terrestrial planet (Earth) and a gas giant planet (Jupiter). Figure based on C.P Dullemond's lectures.

1. Sticking and coagulation: in this step, the typical size of ISM (~ 0.1 μm) dust particles in the disk stick together and grow up to mm and cm sizes by collisional processes.

2. Radial-drift barrier: Growth of grains is difficult where grains are large to grow by coagulation and small to grow by gravitational interaction. This barrier is called radial-drift barrier (Laibe et al. 2012). One solution to overcome this barrier could be the collective gravitational effect of a collection of particles. For instance, long lived-structures in the gas such as vortices can trap a large number of particles and make them to collapse to much larger bodies (Johansen et al. 2006).

3. Gravitational forces: as soon as the particles reach the km-size (planetesimals), the gravitational forces cause them to grow up to Earth-size planetary rocky cores.

4. Gas accretion: in this step, the planetary rocky cores pull the surrounding gas and modify the distribution of gas in the planet vicinity. Gravitational interaction between the plant and the non-uniform gas produce torques that change the planet's orbit. This causes migration of a planet toward or away from the star. the direction of migration depends on the mass of the planet and the local condition of the gas disk.

1.4 The radial structure of the disk

Similar to the planets in our solar system, in protoplanetary disks the gas and dust rotate around their host star. The rotational velocity of the dust and the gas is given by the

radial component of the equation of motion. The equation of motion, for non-magnetised fluid is

$$\frac{\partial \overrightarrow{v}}{\partial t} + (\overrightarrow{v}.\nabla)\overrightarrow{v} = -\frac{1}{\rho}\nabla P - \nabla\Phi \tag{1.1}$$

where $\overrightarrow{v}$ is the fluid velocity, ρ the density, P the pressure and Φ the gravitational potential. Considering a disk as a stationary symmetric flow around a central star as a central gravitating mass and working in cylindrical coordinates, the radial component of Eq. 1.1 is an expression of centrifugal balance

$$\frac{v_\phi^2}{r} = \frac{1}{\rho}\frac{\partial p}{\partial r} + \frac{GM_\star}{r^2} \tag{1.2}$$

For duts, p=0, we find that the azimuthal velocity v_ϕ is simply the Keplerian velocity $v_k = \sqrt{GM_\star/r}$. This is the velocity of the dust in the protoplanetary disk. For the gas, its pressure in the disk decreases outwards (as surface density and temperature are decreasing with distance from the central star). Therefore the term dP/dr in Eq. 1.2 is negative, so that the velocity of the gas is sub-Keplerian.

This simple fact gives rise to significant differential motion between the dust and gas since the dusts in keplerian rotation feel a head-on wind which slows them down. This drag force makes a radial drift toward the central star on timescales as short as hundreds of years for meter-size grains (Weidenschilling 1997). This timescale is even shorter compared to the time scale of planet formation, i.e., few million years. However, Weidenschilling (1997) only applies to the Minimum Mass Solar Nebula (MMSN), in which the critical size corresponds to metre-sized bodies and thus was called the radial-drift barrier. Observed dusty disks are drastically different from the MMSN prototype (Laibe et al. 2012, Laibe 2014). Several scenarios have been proposed to solve this problem. One possibility is the presence of vortices in the protoplanetary disk. In this scenario the vortices can concentrate solids in their centre and accelerate the growth process (Barge & Sommeria (1995)).

Most of the disks accrete gas onto the central star, at a rate of roughly 10^{-8} $M_\odot$/yr (Solar masses per year) for classical T Tauri stars (Hartmann et al., 1998). This means that during the disk lifetime, they accrete about one hundredth of a solar mass of gas, a significant amount of the total disk mass by difinition. Since most of the mass of the disk is in the outer disk, an efficient mass transport mechanism throughout the entire disk is required.

Assuming that the gas is in Keplerian orbits, material close to the star rotates faster than gas or dust further out. The friction between the gas causes the gas to be spread at different radius. The inner gas slows down while the outer gas speeds up. In order to conserve angular momentum, the inner gas that was slowed down rotates in a closer orbit, while the outer gas that was sped up will move to a farther orbit. The effect of this transfer is that the gas will spread radially immediately in both directions, a phenomenon called viscous spreading.

When the disks are geometrically thin, the equations describing the radial structure can be decoupled from those describing the vertical structure. For a symmetric disk, the evolution can be described in terms of the surface density Σ, which is the amount of material in a column perpendicular to the disk per unit surface, at a certain distances from the star, r and indicate how the mass of the dust is distributes along the disk. The time-dependent evolution of the gas was first derived by Lynden-Bell and Pringle (1974), who showed that a part of gas in a viscous disk accretes onto the star, while a part at larger radii carries away the angular momentum. The evolution of the surface density under the influence of a viscosity ν at a time t is given by Pringle (1981):

$$\frac{\partial}{\partial t}\,\Sigma(r,t) = \frac{3}{r}\,\frac{\partial}{\partial r}\left(r^{1/2}\frac{\partial}{\partial r}\left[\nu\,\Sigma(r,t)\,r^{1/2}\right]\right) \tag{1.3}$$

If we know the boundary conditions of the surface density, we can determine the disk evolution only by viscosity. From a theoretical point of view, the molecular viscosity of the gas was not sufficient to explain the observed accretion rates and disk lifetimes, therefore, another mechanism was needed. One of the mechanism proposed was the ideas of Shakura and Sunyaev (1973).

In this case, the viscosity ν has units $[m^2/\mathrm{s}]$, i.e. a length scale [m] times a velocity [m/ s]. Taking the pressure scale height of the disk h_p as the maximum size of vertical turbulence and the sound speed c_s as their maximum velocity, the viscosity is given in the form of Pringle (1981) by:

$$\nu = \alpha\, h_p\, c_s, \tag{1.4}$$

where $\alpha < 1$ is a dimensionless parameter that describes the whole strength of the viscosity. Ruden and Pollack (1991) showed that the total viscosity rapidly diminishes as the midplane optical depth decreases below a critical value, $\tau_{critical}$. They considered that if the optical depth is equal or less than this critical value, which was calculated and obtained roughly 1.78, the viscosity vanishes.

Looking at the steady state solution for an infinite disk, we can obtain a good estimate of the surface density profile ignoring boundary conditions. If we assume that the scale height and sound speed are described by power-laws, Eq. 1.3 can be solved in analytical way. A steady-state disk ($\frac{\partial}{\partial t}\,\Sigma(r,t)$=0, for a flaring disk that is matched with observations with exponent of temperature law of q=0.5 with a sound speed of c_s $\propto r^{-0.25}$, flaring surface of $h_p \propto r^{1.25}$, Sect. 1.5) results in $\Sigma(r,t) \propto r^{-1}$. Compared to the surface density law in MMSN (Weidenschilling, 1997; Hayashi, 1981), i.e., $\Sigma(r,t)$ $\propto r^{-1.5}$, the surface density in α-type viscosity decreases less steepy than MMSN. The basic idea behind the MMSN is to use the structure of the solar system as we observe it now to derive the structure of the disk from which the planets formed.

These α disk models are reasonably successful in explaining disk observations. Looking at accretion rates, and comparing disk lifetimes to sizes and radii, yields a typical value of $\alpha = 0.01$ (Hartmann et al., 1998).

1.5 The vertical structure of the disk

Protoplanetary disks are mostly heated by the central star, thus their vertical structure specifies the amount of radiation that the disks can absorb and re-emit. In the flat-disk models, the effective temperature of the disk is set by the thermal balance between the heating due to the influence of the stellar radiation and the black-body cooling, which results in $q = 3/4 = 0.75$ for the temperature profile $T_{eff} \propto r^{-q}$ **(Pringle, 1981).** This kind of temperature profile makes a steep slope in the SED and a stronger emission at short wavelengths. However, from observations of classical T Tauri stars, values of q are found lower in the range 0.5-0.65 (Beckwith et al., 1990). This causes a higher emission at long wavelengths beyond the IR part of the SED (Fig. 1.5). In a flared disk, the amount of far-infrared emission increases because of re-emission of a significant fraction of the starlight is re-emitted by the dust particles at longer wavelengths.

The degree of flaring of the disk surface and the observational appearance of the disk depends on the vertical structure of both gas and dust.

Assuming that there is no vertical motion in the disk, the hydrostatic equation states that the difference in pressure (dp) between two levels (dz) is caused by the weight of the layer of the fluid (mass $\times$ acceleration due to gravity=$\rho\ dz \times g$), considering a unit cross-sectional area (Fig. 1.6). Note that g depends on z (Eq. 1.5).

Let us consider the gas in the disk at a radius r from the star and at a height z above the mid plane of the disk of density $\rho(r,z)$. Assuming the gas is on a Keplerian orbit at

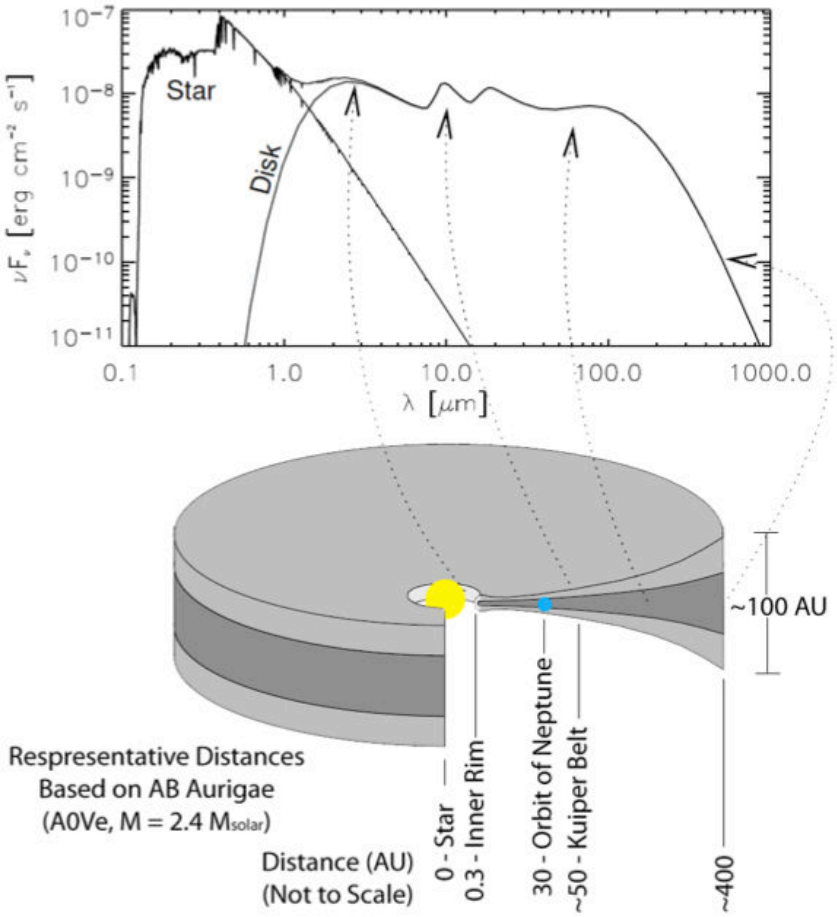

FIGURE 1.5: SED model and distance scale for a young protoplanetary flared disk. This figure is taken from Karen Alicia Collins's thesis, private communication.

a given radial distance r, in vertical direction, the gas only feels the vertical component of the gravitational field of the star, given by:

$$g_z(r,z) = \frac{GM_\star}{r^2}\frac{z}{r} = {\Omega_k}^2(r)\; z\,, \tag{1.5}$$

where $g_z(r,z)$ is the gravitational acceleration in the z-direction, G is the gravitational constant, $M_\star$ is the mass of the star and $\Omega_k(r)=\sqrt{\frac{GM_\star}{r^3}}$ is the Keplerian frequency for a body at the distance r from the star. To achieve equilibrium between the gravitational force acting on a gas volume and the pressure gradient force in vertical direction, this acceleration must be balanced by the pressure from the gas below it, minus the pressure from the gas above it, i.e. the pressure gradient,

$$\frac{dp(r,z)}{dz} = -g_z(r,z)\;\rho(r,z)\,, \tag{1.6}$$

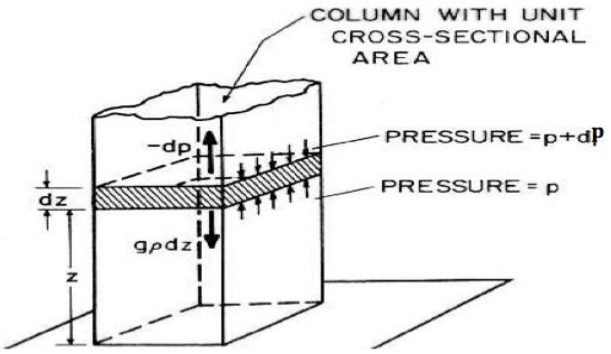

FIGURE 1.6: The column with unit cross-sectional area. Credit: PHYS/EATS 3280.

where $p(r, z)$ is the gas pressure.

Combined with the equation of state that relates the pressure to the density for an ideal gas $p(r, z)$=$\rho(r, z)$ $c_s(r)^2$, and reordering variables, we find,

$$\frac{d\rho(r, z)}{\rho(r, z)} = -\frac{\Omega_k^2(r)\ z\ dz}{c_s^2(r)}\,, \tag{1.7}$$

where $c_s(r)$ is the speed of the sound assumed independent of z, i.e. there is no vertical temperature gradient.

$$c_s(r) = \sqrt{\frac{k\ T(r)}{\mu\ m_H}}\,, \tag{1.8}$$

where μm_H is the average mass of the gas, where μ is the mean molecular weight and m_H is the mass of one hydrogen atom. k is the Boltzmann constant. Assuming isothermal condition in the vertical direction of the disk for each radius, the temperature T(r) in Eq. (1.8) follows a power-law in radial distance from the central star (See Eq. (5.1) of Chapter. 5. Considering a flared disk with exponent of temperature law of q=0.5, c_s will be proportioanl to $r^{-0.25}$). Eq. (1.7) can be directly integrated to find the vertical pressure and corresponding density structure of the gas (Pringle, 1981):

$$\rho(r, z) = \rho_0(r) exp\left(-\frac{z^2}{2\ h_p^2(r)}\right)\,, \tag{1.9}$$

where $h_p(r) = c_s(r)/\Omega_k(r)$ is the pressure scale height. Considering Eq. (1.8) and $\Omega_k(r)$=$\sqrt{\frac{G\ M_\star}{r^3}}$, one can write $h_p(r)$:

$$h_p(r) = \sqrt{\frac{k\,T(r)\,r^3}{G\,M_\star\,\mu\,m_H}}\,, \tag{1.10}$$

We can rewrite $h_p(r)$ as:

$$h_p(r) = \left(\frac{T(r)}{T_c}\right)^{\frac{1}{2}} \left(\frac{r^{\frac{3}{2}}}{R_\star{}^{\frac{1}{2}}}\right)\,, \tag{1.11}$$

where T_c is the critical temperature which is a measure of the gravitational potential at the surface of the star, T_c=$G\,M_\star\,\mu\,m_H/kR_\star$ (Chiang and Goldreich, 1997).

Combining Eq. (1.11) and $T(r)$ from Eq. (5.1) of Chapter 5, gives the pressure scale height :

$$h_p(r) = \left(\frac{T_{in}\,r_{in}{}^q}{T_c}\right)^{\frac{1}{2}} \left(\frac{r^{\frac{3}{2}-\frac{q}{2}}}{R_\star{}^{\frac{1}{2}}}\right) \tag{1.12}$$

Considering a flared disk with temperature law exponent of q=0.5, h_p will be proportional to $r^{1.25}$.

It is convenient also to consider the atmosphere height h_τ(r), defined at the height where the optical depth in the vertical direction is equal to 1. The optical depth is integrated from infinity along the z direction toward the disk mid plane,

$$\tau_\lambda(r) = \int_{+\infty}^{h_\tau(r)} d\tau_\lambda = 1\,, \tag{1.13}$$

$$\tau_\lambda(r) = \int_{+\infty}^{h_\tau(r)} \kappa_\lambda\,\rho(r,z)\,dz = 1\,, \tag{1.14}$$

where κ_λ is the mass absorption coeffitient and is equal to $\pi\,a^2/m$ assuming that the absorption coefficient is 1 (See Sect. 1.6). $\pi\,a^2$ is the cross section of the dust grains with radius a. m is the mass of one grain, m=4/3 $\pi\,a^3\,\rho_{grain}$. ρ_{grain} is the mass density of the material composing the dust grain. Consequently, Eq. (1.14) could be written as,

$$\tau_\lambda(r) = \frac{3}{4} \int_{\infty}^{h_\tau(r)} \frac{1}{a\,\rho_{grain}} \rho(r,z)\,dz = 1 \tag{1.15}$$

Since there is no analytical solution to find h_τ(r) from Eq. (1.15), we solved the integration iteratively. ρ(r,z) in Eq. (1.15) comes from Eq. (1.9). It is linked to $\rho_0(r)$, the density in the mid-plane of the disk that is scaled to the surface density $\Sigma(r)$:

$$\rho_0(r) = \frac{\Sigma(r)}{\sqrt{2\pi}\, h_p(r)} \tag{1.16}$$

$\Sigma(r)$ in Eq. 1.16 is calculated from the integration on volume density in the vertical direction, z, for each radial distance from the central star as follows:

$$\Sigma(r) = \int_0^\infty \rho(r,z)\, dz \tag{1.17}$$

In Chapter 6, we quantify and plot $h_p(r)$ and h_τ versus the radial distance for the specific case of a Herbig star with the model characteristics of MWC480.

1.6 Dust properties

Dust is one of the most important ingredients of the interstellar medium. Its mass is only a small fraction: somewhere between 1% and 2%. But dust particles have radiative and chemical properties that make them outstanding. From a chemical point of view, they are important since they have surfaces and compared to gas phase chemical reactions can happen much more easily. From a radiative transfer perspective they are important since they have high continuum opacities. Also, dust extinction can protect specific regions of the interstellar medium from ultraviolet photons, therefore, molecules are able to form in those regions.

If we try to observe with infrared and millimeter-wave telescopes at arbitrary points in the sky, the emission we obtain is mostly dominated by thermal emission from dust. Molecular clouds seems to be black in IR wavelengths on the sky due to the dust extinction.

Mid-IR observations of the dust in protoplanetary disks, especially with the Infrared Space Observatory and later with the Spitzer Space Telescope, have provided strong constraints on the dust properties in protoplanetary disks (e.g. Watson, 2009). The presence of broad solid state features at 10 and 20 μm indicate the presence of (sub)micron-sized amorphous silicate grains in the upper layers of protoplanetary disks (see Fig. 1.5). They are mostly olivines ($[MgFe]_2SiO_4$) and pyroxenes ($[MgFe]SiO_3$), and tend to be magnesium-rich and iron-poor (Juhász et al., 2010).

1.6.1 Dust opacity

Dust determines the opacity in the protoplanetary disks. The disk geometry and the opacity both are key factors to determine the temperature structure of the disk, the SED and other observational quantities.

The dust opacity depends on the grain sizes, the chemical compositions, and the shapes (e.g. Miyake and Nakagawa, 1993; Pollack et al., 1994; Draine and Allaf-Akbari, 2006). In order to extract estimates from the near-IR to sub-mm/mm SED for the dust grain sizes and the dust mass in the disks, assumptions on the chemical composition and shape of the dust grains have to be made.

In this step, we focus on the typical astrophysical dust opacities. The most common solids in space are silicates, carbonaceous materials and ices such as water ice, CO ice, etc. These minerals can also be mixed, since small dust particles of a composition form small aggregates of grains of different compositions. But this is still not well understood.

Another important parameter to estimate the opacity of the dust is the shape of grains. Optical properties calculated using the Mie theory (Mie 1908), which assumes homogeneous, compact, spherical dust grains, often do not properly fit continuum observations. The spherical symmetry causes resonances at certain scattering angles and in the spectral energy distribution (SED), which are not observed in real disks (Min et al., 2007). It is also possible to use other particle shapes, such as a distribution of hollow spheres (Min et al., 2005). Their opacities mimic those of particles with an irregular shape, and provide a better fit to the observed spectral features. Dust is likely present in the form of aggregates, but computing their optical properties is computationally expensive.

In addition to the chemical composition and shape of grains, the grain size also is important to determine the dust opacity. As it is unlikely to have all grains with equal size within a circumstellar disk, a distribution of their dimension needs be considered. A common way to do it is assuming the grain size distribution

$$n(a) \propto a^{-\gamma} \qquad a_{min} \leq a \leq a_{max} \tag{1.18}$$

where the particle radius a is limited between a_{min} and a_{max} value. In the ISM, a_{min} is a few tens of Angstrom, $a_{max} = 0.1$–0.2 μm, and $\gamma = 3.5$ (Mathis et al. 1977, Draine & Lee 1984, by analyzing extinction and scattering of starlight from the interstellar dust).

With such an ensemble of different particles (see Eq. 1.18), Miyake and Nakagawa (1993) wrote the dust opacity as

$$\kappa_\lambda = \frac{\int n(a) a^3 \kappa_{\lambda,1}(a) da}{\int n(a) a^3 da} \tag{1.19}$$

where the integration is performed between the two limit values for a, and $\kappa_{\lambda,1}$ is the opacity of the single particle (and depends on grain shape and chemical composition), at a given wavelength λ.

If the radiation travels through a medium, a column density with length l and cross section S, the radiation then will be attenuated. The attenuation or extinction coefficient of this column density characterizes how easily it can be penetrated by a beam of light. A large extinction coefficient means that the beam is quickly "attenuated" (weakened) as it passes through the medium, and a small extinction coefficient means that the medium is relatively transparent to the beam.

When a parallel beam passes through the column density, the beam will lose intensity due to two processes: absorption and scattering. Absorption coefficient of this medium is given $Q_{abs}(\lambda)$, and scattering coefficient of this medium is given $Q_{sca}(\lambda)$.

The extinction coefficient, $Q_{ext}(\lambda)$, of the column density is the sum of the absorption coefficient and the scattering coefficient:

$$Q_{ext}(\lambda) = Q_{sca}(\lambda) + Q_{abs}(\lambda) \tag{1.20}$$

The absorption coefficient determines how far into a material light of a particular wavelength can penetrate before it is absorbed, while extinction coefficient measures the total loss of beam intensity, including scattering as well. The extinction coefficient is always larger than the absorption coefficient, although they are equal in the idealized case of no scattering.

If the particle is, for instance, a transparent sphere (e.g. a rain drop) with some index of refraction, then virtually no light is absorbed, but the light is, through refraction on the surface, redirected into another direction. In this case, the scattering coefficient is greater than the absorption one. If, on the other hand, the dust particle is made up of graphite, then only a small fraction of the incident light is scattered and most is absorbed. Therefore, the absorption coefficient is greater.

According to Fig. 1.7, the effective cross-section of the grain ($\sigma_a(\lambda)[m^2]$) can be smaller or larger than the geometrical size of the grain (A $[m^2]$), related by its extinction coefficient [$dimensionless$]. For extinction, we name the $\sigma_a(\lambda)$ as $\sigma_{ext}(\lambda)$:

$$\sigma_{ext}(\lambda) = Q_{ext}(\lambda)\ A \tag{1.21}$$

For absorption and scattering, σ_a is σ_{abs} and σ_{sca} respectively. So one can write,

$$\sigma_{abs}(\lambda) = Q_{abs}(\lambda)\ A, \quad \sigma_{sca}(\lambda) = Q_{sca}(\lambda)\ A, \quad \sigma_{ext}(\lambda) = (Q_{abs}(\lambda) + Q_{sca}(\lambda))\ A \tag{1.22}$$

The amount and character of the scattering is expressed by

$$Albedo(\lambda) = \frac{\sigma_{sca}(\lambda)}{\sigma_{ext}(\lambda)} \leq 1 \tag{1.23}$$

Albedo is the reflecting power of a surface and it is changed from zero for a surface without reflection to 1 for surface with a perfect reflection.

In the following, I remind some of the practical relations modeling the interactions between the light specific intensity I_λ, and the dust properties.

Considering the column density with length l and cross section S, if the optical effective cross-section of each grain is $\sigma_{ext}(\lambda)$ (units m^2), then assuming the beam travels through the length dl, the total area of gains, which are encountered in the column density would be $n_{grains}\ dS\ dl\ \times\ \sigma_{ext}(\lambda)$. n_{grains} (units m^{-3})is the number of grains in the length of dl

In fact the fraction of attenuated radiation is proportional to the fraction of the area blocked by the grain:

$$\frac{dI_\lambda}{I_\lambda} = \frac{n_{grains}\ dS\ dl\ \sigma_{ext}(\lambda)}{dS} = n_{grains}\ \sigma_{ext}(\lambda)\ dl \tag{1.24}$$

τ_λ defines the optical depth of a column density with length l and cross section S and for considered wavelength, λ. Consequently, one can write Eq. 1.24 in terms of optical depth:

$$d\tau_\lambda = \frac{dI_\lambda}{I_\lambda} = \frac{n_{grains}\ dS\ dl\ \sigma_{ext}(\lambda)}{dS} = n_{grains}\ \sigma_{ext}(\lambda)\ dl \tag{1.25}$$

The optical depth describes how much absorption or scattering or extinction occurs when light travels through a medium (for example, a planetary atmosphere or an interstellar dust cloud composed of gas and dust particles).

Integrating Eq. 1.25 gives:

$$I_\lambda = I_{\lambda,0}\, e^{-\tau_\lambda}, \tag{1.26}$$

where $I_{\lambda,0}$ is the initial specific intensity and I_λ is the attenuated light passed through a column density with optical depth of τ_λ.

Combining Eq. 1.21 and Eq. 1.25 we have,

$$d\tau_\lambda = Q_{ext}(\lambda)\, A\, n_{grains}\, dl, \tag{1.27}$$

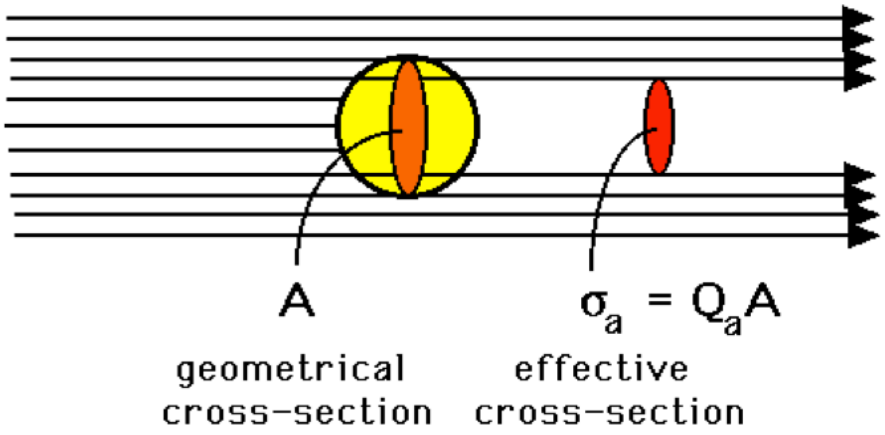

FIGURE 1.7: A schematic view of the absorption of the light by a grain. Credit from ECE532 Biomedical Optics.

We can then rewrite Eq. (1.27) adding the mass of one grain, m,

$$d\tau_\lambda = (Q_{ext}(\lambda)\, A/m)\, m \times n_{grains}\, dl \tag{1.28}$$

In Eq. 1.28, $m \times n_{grains}$ is the density of the dust fluid, ρ_d. Assuming the column density is in vertical direction of a disk,

$$d\tau_\lambda = (Q_{ext}(\lambda)\, A/m)\, \rho_d\, dz \tag{1.29}$$

In this case, integrating Eq. 1.29 gives the vertical optical depth of the disk,

$$\tau_\lambda(r) = \kappa_\lambda^{ext}\, \Sigma_{dust}(r), \tag{1.30}$$

where $\tau_\lambda(r)$ is the vertical optical depth for each radius, $\Sigma_{dust}(r)$ is the surface density of the dust phase (see Eq. 1.17) and $(Q_{ext}(\lambda)\, A/m)$ is the mass extinction coefficient, κ_λ^{ext} or extinction opacity.

The extinction opacity is the sum of absorption opacity and scattering opacity,

$$\kappa_\lambda^{ext} = \kappa_\lambda^{abs} + \kappa_\lambda^{sca}, \tag{1.31}$$

To evaluate the grain growth from observations of continuum emission from circumstellar disks, opacity is useful to be considered. While the surface density $\Sigma_{dust}(r)$ is not assumed to be dependent on the local conditions of the dust in the disks, κ_λ^{ext} or κ_λ^{abs} or κ_λ^{sca} include different factors: grains shape, size and chemical composition. Although these factors have been deeply studied, which dust ensemble should be the most appropriate for protoplanetary disks is still today a great matter of study and depends on the local conditions in the disk. In this thesis, in Chapters 4, 5 and 6, I will use the dust opacity in my model.

Since in Chapter 4 the Mie theory is used in the radiative transfer code, MCFOST, in the following, I give a short introduction of this theory reminding some basics on scattering.

1.6.2 Dust scattering

In this section, the main objective is to calculate the scattering and absorption cross sections at a given wavelength, for a particle of a given size and shape, made from a given type of material.

Suppose an electromagnetic field interacts with a dust grain. If refraction happens, the properties of the material are fully given by the complex index of refraction

$$m(\lambda) = n(\lambda) + ik(\lambda), \tag{1.32}$$

where $n(\lambda)$ and $k(\lambda)$ are the real and the imaginary part of the complex index of refraction. One can interpret n and k as the scattering and absorption part of the refractive index.

Another fundamental parameter is the ratio of the size of the particle over the wavelength:

$$x = \frac{2\pi a}{\lambda} \tag{1.33}$$

where a is the radius of the particle. This parameter is only well-defined for spherical particles. Nevertheless, it gives a rough idea of how the particle size and the wavelength compare. We can distinguish three regimes:

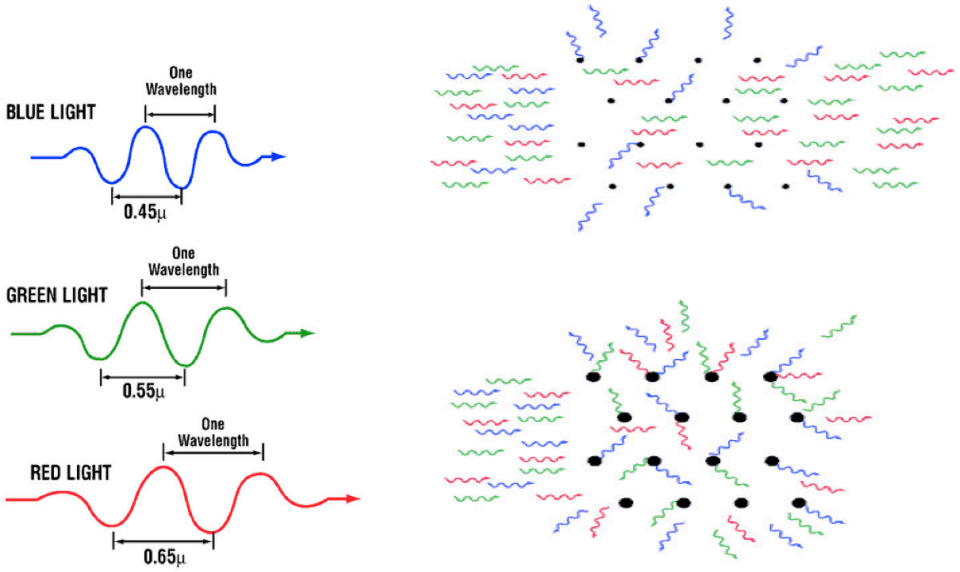

FIGURE 1.8: Left: three different incident light with different wavelength,i.e., blue: 0.45 μm; green: 0.55 μ and red: 0.65 μ. Right-top: Scattering process for three different incident wavelength (left part of figure) and for small grains much smaller than the wavelength of incident light following Rayleigh scattering. Right-bottom: Scattering process for three different incident wavelength (left part of figure) and for larger grain sizes comparable to the wavelength of incident light following Mie theory (Mie 1908). Credit: Visibility and Light Scattering in the Atmosphere.

- $x \ll 1$ (the Rayleigh regime): the particle is much smaller than the wavelength. In this regime the scattering process is called Rayleigh scattering. In this case, the light is scattered from small grains in short wavelengths, which the size of grain is comparable to the size of wavelength of the incident light (see Fig. 1.8-right-top).

- $x \simeq 1$: the particle size is similar to the wavelength. This is the most complex regime, and requires the full solution of the Maxwell equations. In this case, the grains are larger than Rayleigh phase (see Fig. 1.8-right-bottom).

- $x \gg 1$ (geometric optics regime): the particle is much larger than the wavelength. This does not mean that its scattering is simple. The reflection on the surface and refraction in the interior can still be quite complex, but it can be calculated using for instance ray-tracing through the particle and the particle's surface.

Calculating the scattering and absorption cross sections for all wavelength regimes is complicated since it has to taken into account the radiative transfer in whole disk and for all different dust shapes and compositions. For homogeneous dust spheres this was first done in its full complexity by Gustav Mie (Mie 1908). This calculational method is called Mie theory.

1.6.3 Mie Theory

Understanding Mie theory is not an easy task. Here, I shortly discuss the basic idea behind it since I use this theory in MCFOST code in Chapter 4.

We assume a plane electromagnetic wave with a wavelength λ hits a sphere of radius a with a complex refractive index m (See Eq. 1.32). The wave and the sphere interact with each other and it causes the sphere to radiate electromagnetic waves of itself. These waves are not isotropic in general. Isotropic scattering means that the wave will be scattered the same way in all directions. We can expand the outgoing wave using the vector spherical harmonics. The idea is the same as for expanding a scalar field in spherical harmonics, but for a vector field. Like with spherical harmonics, this involves Legendre polynomials and Bessel functions. The expansion coefficients are written as a_n and b_n, where n is the expansion index going from n=1 to n$\rightarrow \infty$. These a_n and b_n are called the scattering coefficients.

Now, we expand the incoming plane wave into the same set of vector spherical harmonics. The expansion coefficients are written as c_n and d_n. The aim is to link a_n and b_n (the outgoing wave) to c_n and d_n (the incoming wave). This can be done by applying the usual boundary conditions for the electric and magnetic fields at the edge of the sphere and for each value of n separately. The results is:

$$a_n = \frac{m\ \Psi_n(mx)\ \Psi'_n(x) - \Psi_n(x)\ \Psi'_n(mx)}{m\ \Psi_n(mx)\ \xi'_n(x) - \xi_n(x)\ \Psi'_n(mx)} \tag{1.34}$$

$$b_n = \frac{\Psi_n(mx)\ \Psi'_n(x) - m\ \Psi_n(x)\ \Psi'_n(mx)}{\Psi_n(mx)\ \xi'_n(x) - m\ \xi_n(x)\ \Psi'_n(mx)} \tag{1.35}$$

Where Ψ and ξ are the Riccati-Bessel functions[1]

Since we know the full expansion of the outgoing wave, we can calculate the scattering cross section:

$$\sigma_{sca} = \frac{2\pi}{k^2} \sum_{n=1}^{\infty} (2n+1) \left(|a_n|^2 + |b_n|^2 \right) \tag{1.36}$$

where k $= 2\pi/\lambda$ is the wave number of the incident wave. The full extinction coefficient (scattering + absorption) is:

[1]The Riccati-Bessel function Ψ_n is also often written as $\S_n$, and is given by $\Psi_n(x) = x j_n(x)$ in terms of the spherical Bessel function $j_n(x)$.

$$\sigma_{ext} = \frac{2\pi}{k^2} \sum_{n=1}^{\infty} (2n+1) Re(a_n + b_n) \tag{1.37}$$

From this one can calculate the absorption cross section as

$$\sigma_{abs} = \sigma_{ext} - \sigma_{sca} \tag{1.38}$$

1.7 Protoplanetary disk Models

The SED of a disk can be computed in first approximation assuming that each disk annulus emits as a black body at the effective temperature T_d, so that the observed flux at any given wavelength λ is given by the relation (Malbet et al. 2005):

$$F_\lambda = \frac{cos\ i}{D^2} \int_{R_{in}}^{R_{out}} B_\lambda(T_d)(1 - e^{-\tau_\lambda}) 2\pi\ r\ dr \tag{1.39}$$

where R_{in} and R_{out} are the inner and outer disk radii, D is the distance from the observer, i is the disk inclination with respect to the line of sight (i=0 means face-on disks), B_λ is the black body emission. The optical depth τ_λ is,

$$\tau_\lambda = \frac{1}{cos\ i} \kappa_\lambda\ \Sigma_{dust}(r) \tag{1.40}$$

Where κ_λ is the total (gas+dust) opacity at the wavelength λ and $\Sigma_{dust}(r)$ is the surface density of the dust (see in details Sect. 1.6).

Chiang & Goldreich (1997, CG97) computed a radiative transfer model based on a flared circumstellar disk, which explains the flaring geometry by means of vertical hydrostatic equilibrium and provided a temperature profile with index $q = 0.5$ and a SED at IR and longer wavelengths. CG97 have been quite successful in the interpretation of observed SEDs of disks around YSOs, and is still nowadays widely assumed as the starting base for studies of those objects.

Afterwards, many improvements have been suggested. For instance, Dullemond et al. (2001, henceforth DDN01) proposed a model based on CG97 with some further implementations. The model DDN01 was basically based on CG97, plus the addition of an inner 'puffed-up' rim. The idea of a puffed-up inner rim was proposed by Natta et al. (2001) and developed further by DDN01 for Herbig Ae stars, to account for the shape

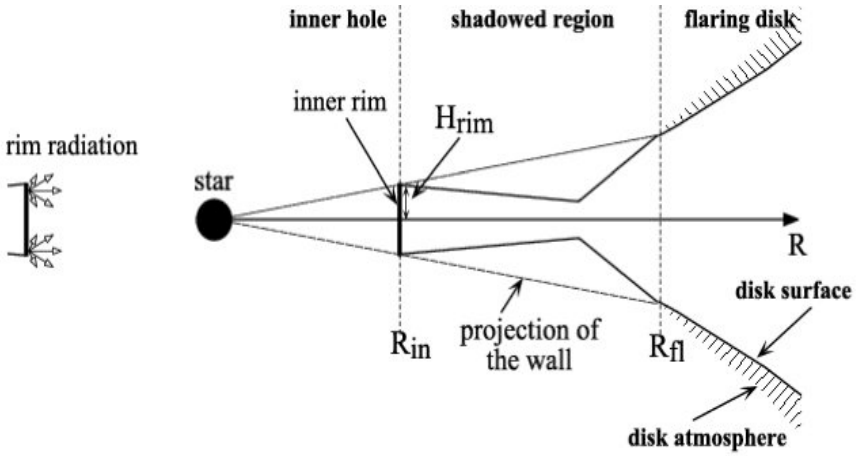

FIGURE 1.9: The Dullemond (Dullemond et al. [2001]) passive and flared disk model.

of the near-infrared excess of these stars (3-μm bump"). In the DDN01 model, the vertical structure of the circumstellar disk was set by a balance between disk gravity and the pressure gradient created from the heating of disk material by stellar photons (see. Fig. 1.9). One success of this model has been the correct prediction of the NIR size- luminosity diagram for YSOs (Monnier & Millan-Gabet 2002, Millan-Gabet et al. 2007).

According to Fig. 1.9, the inner rim in the DDN01 model casts a geometric shadow on the region behind it, preventing it from receiving direct star light. The disk in the shadow is heated by scattered photons from the rim edge and through radial heat diffusion. The size of the shadow can be several AU depending on the rim geometry, the mass of dust in the outer disk and dust grain properties in the outer disk. The shadow corresponds to the terrestrial planet forming region in circumstellar disks inside/close to the snow line.

When the outer disk is dominated by gas mass, the disk eventually emerges from the shadow and 'flares'. The flared disk can be a few hundred AU in size and emits radiation in the MIR and longer wavelengths (Fig. 1.9).

Although DDN01 succeed to explain a variety of observations, the structure of the inner rim was not explained. DDN01 assumed that the inner rim is 'vertical', and that its photospheric height is controlled by radial heat diffusion behind the rim. This model is not consistent with the near-IR emission of Herbig stars where their disks for instance are face-on, for which the projection on the line of sight of the rim surface is null. (see. Fig. 1.10).

Later, Isella & Natta (2005) investigated the shape of the illuminated face of the rim. They found that the shape of the inner rim is dependent on their very large vertical

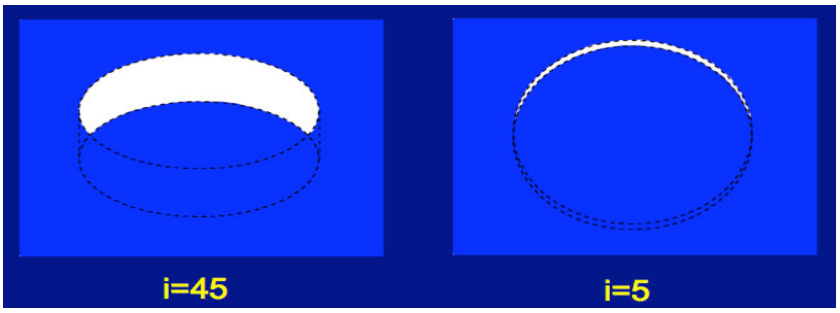

FIGURE 1.10: The effect of inclination on a vertical rim. Credit from talk of C.P. Dullemond.

density gradient. They concluded that the bright side of the rim is naturally curved, rather than vertical, as expected when a constant evaporation temperature is assumed.

They showed that for a given star, the rim properties depend mostly on the properties of the grains. Fig. 1.11 represents the shape of the inner rim as a plot of the photospherical height H (when the optical depth to the stellar radiation is 1) versus the distance from the central star for different values of ϵ. The quantity ϵ is the ratio of the mean Planck opacity at the evaporation temperature to that at the stellar temperature. This plot shows that the distance of the inner rim from the central star is dependent on the evaporation temperature of the dust particles that have the highest evaporation temperature where their opacity is enough for a very optically thick disk. In the model of Pollack et al. (1994) of the dust in accretion disks, silicates have the highest evaporation temperature. Fig. 1.11 has been plotted for astronomical silicates (Isella & Natta (2005)).

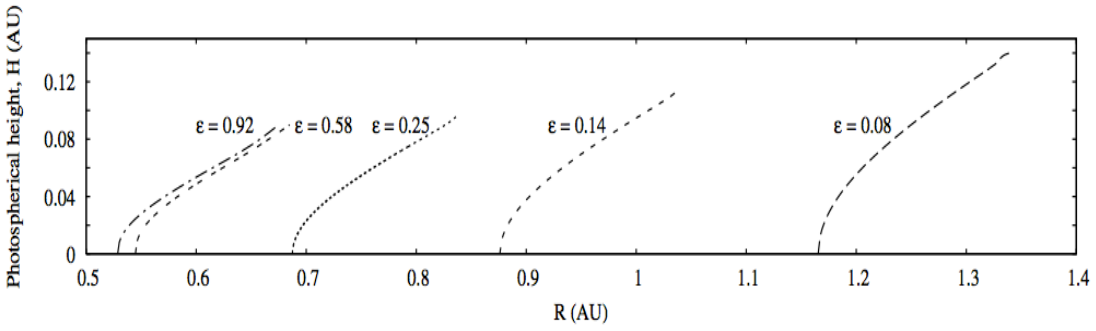

FIGURE 1.11: Photospherical height H (when the optical depth to the stellar radiation is 1) of the inner rim versus distance from the central star for different values of ϵ. The curves are plotted for a star with $T_\star = 10\ 000$ K, $M_\star = 2.5\ M_\odot$, $L_\star = 47\ L_\odot$. This figure is taken from Isella et al. (2005).

Fig. 1.12 shows the synthetic image of the curved and vertical rim plotted by Isella & Natta (2005). Both vertical and curved rim emit most of their radiation in the near and mid-IR. Contrary to the vertical rim (Fig. 1.12-right), for curved rims (Fig. 1.12-left) the near-IR excess does not depend much on the inclination, being maximum for face-on objects and only partially smaller for highly inclined ones. This is consistent with

the observed near-IR between objects seen face-on and close to edge-on (Isella & Natta (2005)).

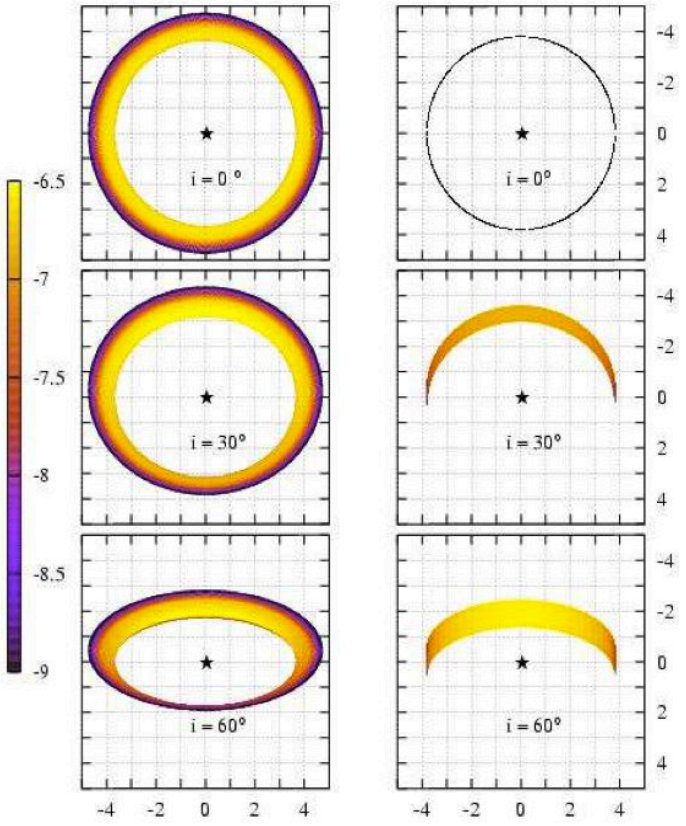

FIGURE 1.12: Synthetic images of the curved rim (left) the vertical rim (right) for different values of inclination angles. This figure is taken from Isella et al. (2005)

Kama et al. (2009) studied the detailed physics of the inner rim using a radiative transfer code. However, detailed study of inner rim needs also a hydrodynamical model. Kama et al. (2009) showed that the inner rim could not be a sharp wall and it should be rounded. They also showed that high surface densities and large silicate grains decrease the rim radius.

In case a dust grain can not cool in every direction, its temperature increases because of backwarming. The IR radiation that one grain emits can be absorbed by another grain. This is the backwarming meaning. A dust grain in an optically thick region is immersed in the IR emission, while a grain in an optically thin region receives only half of the sky dust IR emission. In Kama et al. (2009), the backwarming factor is defined, i.e., C_{bw} that is proportional to the square of the radius of the inner rim of the disk:

$$\pi \frac{L_\star}{4\pi R_{rim}^2} = \frac{4\pi}{C_{bw}} \epsilon \sigma T_d^4 \tag{1.41}$$

Eq. 1.41 is a result of equating the energy absorbed by a grain at a distance R_{rim} from the central star with luminosity of $L_\star$ and the energy emitted by a grain when the temperature of the grain is T_d . ϵ is the cooling efficiency and C_{bw} is a quantity that can be determined by solving complex radiative transfer (Kama et al. 2009).

In an optically thin environment for C_{bw}=1 grains have the smallest possible distance from the central star. This value for C_{bw} has been used by e.g. Monnier & Millan-Gabet (2002) to determine the smallest distance of the grains from the central star.

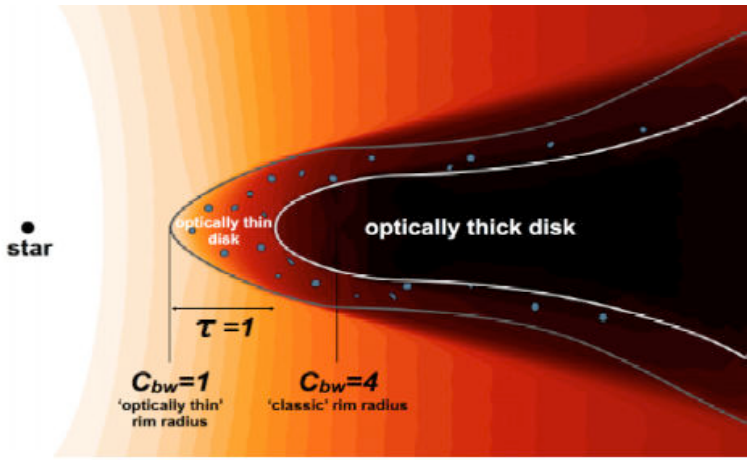

FIGURE 1.13: A schematic view of the inner rim of the disk. The colour map shows the range of temperatures, from <300 K (dark regions) to >2000 K (white regions). For C_{bw} = 1 where the disk is optically thin, dust starts condensing. C_{bw} = 4 (for a classical rim) is a maximum backwarmed dust wall (Kama et al. 2009).

DDN2001 adopted C_{bw} = 4 assuming a rim with optically thick vertical wall. This shows how backwarming can change the distance of the rim from the central star. The optically thin region in front of the rim is illustrated by Fig. 1.13.

1.7.1 Transitional and Pre-transitional Disks

Several disks have been recently detected with a notable deficit of flux in the near- and mid- infrared (2 –20 μm) compared to disk of other Herbig stars, e.g. Bouwman et al. (2003). The lack of near- and mid-infrared flux in these disks could be indicative of the removal of the hot dust or warm dust close to the star which emits at near-IR and mid-IR wavelengths respectively, and the presence of inner disk holes or gaps.

A few years ago, a new class of disk was identified. These disks are so called "pre-transitional disks" and they have gaps within their disks, which is different from the inner holes observed in transitional disks (Espaillat et al. 2007b). In these disks there is lack of mid-infrared flux (5 –20 μm) and significant emission beyond 20 μm (Fig. 1.14).

To create the inner disk holes and gaps in transitional disks and pre-transitional disks several mechanisms can be involved. These mechanisms could be due to planet formation, stellar companions, grain growth, magnetorotational instability (MRI) and photoevaporation. The MRI, grain growth and photoevaporation could not explain the gaps seen in the pre-transitional disks around for instance LKCa 15. Based on disk clearing theories, the planet formation is a more important factor to clear the inner disk of pre-transitional disks. HD 100546 is such a pre-transitional disk, which will be discussed in detail in Chapter 4.

FIGURE 1.14: A pre-transitional disk around young star, 2MASS J16042165-2130284. Credit: The Graduate University for Advanced Studies, Japan.

1.8 Radiative transfer

As I mentioned in previous sections, dust plays an important role in the circumstellar disk of YSOs. With high-angular resolution, the basic structural properties such as size, inclination, and surface brightness of the circumstellar environments are now under study. With high-resolution data, from optical to radio, a comprehensive study of the dust can be done using radiative transfer (RT) codes.

Dust grains can efficiently absorb, scatter, and polarise the stellar light at short wavelengths, whereas at longer wavelengths the absorbed light is re-emitted by dust. The amount of scattered and absorbed light is related to the geometry of the circumstellar environment and the properties of the dust. The amount of absorbed radiation determines the temperature of the dust and defines the amount of radiation re-emitted at longer, thermal wavelengths. To understand the structure and evolution of these dusty disks, the evolution of dust grains and their properties, their temperature, or the density profiles, it is very important to model the integrated fluxes, SED, and get the images at different wavelengths and this requires solving radiative transfer problems.

1.8.1 The radiative transfer problem

To solve the RT problem in a dusty disk, one should determine the specific intensity $I_\lambda(\overrightarrow{r}, \overrightarrow{n})$ at each point $\overrightarrow{r}$ and direction $\overrightarrow{n}$ at each wavelength λ. By solving the stationary radiative transfer equation, one can obtain this intensity. For randomly oriented dust grains, the radiative transfer equation is given with the Stokes formalism:

$$\begin{aligned}\frac{dI_\lambda(\overrightarrow{r}, \overrightarrow{n})}{ds} = &- \kappa_\lambda^{ext}(\overrightarrow{r})\, I_\lambda\,(\overrightarrow{r}, \overrightarrow{n}) \\ &+ \kappa_\lambda^{abs}(\overrightarrow{r})\, B_\lambda\,(T(\overrightarrow{r}))\, I_0 \\ &+ \kappa_\lambda^{sca}(\overrightarrow{r})\frac{1}{4\pi}\int\int_\Omega S_\lambda\,(\overrightarrow{r}, \overrightarrow{n}', \overrightarrow{n})\;\, I_\lambda\,(\overrightarrow{r}, \overrightarrow{n}')\, d\Omega',\end{aligned} \tag{1.42}$$

where $I_\lambda\,(\overrightarrow{r}, \overrightarrow{n})$ = (I,Q,U,V) is the Stokes vector, I is the total intensity, Q and U are the linearly polarised intensities, and V is the circularly polarised intensity. $\kappa_\lambda^{abs}(\overrightarrow{r})$, $\kappa_\lambda^{sca}(\overrightarrow{r})$ and $\kappa_\lambda^{ext}(\overrightarrow{r}) = \kappa_\lambda^{abs}(\overrightarrow{r}) + \kappa_\lambda^{sca}(\overrightarrow{r})$ are the absorption, scattering and extinction opacities, respectively. $S_\lambda\left(\overrightarrow{r}, \overrightarrow{n}'\overrightarrow{n}\right)$ is the 4×4 scattering matrix, which explains the changes in the Stokes vector scattering the light from direction $\overrightarrow{n}'$ to the direction $\overrightarrow{n}$. s is the length along the direction of propagation. $B_\lambda\,(T(\overrightarrow{r}))$ is the Planck function and I_0 is the unitary Stokes vector, which shows an unpolarised emission of I_0 = (1,0,0,0)[2].

To obtain the dust thermal emission, one needs to set the dust temperature structure $T(\overrightarrow{r})$ taking into account the radiative equilibrium. Assuming dust in local thermodynamic equilibrium and the radiation field as the only source of energy, the temperature is calculated solving the following equation:

$$\int_0^\infty \kappa_\lambda^{abs}(\overrightarrow{r})\, B_\lambda\,(T(\overrightarrow{r}))\;\, d\lambda = \int_0^\infty \kappa_\lambda^{abs}(\overrightarrow{r})\, J_\lambda\, d\lambda, \tag{1.43}$$

where J_λ is the mean specific intensity.

Owing to the dust optical properties (κ_λ^{abs}, κ_λ^{sca}, S_λ) and sources of radiation (initial conditions for Eq. (1.42)), the Eqs . (1.42) and (1.43) can define the RT problem. Note that the opacities can be dependent on the temperature, in this case solving Eqs. (1.42) and (1.43) needs an iterative scheme.

Moreover, radiative transfer has an important role in the physics of the disk. It modifies the density structure through hydrostatic equilibrium and affects the dust quantity and its opacity.

[2]Since the dust particles are randomly oriented, the net dust thermal emission is not polarised.

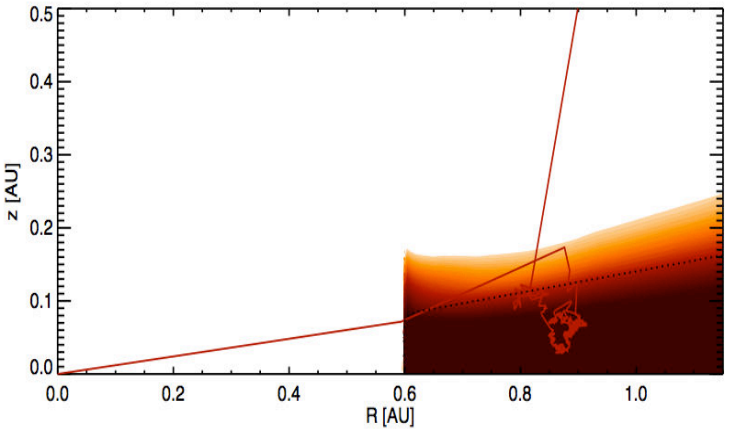

FIGURE 1.15: Propagating a photon package through a disk. A photon package propagates through the disk until it exits from the grid. Credit: from thesis of G. D. Mulders.

1.8.2 Monte Carlo radiative transfer: MCFOST

MCFOST is a 3D continuum and line radiative transfer code based on the Monte Carlo method (Pinte et al. 2006). In a Monte Carlo method a probabilistic approach is taken to solve the radiative transfer equation. The photon packets from the central star are propagated through the disk to set its temperature (Fig. 1.15). Taking into account the scattering, absorption and emission of the photon packets in the disk, the SED and/or synthetic images are bulit.

MCFOST computes the temperature and the SEDs/images with a two-step processes:

-**Step 1**: determining the temperature distribution. When photon packets are produced at the stellar photosphere, they propagate through the disk until they exit the grid. By scattering, the orientation of the packet is changed but not its wavelength. By absorption, packets are re-emitted at once but at a different wavelength, calculated based on the temperature of the cell. For re-emission process, the temperature correction method proposed is used by Bjorkman & Wood (2001). In this step, all photon packets have a similar energy and are randomly scattered/absorbed within the disk. The concept of mean intensity proposed by Lucy (1999) is used to decrease noise in the temperature estimation for optically thin cases.

-**Step 2**: gives the SED and/or images from the temperature calculated in step 1. In this step, the number of photon packets is assumed to be constant at all wavelengths. This code uses a spherical or cylindrical grid, with an adaptive mesh filtering at the inner edge to properly sample the inner radius of the disk.

We used this code in order to reproduce our new PIONIER/VLTI data. This code is used in Chapter 4. For a comparison with other 2D radiative transfer codes, see Pinte et al. (2009).

Chapter 2

An introduction to optical/IR interferometry

2.1 Why Spatial Interferometry?

Since the times of Galileo Galilei (1564-1642), astronomers have tried to increase the size of their telescopes to improve the quality of the observations. A question might come in mind: why and how does increasing the size of telescopes could improve the quality of the observations. Let's consider a single telescope. According to Fig. 2.1, the diameter of the telescope is called "D_1". We know that an ideal optical system would image a point object perfectly as a point. However, due to the wave nature of light, diffraction occurs, caused by the limiting edges of the system aperture stop. The result is that the image of a point is a blurred spot, no matter the lens quality. This is the diffraction blurred spot or Airy disk as is seen in the right part of Fig. 2.1, named in honor of Lord George Biddel Airy, a British mathematician (1801–1892). The blurred spot size is proportional to the wavelength, the diffraction effect can often become the limiting factor. If the aperture of the lens is circular, approximately 84 % of the energy from an imaged point is spread over the central disk surrounded by the first dark ring of the Airy pattern. The angular diameter of this central disk, which is the Full Width at Half Maximum (FWHM) of airy patern i.e, "σ", in radian is

$$\sigma = 2.44\frac{\lambda}{D_1} \tag{2.1}$$

Where λ/D_1 is the angular resolution of the telescope. The angular resolution of a single telescope is defined as ability to distinguish between two point sources. A smaller size

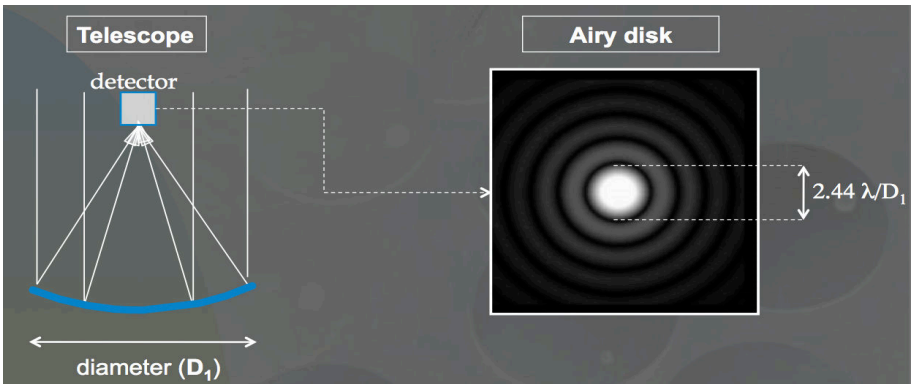

FIGURE 2.1: The image of an unresolved star looks like a blurred spot. Credit: talk of J. Surdej in VLTI school.

of the airy disk causes a better image of the star in the sky. In order to decrease the angular diameter of the airy disk, we need to work on shorter wavelength ranges or to increase the size of telescope.

According to Fig. 6.2, increasing the diameter of the telescope from D_1 to D_2 the size of airy disk decreases.

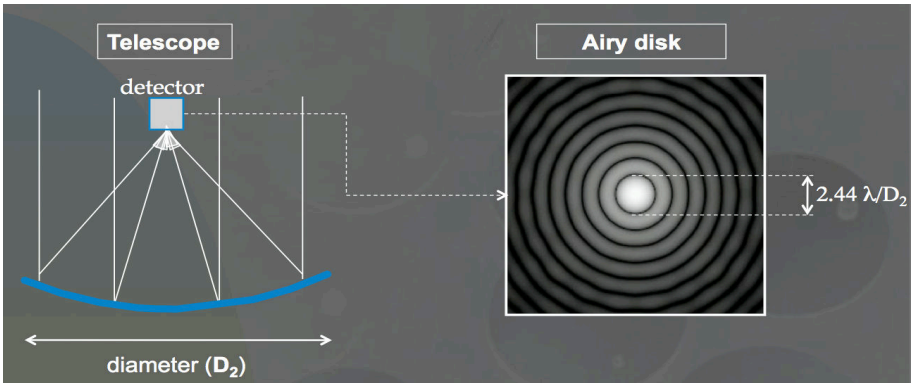

FIGURE 2.2: The image of an unresolved star still looks like a blurred spot. Credit: talk of J. Surdej in VLTI school.

Telescope diameters have grown from Galileo's telescope of a few centimetres to the current 10-m class of telescopes represented by the Keck Telescopes and 8-m for ESO's Unit Telescopes. In all this time, the basic idea has not changed: the telescope as an optical system produces an image in the focal plane that is taken as a representation of the object shape. We see that the size of the telescope sets a limit on the spatial resolution of the images. As there is a practical limit to telescope sizes, we can not achieve resolutions beyond that limit.

2.1.1 The Electromagnetic field

When we look at the field of radiation, we may represent it as being composed of many trains of waves propagating with light velocity. For simplicity, we consider a monochromatic wave train, which is linearly polarized and propagating along the z direction. The electric field of such a radiation field can be represented by a cosine function as following:

$$E(z,t) = a\ cos\,(2\pi(\nu t - z/\lambda)) \tag{2.2}$$

where a is the real magnitude as is shown in Fig. 2.3, ν is the frequency of the waves and λ is the wavelength. If we consider a position of the observer along the z axis, so that assuming z=0, the radiation field only varies with time. In this case the distance between two successive maxima (see Fig. 2.3) is defined as a period and one period is equal to $1/\nu$. Now if we freeze the time (t=0), then the electric field varies as a function of distance. In this case, the distance between two successive maxima is one λ. The relation between λ and the period (T) is very simple. During the time of wave period, the light wavelength at the velocity of the light speed is:

$$\lambda = cT \tag{2.3}$$

The electric function, Eq. 2.2, can be written in complex notation as:

$$V(z,t) = Re(a\ exp\,[i2\pi(\nu t - z/\lambda)]) \tag{2.4}$$

The reason why we use the complex representation is that we can easily separate the time and space variables:

$$V(z,t) = Re(a\ exp\,[-i2\pi z/\lambda]\ exp\,[i2\pi\nu t]) \tag{2.5}$$

From now, we represent the electric field as a complex notation but at the end we consider the real part of the equation. We can write Eq. 2.5 as:

$$V(z,t) = A\ exp\,[i2\pi\nu t]\,, \tag{2.6}$$

where A= $a\ exp\,[-i2\pi z/\lambda]$ is called the complex magnitude. Unfortunately in practice, it is impossible to directly measure the amplitude variation (the wave pulsation) in the optical wavelengths, because the frequency of the waves is too large at these wavelengths

and there is no detector to respond that rapidly. Heterodyne methods allow this measure in the mid-IR (see ISI Berekely interferometer) and in the radio wavelengths , it is possible to measure the amplitude because the frequency is much lower than in the optical.

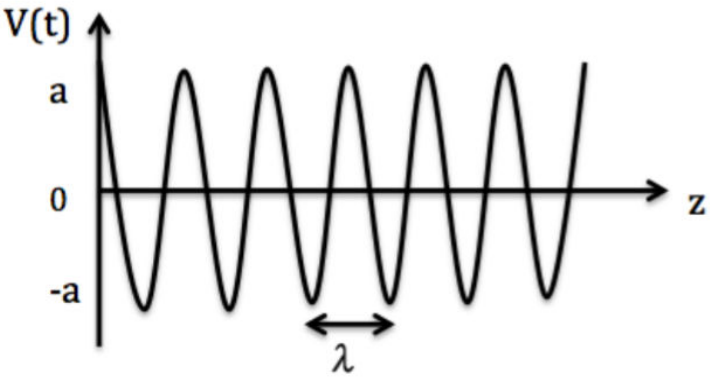

FIGURE 2.3: A schematic of the electric wave propagation. I have plotted it.

What astronomers are currently able to measure for all wavelengths, is the intensity (I) of the electric field, which is a time average of the quantity of the energy per second, per cm^2, per solid angle unit, i.e, $< V^2(t,z) >$ or $< V(t,z) \times V^*(t,z) >$, $V^*(t,z)$ is the conjugate of the electric field,:

$$I =< V(t,z) \times V^*(t,z) >= \frac{1}{2T} \int_{-T}^{+T} V(t,z) \times V^*(t,z) dt, \tag{2.7}$$

From Eq. 2.7, $V(t,z) \times V^*(t,z)$ will be equal to AA^* where A^* is the conjugate of complex amplitude. Consequently, we will have:

$$I = AA^* =\mid A \mid^2 = a^2, \tag{2.8}$$

where $\mid A \mid^2$ is the squared value of the modulus of the complex magnitude, which is equal to the squared value of the real magnitude.

2.1.2 The Young's experiment

This is the classical diffraction experiment named after Thomas Young who conducted it in 1802, providing the experimental vital element for the demonstration of the wave nature of light. In its simplicity it is perfectly suited to explain the concept of stellar interferometry.

A simple schematic of the experiment is shown in Fig. 2.4.

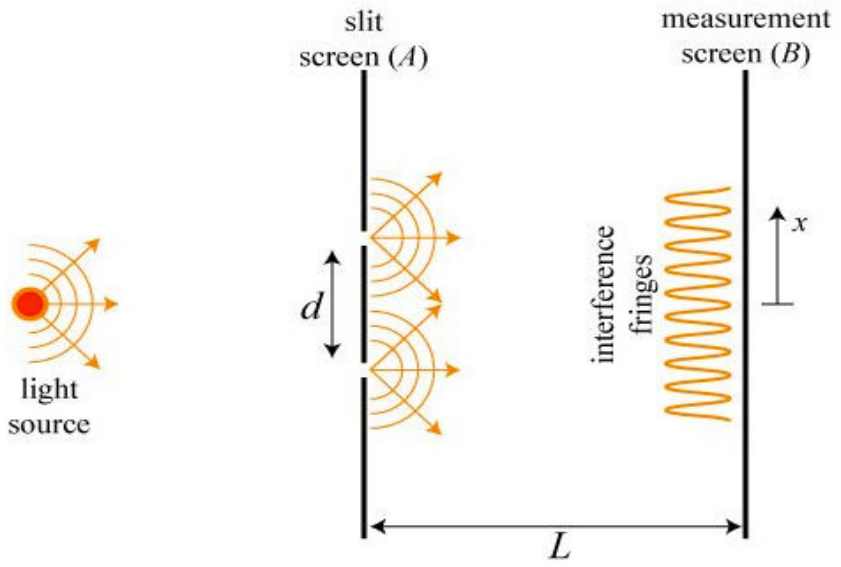

FIGURE 2.4: A scheme of the young's experiment. Credit from teach astronomy website.

A light source is positioned some distance behind a screen A which possesses a pair of closely spaced narrow slits. Light emerges from the pinholes and spreads as spherical waves; the waves overlap, and the interference pattern produced is projected on a measurement screen B. As we showed in previous section, the measurable quantity of the electric field on the screen B is the intensity, which is the squared real amplitude.

A simulation of the pattern of light which would be observed on the screen B is shown in Fig. 2.5.

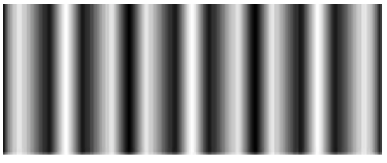

FIGURE 2.5: A simulation of the pattern of light on the screen B. Credit: Sebastien Flament.

One should see bright lines of light, where the light from the two slits constructively interferes and the dark lines where the light destructively interferes. Let us assume that the source produces a monochromatic (single-wavelength) wave which hits the two slits at the same time, so that the peaks of the wave arrive at the two slits simultaneously. The two waves are then said to be in phase with one another.

The distance L between the screens is large (Fig. 2.4), so that the paths of light from pinholes P and Q to a point on the measurement screen are nearly parallel (see Fig. 2.6). The difference in phase can then be calculated as in Fig. 2.6.

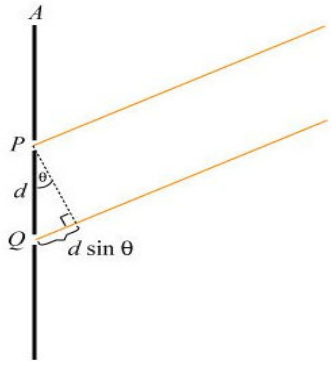

FIGURE 2.6: A schematic of pinholes. Credit from teach astronomy website.

Assuming the two paths meet at the observation screen, light emerging from pinhole Q must travel a distance d sin θ farther than light from pinhole P. Assuming monochromatic light of wavenumber k=$2\pi/\lambda$, the light from the two pinholes arrives at the screen with a relative phase difference:

$$\phi = \frac{2\pi}{\lambda} dsin\theta, \tag{2.9}$$

two waves are out of phase and produce destructive interference when phase is an odd multiple of π , i.e.

$$\frac{2\pi}{\lambda} dsin\theta = (2n+1)\pi, \qquad n = 0, 1, 2, 3, ... \tag{2.10}$$

and produce constructive interference when the phase is an even multiple of π, i.e.

$$\frac{2\pi}{\lambda} dsin\theta = 2n\pi, \qquad n = 0, 1, 2, 3, ... \tag{2.11}$$

A little more geometry demonstrates that sin$\theta \approx$ x/L, so that bright fringes occur at positions

$$x = n\ L\lambda/d \tag{2.12}$$

The distance between two successive bright fringes on the screen is given by:

$$\Delta x = L\lambda/d, \tag{2.13}$$

when $\Delta x/L = \lambda/d$ is an angle is called the angular resolution of the instrument when we discussed it in Sect. 2.1. According to Fig. 2.7 , the smallest angular separation of a source, which can be observed by an instrument is the angular resolution.

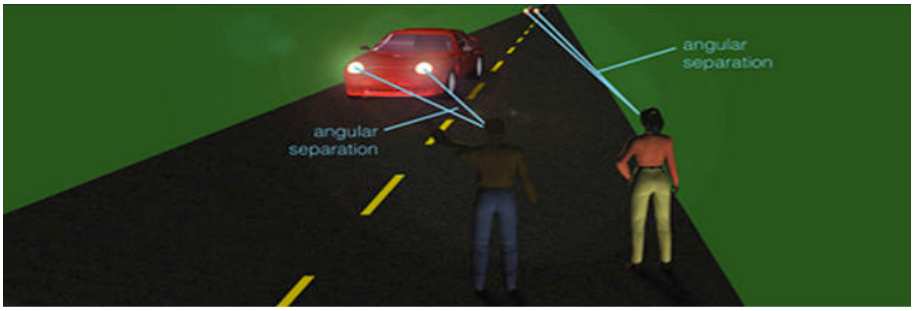

FIGURE 2.7: A schematic of angular separation. *Credit* : *http* ://*www.abovetopsecret.com*/*forum*/*thread*1072484/*pg*1.

The instrument could be the human eye, which has an angular resolution of 1 arcminute.

2.1.3 The Fizeau Interferometry

Perhaps the most basic technique of interferometry is Fizeau interferometry, named after Hippolyte Fizeau (1819-1896), a French physicist who first suggested to use interferometry to measure the size of stars by masking the telescope aperture with two small pinholes. According to Fig. 2.8, the light of a point star passing through the pinholes would then interfere in the telescope focal plane.

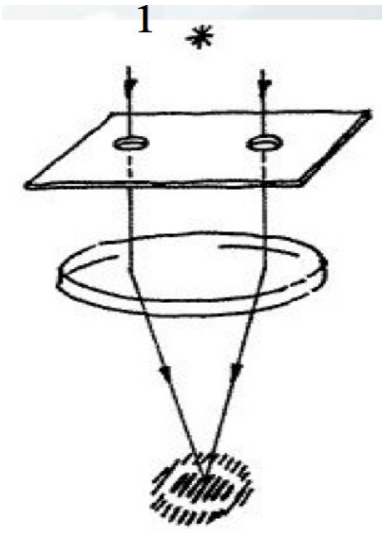

FIGURE 2.8: A sketch of Fizeau Interferometry. Credit: talk of J. Surdej in VLTI school.

If we cover the right hole, the left hole would be as a very small telescope with diameter of for instance "d". In this case, an airy pattern with an angular size of 2.44 λ/d will

be formed in the detector plane. If we uncover the right hole and cover the left one, we obtain the same airy pattern was formed in the same location by left hole in the detector plane.

Now, if we uncover both holes, we expect to see only the superposition of two airy disks. But according to Young's experiment (see Sect. 2.1.2) in addition, we will obtain interference fringes where the angular separation of the white fringes are λ/B, whit B the distance between the two holes.

Fizeau suggested the method to observe the close binaries. When the binary separation is too small, the airy disks of the two stars would be superimposed each other, it is equivalent to observing one single star, so that we can not resolve the binary. In this case, interfering the coherent light causes bright fringes inside of the airy patterns. Increasing the binary separation up to $\lambda/2B$, the fringes will disappear (see Fig. 2.9). With this method, it would be possible to estimate the angular binary separation.

Fizeau then proposed the following equation that is defined the contrast of the fringes:

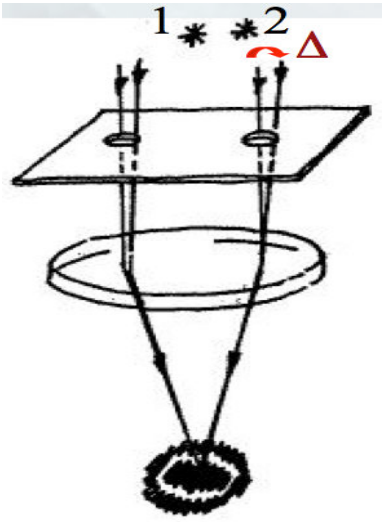

FIGURE 2.9: A sketch of Fizeau Interferometry. Credit: talk of J. Surdej in VLTI school.

$$C = \frac{I_{max} - I_{min}}{I_{max} + I_{min}} \tag{2.14}$$

where I_{min} and I_{max} denote the minimum and maximum intensity of the fringes. the intensity I is measured by Eq. 2.7. According to Eq. 2.15, if the star is unresolved, then the value of I_{min} would be close to zero. In this case the contrast goes to roughly 1 as Fig. 2.10:

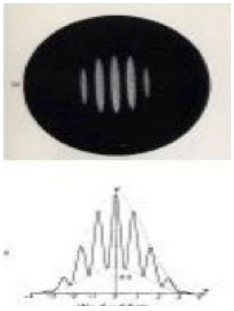

FIGURE 2.10: A schematic of the contrast of the light. Credit: talk of J. Surdej in VLTI school.

If the star is an extended source, then we resolve it. In this case I_{min} would be close to I_{max}, so that the contrast goes to zero as in Fig. 2.11:

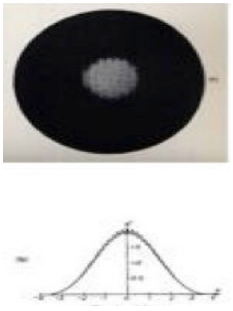

FIGURE 2.11: A schematic of the contrast of the light. Credit: talk of J. Surdej in VLTI school.

Due to insurmountable technical problems with the mechanical stability at larger pinhole separations, spatial interferometry was abandoned in the late 1920's.

The first successful measurement using the Fizeau's principle was performed by Albert A. Michelson and Francis G. Pease in 1920 determining the diameter of α Orionis to 0.047 arcsec. This was at a time when the smallest diameter measured with a full aperture was about 1 arcsec, equivalent to the typical seeing value.

In terms of angular resolution, two small telescopes separated by B are equivalent to a single large telescope of diameter B (Fig. 2.12).

This method is similar to the proposition of Fizeau to use a screen composed of two holes on the top of a telescope (lens or mirror) as I explained before. However, in this method, the baseline (B), which separates two telescopes is larger than the separated distance between two holes (d) in Fig. 2.8. Therefore, the angular resolution of the system (two telescopes), λ/B, could be smaller than one using two holes, λ/d. The larger the baseline, the more precise the measurement of the angular size of the objects.

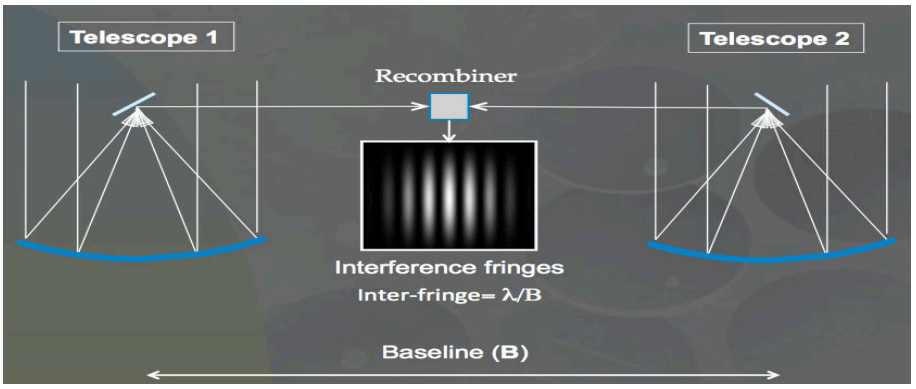

FIGURE 2.12: The sketch of an interferometer. Credit: talk of J. Surdej in VLTI school.

2.1.4 Light coherence

One of the important parameters of illumination sources is their coherence.

Coherence is a measure of the ability of wave functions to interfere the photons with each other.

The theory of the light coherence gives the description in the statistical scenes of the correlation of the electric field at different points in space. So far, in the Young experiment we considered only monochromatic light.

Concerning the coherence of light waves, temporal coherence tells us how monochromatic a source is.

Temporal coherence is a measure of the correlation between the phases of a light wave at different points along the direction of propagation.

So far, we assumed pin-holes and point-like and monochromatic source. If we would work with only monochromatic light, we would obtain very small amount of photons from the star. In this part, instead of working in the monochromatic regime, we work in the so-called quasi-monochromatic regime. The quasi-monochromatic means working within a small spectral band around a specific wavelength, λ or frequency, ν.

Let's assume that our source emits waves in the range $\lambda \pm \Delta\lambda$. Waves with wavelength λ and $\lambda + \Delta\lambda$, which at some point in space constructively interfere, will no longer constructively interfere after some optical path length $l_c = \lambda^2/\Delta\lambda$; l_c is called the coherence length.

To calculate the coherence length, we start with the definition of the electric field from Eq. 2.4 :

$$V(z,t) = \int_{\lambda+\Delta\lambda}^{\lambda-\Delta\lambda} a(\lambda^{'})exp(i2\pi(ct/\lambda^{'} - z/\lambda^{'}))d\lambda^{'}, \tag{2.15}$$

In Eq. 2.16, we add all the contributions within the small spectral range around λ. In this case $V(z,t)$ will be:

$$V(z,t) = A(z,t)exp(i2\pi c/\lambda(t - z/c)), \tag{2.16}$$

where

$$A(z,t) = \int_{\lambda+\Delta\lambda}^{\lambda-\Delta\lambda} a(\lambda^{'})exp(i2\pi c((\lambda - \lambda^{'})/\lambda\lambda^{'})(t - z/c))d\lambda^{'}, \tag{2.17}$$

assuming that the real amplitude, $a(\lambda^{'})$ is constant, so that $a(\lambda^{'}) = a_0$, we will have:

$$A(z,t) = a_0 \frac{sin(-2\pi c(t - z/c)\Delta\lambda/\lambda^2))}{\pi(t - z/c)}, \tag{2.18}$$

Freezing the time, i.e, $t = 0$, the space variation of the complex amplitude in the z direction will be equal to $\lambda^2/\Delta\lambda$, which is called l_c, i.e, coherence length.

In Eq. 2.19, if we substitute $\Delta\lambda$ to $\Delta\nu$, we will have:

$$A(z,t) = a_0 \frac{sin(2\pi\Delta\nu(t - z/c)))}{\pi(t - z/c)}, \tag{2.19}$$

Eq. 2.20 shows that the complex amplitude varies in time with a frequency of $\Delta\nu$, which is much lower than the frequency of vibration ν.

The time of coherence for a coherence length of l_c is then $1/\Delta\nu$, which is the period of a packet of the coherent light.

2.1.5 Complex degree of mutual coherence

In a further step, keeping the assumption of pin-holes of Young experiment, we assume that the source is quasi-monochromatic and extended. According to the Fig. 2. 13, we consider first a point source, which is at infinite distance of two similar pin-holes, P_1 and P_2. V_1 and V_2 are the electric waves in pin-holes P_1 and P_2 respectively. The observing screen, q, is located at a specific distance of pin-holes. We wonder what the intensity of the source in the quasi-monochromatic regime is at the location of q.

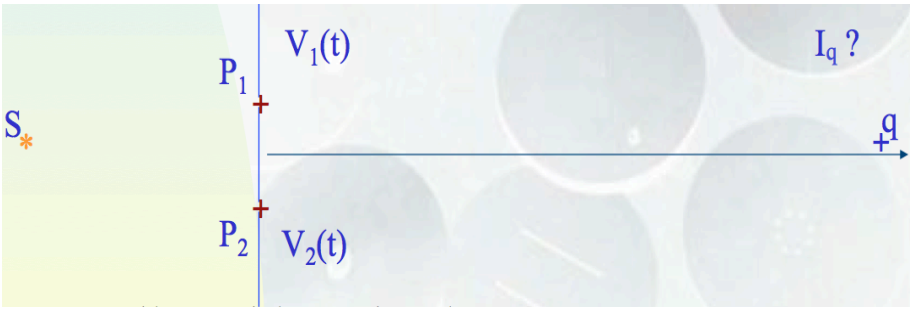

FIGURE 2.13: A schematic of a simple interferometer for a point source. Credit: talk of J. Surdej in VLTI school.

As we showed in Eq. 2.7, the intensity of light is the average of the electric field multiplied by its conjugate. The intensity at the location of q is:

$$I_q =< V_q^*(t)V_q(t) >, \tag{2.20}$$

where

$$V_q = V_1(t) + V_2(t-\tau) \tag{2.21}$$

In Eq. 2.22, τ is the time difference between the light wave coming from the pin-holes at the location of q and is called optical delay.

Consequently, combining Eq. 2.21 and 2.22 we have:

$$I_q =< V_1^*(t)V_1(t) > + < V_2^*(t-\tau)V_2(t-\tau) > + < V_1^*(t)V_2(t-\tau) > + < V_1(t)V_2^*(t-\tau) >, \tag{2.22}$$

where the term of $< V_1^*(t)V_1(t) >$ is equal to the intensity, I_1, which is due to the hole P_1. Although the term of $< V_2^*(t-\tau)V_2(t-\tau) >$ has been translated by τ, since we take the time average, it would be equal to the intensity I_2, which is due to the hole P_2. Since we assumed that pin-holes are the same size, so that the $V_1(t)$ and $V_2(t)$ are the same as well. We conclude that:

$$I_2 = I_1 = I \tag{2.23}$$

In Eq. 2.23, we have additional terms of $< V_1^*(t)V_2(t-\tau) >$ and $< V_1(t)V_2^*(t-\tau) >$. To find out these terms, we remind simply the relation of complex quantities. Suppose that we have two complex quantities:

$$\xi_1 = a_1 + ib_1 \quad and \quad \xi_2 = a_2 + ib_2, \tag{2.24}$$

where a_1 and a_2 are real parts of complex quantities and b_1 and b_2 are the imaginary ones. Now the expression of $\xi_1^*\xi_2 + \xi_1\xi_2^*$ will be equal to:

$$2Re(\xi_1^*\xi_2) = 2Re(\xi_1\xi_2^*) \tag{2.25}$$

From Eq. 2.26, one can conclude that the terms of $< V_1^*(t)V_2(t-\tau) > + < V_1(t)V_2^*(t-\tau) >$ will be:

$$2Re(< V_1^*(t)V_2(t-\tau) >) \tag{2.26}$$

Consequently, I_q in Eq. 2.23 will be:

$$I_q = I + I + 2IRe(\gamma_{12}(\tau)), \tag{2.27}$$

where the expression of $2IRe(\gamma_{12}(\tau))$ is the interference term of the light and $\gamma_{12}(\tau)$ is:

$$\gamma_{12}(\tau) =< V_1^*(t)V_2(t-\tau) > /I, \tag{2.28}$$

the quantity of $\gamma_{12}(\tau)$ is the time average of the cross correlation product divided by the intensity, which is called the complex degree of mutual coherence. This quantity gives the idea of how light waves correlate between each other at two different places in space.

Combining Eq. 2.6 and Eq. 2.29, one can write:

$$\gamma_{12}(\tau) =< A_1^*(z,t)A_2(z,t-\tau) > exp(-i2\pi\nu\tau)/I, \tag{2.29}$$

If the time difference between two beams is equal to zero, Eq. 2.30 will be:

$$\gamma_{12}(\tau = 0) =< A_1^*(z,t)A_2(z,t) > /I, \tag{2.30}$$

which can be written with their modulus as following:

$$\mid \gamma_{12}(\tau = 0) \mid = \mid < A_1^*(z,t)A_2(z,t) > /I \mid \tag{2.31}$$

Now, if we take the modulus of $\gamma_{12}(\tau)$ from Eq. 2.30, we will have:

$$\mid \gamma_{12}(\tau) \mid = \mid < A_1^*(z,t)A_2(z,t-\tau) > /I \mid, \tag{2.32}$$

assuming that the time difference of two beams is much smaller than the time of coherence, i.e, $\tau \ll 1/\Delta\nu$, we can write:

$$\mid \gamma_{12}(\tau) \mid = \mid \gamma_{12}(\tau = 0) \mid, \tag{2.33}$$

on the other hand, $< A_1^*(z,t)A_2(z,t-\tau) > /I$ can be written as:

$$< A_1^*(z,t)A_2(z,t-\tau) > /I = \mid < A_1^*(z,t)A_2(z,t) > /I \mid exp(i\beta_{12}), \tag{2.34}$$

where $exp(i\beta_{12})$ is a phase dependent factor between the two beams. Consequently, we can rewrite Eq. 2.30 as:

$$\gamma_{12}(\tau) = \mid \gamma_{12}(\tau = 0) \mid exp(i\beta_{12} - i2\pi\nu\tau), \tag{2.35}$$

Combining Eq. 2.28 and 2.36, one can write:

$$I_q = 2I(1+ \mid \gamma_{12}(\tau = 0) \mid cos(\beta_{12} - 2\pi\nu\tau)), \tag{2.36}$$

In this step, we are able to find out the expression of visibility defined by Fizeau (Eq. 2.15) using the intensity in Eq. 2.37. According to Eq. 2.37, I_{max} is equal to $2I(1+ \mid \gamma_{12}(\tau = 0) \mid)$ and I_{min} is equal to $2I(1- \mid \gamma_{12}(\tau = 0) \mid)$. Therefore, from Eq. 2.15 we have:

$$V = \frac{I_{max} - I_{min}}{I_{max} + I_{min}} = \frac{4I \mid \gamma_{12}(\tau = 0) \mid}{4I} = \mid \gamma_{12}(\tau = 0) \mid, \tag{2.37}$$

which is an interesting result to relate an observable quantity to the complex degree of mutual coherence. If we observe an unresolved object, i.e, I_{min}=0, the modulus of complex degree of mutual coherence would be equal to 1. If we resolve an object, i.e, I_{max}=I_{min}, the modulus of complex degree of mutual coherence would be equal to 0. Indeed, there is a relation between the modulus of the complex mutual coherence and angular structure of the source. In this part, we focus on establishing this relation considering an extended source:

Van Cittern Zernike theorem: Let's assume that considering two pin-holes, the source is extended. In fact, the source is composed of several elements, which emit in an incoherent way. According to Fig. 2.13, the electric field at hole 1 is called $V_1(t)$ and that at hole 2 is called $V_2(t)$. Now, we are wondering what would be the distribution of the intensity in the screen q for an extended source (see Fig. 2.14). To do that, we need to evaluate the following expression of the complex degree of mutual coherence for a time delay of τ=0 according to Eq. 2.36:

$$\gamma_{12}(\tau = 0) = < V_1^*(t)V_2(t) > /I \tag{2.38}$$

To proceed from Eq. 2.39, we suppose that $V_1(t)$ and $V_2(t)$, the electric fields, are summation on all the surface elements visible from the hole number one and the hole number two as following:

$$V_1(t) = \sum_{i=1}^{N} V_{i1}(t) \tag{2.39}$$

$$V_2(t) = \sum_{i=1}^{N} V_{i2}(t) \tag{2.40}$$

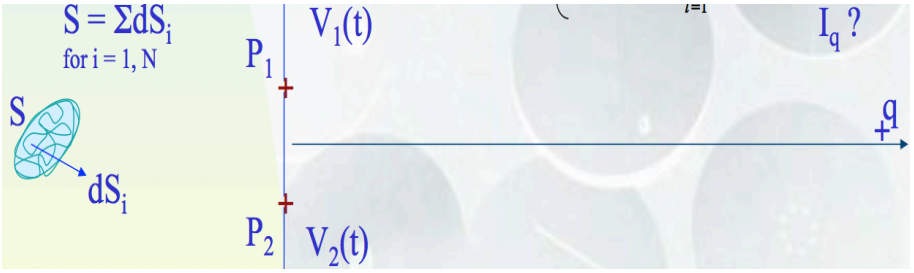

FIGURE 2.14: A scheme of the extended source with two similar pine holes. Credit: talk of J. Surdej in VLTI school.

Now, we insert Eq. 2.40 and 2.41 into Eq. 2.39, then the following expression comes out:

$$\gamma_{12}(\tau = 0) = \left[\sum_{i=1}^{N} < V_{i1}^{*}(t) V_{i2}(t) > + \sum_{i \neq j}^{N} < V_{i1}^{*}(t) V_{j2}(t) > \right] / I \tag{2.41}$$

In Eq. 2.42, the first expression is summation of the electric fields for each individual elements. In the second expression, which is summation of the electric field for $i \neq j$, all the elements are emitting like in incoherent way and the fringes are destructive, so that we neglect the second expression.

Therefore, from Eq. 2.42 remains the following quantity:

$$\gamma_{12}(\tau = 0) = \sum_{i=1}^{N} < V_{i1}^{*}(t) V_{i2}(t) > / I \tag{2.42}$$

In this step, we recall the expression of the electric field evaluated at the hole number one and the hole number two coming from the source element i:

$$V_{i1}(t, \nu r_{i1}/c) = (a_i(t - r_{i1}/c)/r_{i1}) \; exp(2\pi i \nu (t - r_{i1}/c)) \tag{2.43}$$

$$V_{i2}(t, \nu r_{i2}/c) = (a_i(t - r_{i2}/c)/r_{i2}) \; exp(2\pi i \nu (t - r_{i2}/c)) \tag{2.44}$$

Where, a is the real amplitude, which depends on the time, t. We divided a by r_{i1} in Eq. 2.44, which is the distance between the hole number 1 and the surface element i just to account for the dilution of the radiation field, because the intensity scales as square of the modulus of amplitude, so we find out that it is in principle proportional to the square of the distance. The complex exponential function in Eq. 2.44 depends on time and the distance between hole number one and the surface element i. we have the same for Eq. 2.45.

Therefore, the expression of $V_{i1}^{*}(t, \nu r_{i1}/c)V_{i2}(t, \nu r_{i2}/c)$ in Eq. 2.43 will have the following product:

$$V_{i1}^{*}(t, \nu r_{i1}/c)V_{i2}(t, \nu r_{i2}/c) =\mid a_i(t - r_{i1}/c) \mid^2 /(r_{i1}r_{i2})\, exp(-2\pi i\nu(r_{i2} - r_{i1})/c) \quad (2.45)$$

In the squared real amplitude, we assume that r_{i1} is equal to r_{i2} since the distances from the different parts of extended source to the detector is almost infinity. We can express the quantity of $\mid a_i(t - r_{i1}/c) \mid^2$ as a function of the intensity of the source. In the exponential function of Eq. 2.46, we have the difference between the distances between the surface element of the source i and the hole number one and two.

As long as the difference between the two paths of the light, i.e, $r_{i2} - r_{i1}$ is smaller than the length of the coherence of the light (see Sect. 2.1.4):

$$\mid r_{i2} - r_{i1} \mid \leq c/\Delta\nu = \lambda^2/\Delta\lambda = l \quad (2.46)$$

and inserting Eq. 2.46 to the summation in Eq. 2.43 and then replacing the summation by an integration one can write:

$$\gamma_{12}(\tau = 0, (r_{i2} - r_{i1})/\lambda)) = \int_s \frac{I(s)}{r_1 r_2} exp(-2\pi i((r_{i2} - r_{i1})/\lambda))ds/I \quad (2.47)$$

Where $I(s)ds$ is equal to $\mid a_i(t - r_{i1}/c) \mid^2 ds$, the intensity of the source times by the size surface element. Indeed, Eq. 2.48 is the theorem of Zernicke-van Cittert. The Van Cittert–Zernike theorem is a formula in coherence theory, which states that under certain conditions the Fourier transform of the degree of the coherency of the light in the sky is equal to its complex visibility.

The distance between the source and the interferometer is much much larger than the separation between the two telescopes and also than the size of the source. Therefore, we shall approximate the expression of Eq. 2.48 to have more precise results.

According to Fig. 2.15, we assume a source element i located at coordinates ($X^{'}$, $Y^{'}$, $Z^{'}$) and with a distance $Z^{'}$ from an interferometer with two telescopes with one located at P_1 with (X, Y, 0) coordinates and another one at P_2 with (0, 0, 0) coordinates.

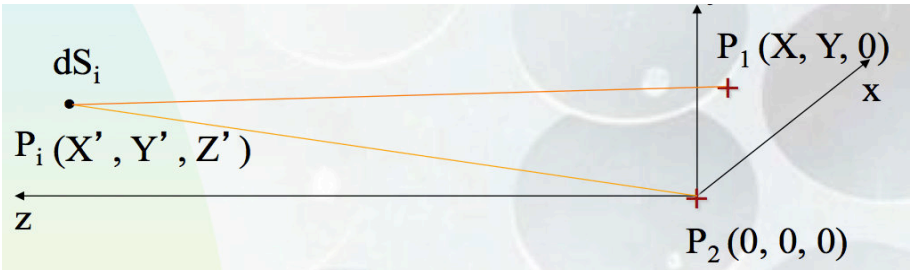

FIGURE 2.15: A schematic of the extended source with two similar pin hols. Credit: talk of J. Surdej in VLTI school.

With these coordinates, we must evaluate the expression of $| r_{i2} - r_{i1} |$ in the exponential term of Eq. 2.48.

To do that, we start with r_{i1} and replace it by the square root of the summation of the square of the difference between all coordinates X, Y and Z as follows:

$$r_{i1} = \sqrt{(X^{'} - X)^2 + (Y^{'} - Y)^2 + (Z^{'})^2}, \tag{2.48}$$

which can be written as:

$$r_{i1} = Z^{'}\sqrt{1 + ((X^{'} - X)^2 + (Y^{'} - Y)^2)/(Z^{'})^2}, \tag{2.49}$$

we use the Taylor series to simplify Eq. 2.50:

$$r_{i1} = Z^{'}(1 + ((X^{'} - X)^2 + (Y^{'} - Y)^2)/2{Z^{'}}^2), \tag{2.50}$$

We calculate the same way for r_{i2}:

$$r_{i2} = Z^{'}(1 + ((X^{'})^2 + (Y^{'})^2)/2{Z^{'}}^2), \tag{2.51}$$

If we make the difference between the two distances r_{i1} and r_{i2}, we will have:

$$\mid r_{i1} - r_{i2} \mid = \mid P_{i1} - P_{i2} \mid = \mid -(X^2 + Y^2)/2Z^{'} + (XX^{'}/Z^{'}) + (YY^{'}/Z^{'}) \mid, \tag{2.52}$$

Replacing $\xi = X^{'}/Z^{'}$ and $\eta = Y^{'}/Z^{'}$, one can rewrite Eq. 2.53 as:

$$\mid r_{i1} - r_{i2} \mid = \mid P_{i1} - P_{i2} \mid = \mid -(X^2 + Y^2)/2Z^{'} + X\xi + Y\eta \mid, \tag{2.53}$$

Replacing the Eq. 2.54 to the argument of Eq. 2.48, the complex degree of mutual coherence would be:

$$\gamma_{12}(0, X/\lambda, Y/\lambda) = exp(-i\phi_{xy}) \int\int_s \frac{I(\xi,\eta)exp(-2\pi i(X\xi + Y\eta)/\lambda))d\xi d\eta}{\int\int_s I(\xi^{'},\eta^{'})d\xi^{'}d\eta^{'}} \tag{2.54}$$

In Eq. 2.55, in the exponential function, $exp(-i\phi_{xy})$, ϕ_{xy} is the phase shift, which only depends on the coordinates, X and Y. $I(\xi,\eta)$ is the intensity as a function of two angular coordinates of ξ and η, which are the angular size of the object in the sky. The only parameters, which are free in Eq. 2.55 are X/λ and Y/λ.

Dividing the intensity, $I(\xi,\eta)$, by the integration of the intensity of the stellar source, the normalized intensity of the source will be as following:

$$I^{'}(\xi,\eta) = I(\xi,\eta) / \int\int_s I(\xi^{'},\eta^{'})d\xi^{'}d\eta^{'} \tag{2.55}$$

We set u=X/λ and v=Y/λ. Reminding that lambda over baseline, i.e, λ/X =λ/B is an angular quantity. The quantities of u=X/λ and v=Y/λ are inverse of this angular coordinate. Therefore, the parameters of u and v represent angular space frequency, which will define the u,v plane and they are correspond to B_x and B_y, i.e., projected baselines respectively.

Setting u,v and using Eq. 2.56, the complex degree of mutual coherence would be:

$$\gamma_{12}(0, u, v) = exp(-i\phi_{u,v}) \int\int_s I^{'}(\xi,\eta)exp(-2\pi i(u\xi + v\eta))d\xi d\eta \tag{2.56}$$

From Eq. 2.57, we find out that the complex degree of mutual coherence is the Fourier transform of the source brightness distribution, which has been normalized. Now, if we take the modulus of $\gamma_{12}(0, u, v)$, which gives the visibility quantity, it would be equal to

the modulus of the Fourier transform of the intensity distribution of the source. Indeed, $\gamma_{12}(0,u,v)$ contains the information on the angular structure of the source. If we do the inverse Fourier transform, then one can find the normalized intensity of the source as follows:

$$I'(\xi,\eta) = exp(i\phi_{u,v}) \int\int_s \gamma_{12}(0,u,v) exp(2\pi i(u\xi + v\eta)) d(u) d(v) \tag{2.57}$$

For each observation and for a specific baseline length, we have information about one direction of the object in the sky, which is correspond to one point in u-v plane. If we observe with many u and v to have a rich u-v plane, then by inverse Fourier transform, we may be able to find what is the distribution of the intensity of the source.

2.1.6 Visibility

Combining the beam of telescopes, the phase component of $\gamma_{12}(0,u,v)$ is lost to atmospheric turbulence and the only good measurable is the modulus of $\gamma_{12}(0,u,v)$, i.e. V (Eq. 2.38).

As an illustration, Fig 2.12-left shows the K-band visibility-amplitude curves as a function of projected baseline length for a Uniform Disk (constant surface brightness profile). A reasonable approximation to the brightness distribution of a resolved star is the model of an uniform disk. The Fourier transform of a symmetrical uniform disk is the first-order Bessel function. The uniform disk is often the model to use when one wants to extract a diameter from a visibility curve.

The visibility curve of a uniform disk model, which is a Bessel function, has several zeros whose positions can be directly related with the diameter. If B_1 is the baseline corresponding to the first zero, then the diameter in milliarcseconds is $\theta \sim \lambda/B_1$. Finding the first zero is of course not mandatory, a χ^2 minimization on a properly sampled visibililty curve is the best way to get an accurate final result. According to Fig. 2.16-left, at short baselines the source looks like a point and the visibility is high. As the baseline increases and the sources begins to get resolved, the visibility drop. At long baselines the Uniform Disk visibility shows ringing because of the presence of a sharp outer edge. Any departure from the uniform disk model, caused for example by limb-darkening or brightening or the presence of a hot spot, should mostly affect spatial frequencies higher than the first null and therefore should require exploration of the second lobe. In Fig. 2.16-right, we do show that the Fourier transform of a Gaussian disk model is a Gaussian. In Figs. 2.17 and 2.18, we do represent the models of a few Herbig stars observed during a large program made by J-P Berger with PIONIER/VLTI (Lazareff et al. 2015 in preparation). In this plot, we do show the squared visibilities

versus spatial frequency for each model. It is obvious that the visibility curve depends on the size of object on the sky. As the object becomes more extended, the visibility curve versus spatial frequency is less extended.

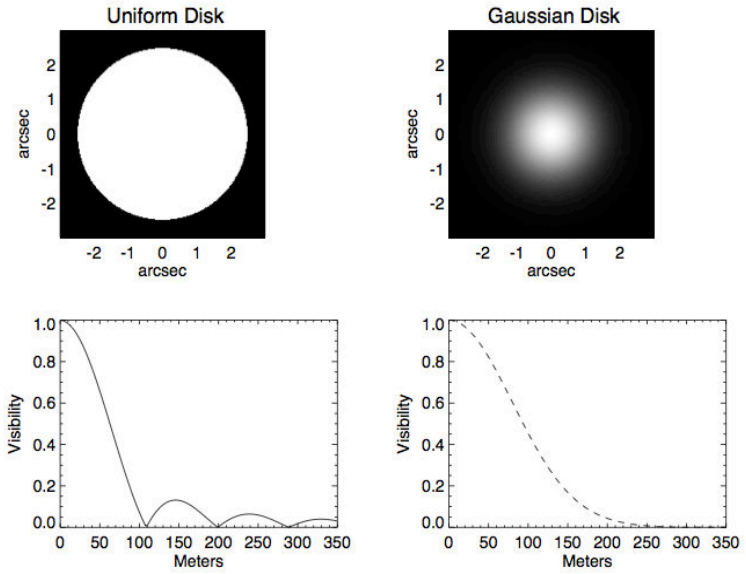

FIGURE 2.16: Illustrative visibility curves versus spatial frequency for a uniform disk (left) and a Gaussian disk (right). Credit: (Tannirkulam, 2008).

A measurement of fringe visibilities can thus be used to constrain surface brightness properties of light sources in the sky and differentiate between various physical models. Interferometers have been successful in measuring stellar diameters (Michelson & Pease [1921]), determining binary orbits, probing the circumstellar environments of young as well as evolved stars (McCarthy & Low [1975]; Millan-Gabet et al. [1999]), and imaging of stars outside the solar system (Monnier et al. [2007]).

2.1.7 Phase

The phase defines properly the fringe location and it is very sensitive to the turbulence of the atmosphere. The available optical/IR interferometers are not able to measure directly the phase. This quantity is crucial for image reconstruction as it carries information about the geometry, i.e. symmetry of the object. Usually an object is denoted asymmetric when the shape is not centrally-symmetric. For example an ellipse is a symmetric shape, but an ellipse plus a off-center spot is not. A binary star with the two objects having the same brightness is symmetric, if the brightness differs it is not. The observations that uses only two apertures is able to preserve only the so-called differential phase (i.e. as an function of λ). Three (or more) aperture telescopes (such as AMBER, Astronomical Multi-BEam combineR; Petrov et al. 2007) provide a quantity

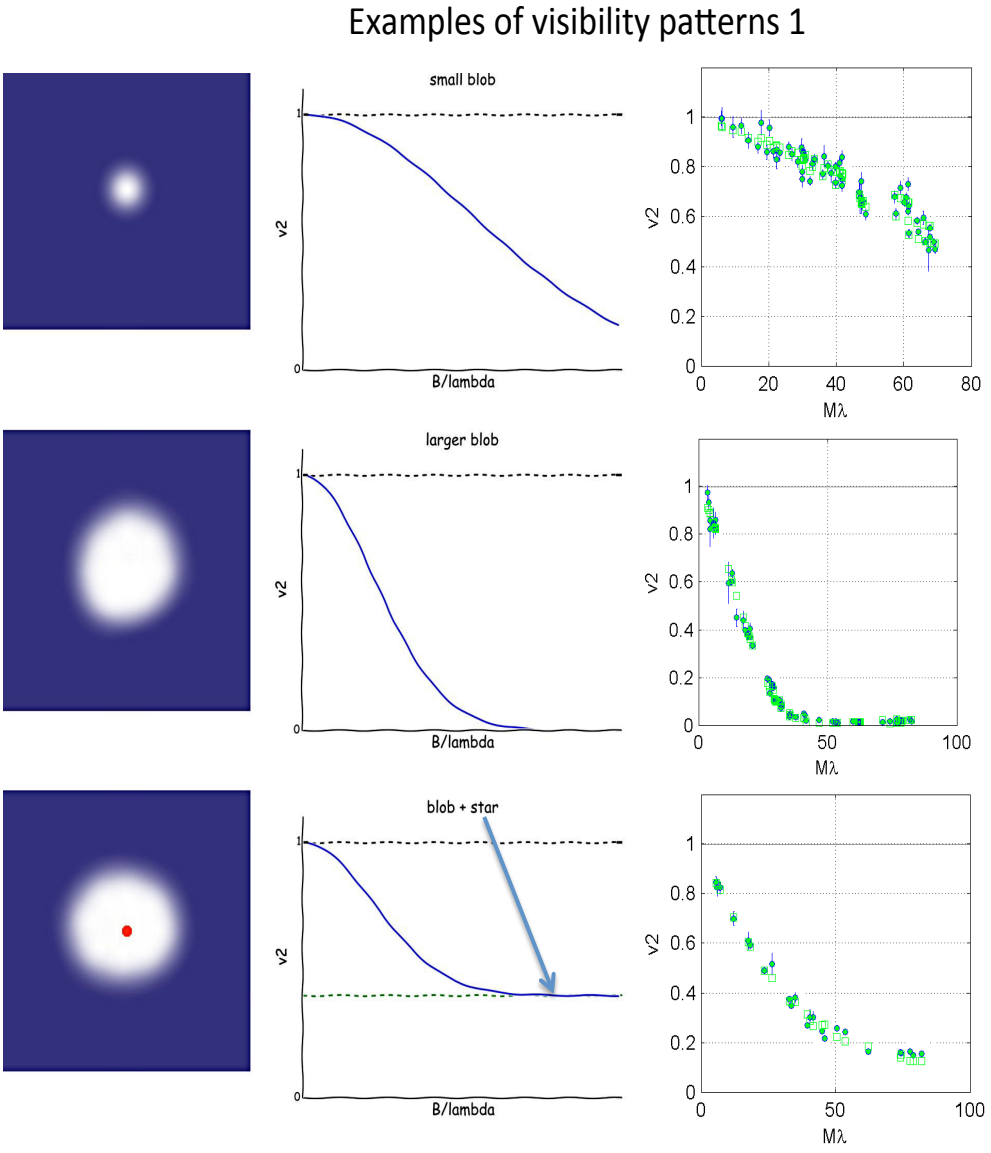

FIGURE 2.17: Illustrative visibility curves for a few Herbig stars (Lazaref et al. 2015 in preparation).

called the closure phase. In following sections, we briefly explain the differential phase and closure phase quantities.

2.1.8 The differential phase

Differential phase is a powerful technique used to measure small phase variations as a function of wavelength, due to sources with chromatic, asymmetric structures.

For marginally resolved objects, the differential phase, $\phi(\lambda)$, in a certain spectral line channel is directly related to the photocenter displacement p of the line-emitting region

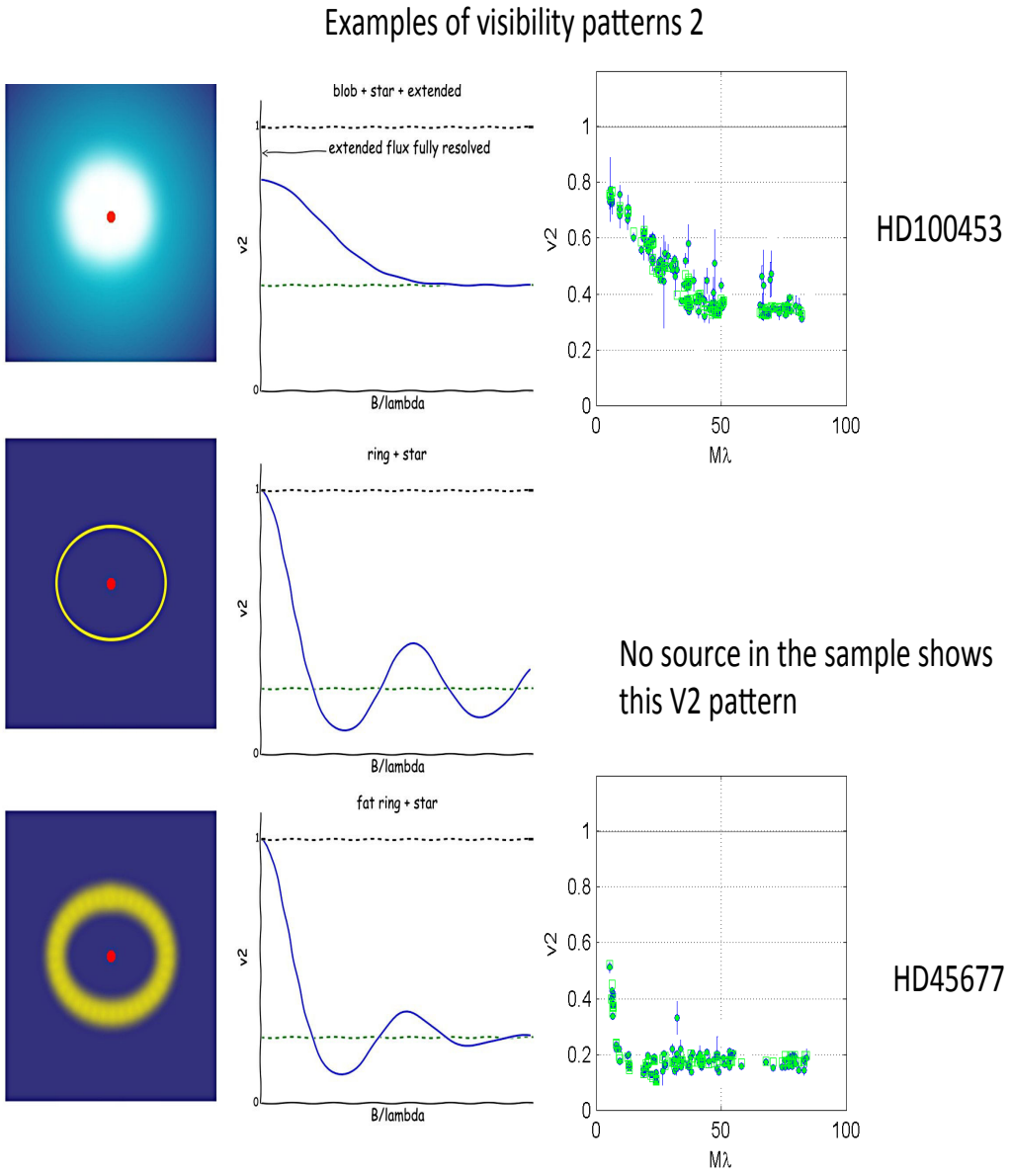

FIGURE 2.18: Same as Fig. 2.18.

with respect to the photocenter of the continuum emission, as projected on the telescope baseline:

$$p = \frac{\lambda}{B}\frac{\phi(\lambda)}{2\pi} \tag{2.58}$$

In Fig. 2.20, we do represent a plot of rotational map of a $Br\gamma$ emission line assuming that the equatorial disk is in rotation (Kraus et al. 2011). In this case, the differential phase is consistent with the expected signature for a Keplerian-rotating circumstellar disk, where the photocenter of the blue and red-shifted line emission is displaced with similar amplitude in opposite directions from the central star. In Fig. 2.19, a cartoon

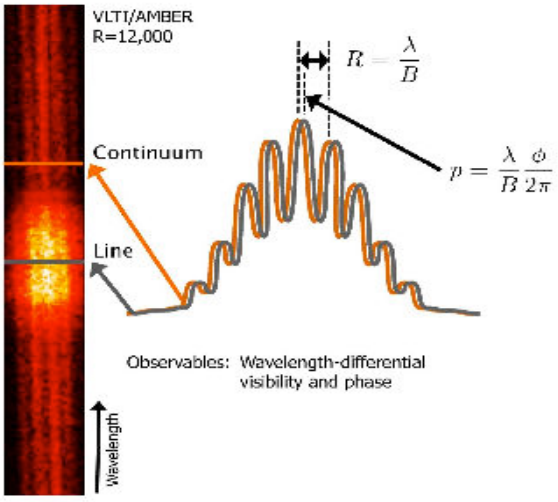

FIGURE 2.19: Spectro-interferometry uses spectrally dispersed interferograms (such as the VLTI/AMBER R = 12, 000 interferogram from Kraus et al. (2011) shown here) in order to detect phase differences between the continuum emission and the emission within a spectral line. In first-order expansion, this differential phase ϕ correspond to the photocenter offset p between the continuum- and line- emitting region. Credit: Kraus et al. (2011)

explaining the effect of photocentric displacement on differential phase is plotted with respect to the fact that the equatorial disk is in rotation.

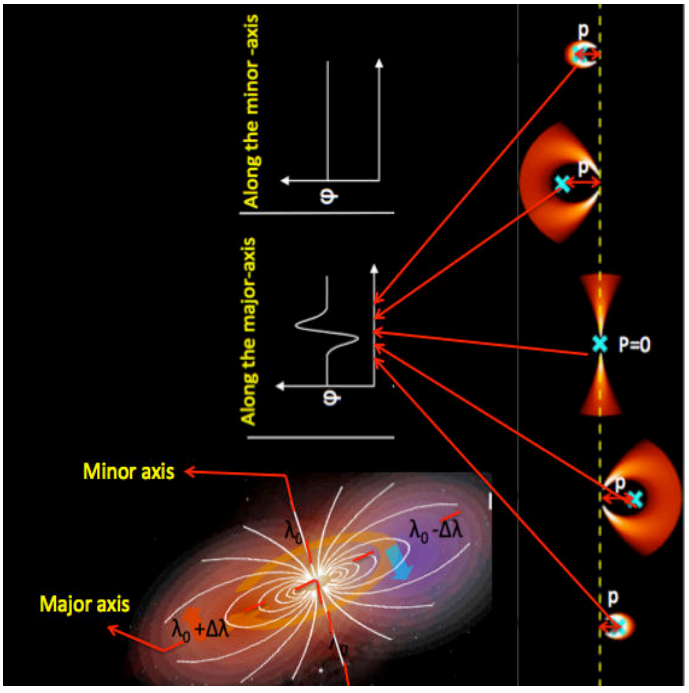

FIGURE 2.20: A cartoon explaining the effect of photocentric displacement on differential phase plot respect to the fact that the equatorial disk is in rotation. Credit: Kraus et al. (2011)

The two operational instruments that offer this observing mode with sufficient resolution

for detailed kinematical studies and measuring the differential phase are the near-infrared VLTI/AMBER instrument (spectral resolution up to $\lambda/\Delta\lambda$ = 12 000, Petrov et al., 2007) and the visual wavelength CHARA/VEGA instrument at the CHARA array (up to $\lambda/\Delta\lambda$ = 35000, Mourard et al., 2012). The differential phase can also be studied at low resolution with the MIDI instrument. In this case, it provides information on the symmetry of the object.

2.1.9 The closure phase

The basic idea of the method of closure phase, introduced by Jennison (1958), is founded on the principle that the sum of the observed phases around a close loop of at least three baselines is equal to the sum of the intrinsic phases due only to the source, which is free from the atmosphere effects. To understand this statement, we show in Fig. 2.21 a configuration of three telescopes where, for each pair (i, j), the observed phase can be expressed by the relation

$$\phi_{ij} = \phi_{0,ij} + \theta_i - \theta_j, \tag{2.59}$$

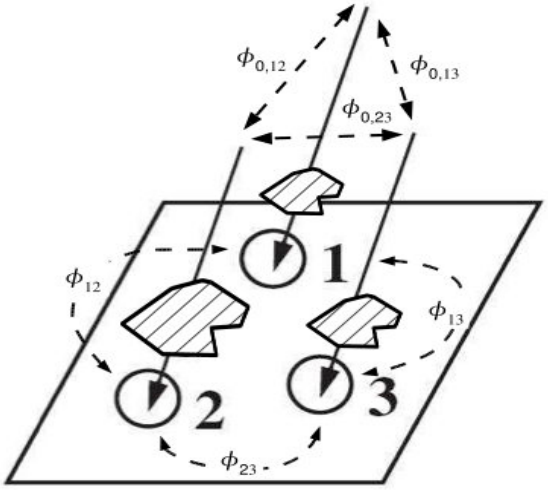

FIGURE 2.21: A cartoon of a configuration of three telescopes. Credit: Monnier et al. 2002.

where $\phi_{0,ij}$ is the intrinsic phase and θ_i, θ_j are the phase shifts introduced by atmospheric variations and/or instrumental errors at each telescope. Defining the closure phase as the sum of the observed phases, β_{123}=ϕ_{12}+ϕ_{23}+ϕ_{31}, Eq. 2.60 implies that the terms θ_i cancel each other out with the result that the closure phase is equal to the sum of the intrinsic phases:

$$\beta_{123} = \phi_{12} + \phi_{23} + \phi_{31} = \phi_{0,12} + \phi_{0,23} + \phi_{0,31} \tag{2.60}$$

To calculate the closure phase, we need to stay in the complex plane to avoid phase wrapping. We compute what is called the Bispectrum, which is an averaged product of all the complex coherent fluxes of triplet telescopes. Computing the phase of complex quantity of the Bispectrum gives us the closure phase value, which is free of atmosphere effects. The Bispectrum is:

$$Bispectrum =< \gamma_{12}\gamma_{13}\gamma_{23} > \tag{2.61}$$

The closure phase is the arctangent of the ratio of the real part to imaginary part of the Bispectrum as following:

$$Closurephase = arctang(\frac{Real(Bispectrum)}{Imaginary(Bispectrum)}) \tag{2.62}$$

The triple product, the Bispectrum, is real if the source is symmetry. This implies that for these types of sources the closure phase is either 0° or 180°. The closure phase measures the amount of asymmetric flux in the target. Therefore one can also write the closure phase as follows:

$$\mid Closurephase(radians) \mid \approx \frac{AsymmetricFlux}{SymmetricFlux} \tag{2.63}$$

The amount of asymmetric flux should be based on the resolution of the baselines (Nothing is asymmetric if the object is unresolved). For instance, for a resolved binary system, the closure phase will be typically roughly the brightness ratio.

Let's give an example. Suppose that we have a star and a spot. At low angular resolution, the stellar disc dominants and the target looks centro-symmetric (See Fig. 2.22-left). In this case, closure phase has small values close to zero.

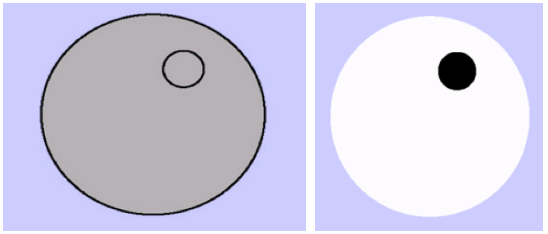

FIGURE 2.22: Left: a star and a spot in low angular resolution. Right: a star and a spot in high angular resolution. Credit: talk of C.A.Haniff in Michelson Summer Workshop.

At high angular resolution, the stellar disc is resolved out, and the off-center spot dominates (See Fig. 2.23-right). In this case, the closure phases have larger values.

Let's give another example. Consider the case of a binary star, in which the size of the stars is the same. In this case, the visibility amplitude is a set of sinusoidal stripes oriented orthogonal to the binary separation as in Fig. 2.24.

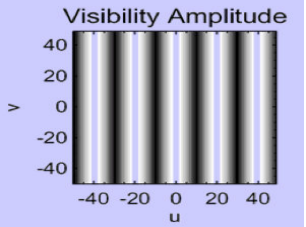

FIGURE 2.23: Visibility amplitude of the fringes. Credit: talk of C.A.Haniff in Michelson Summer Workshop.

In this case, the source is centro-symmetric and the closure phase is either zero or 180 degrees. In Fig. 2.25-top, we plot the visibility of a binary system with a flux ratio of 1 for three pairs of baselines. In Fig 2.25-bottom, we plot the closure phase, whose its value is either 0 or 180 degrees.

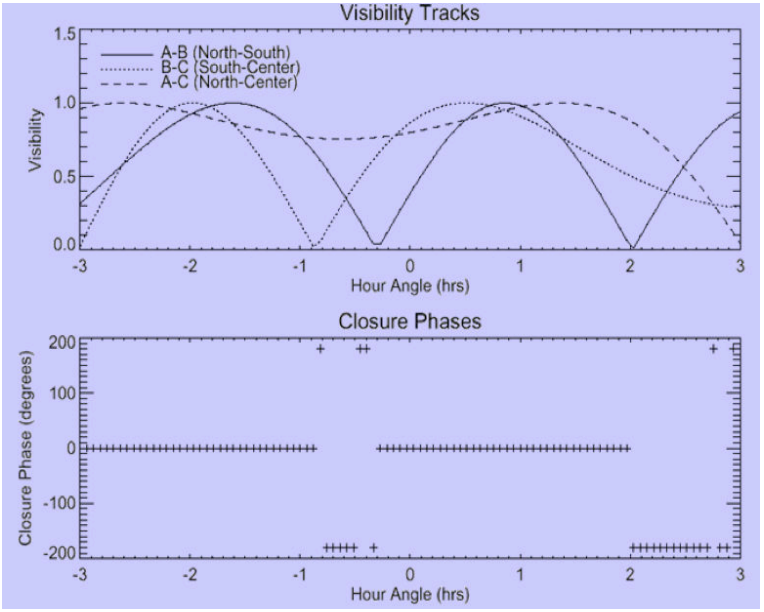

FIGURE 2.24: Top: the visibility curve for a binary system with a flux ratio of 1. Bottom: the closure phase of this binary system. Credit: talk of C.A.Haniff in Michelson Summer Workshop.

Now, we assume a binary stars with a flux ratio of 10. In Fig. 2.26-top, we do show that the visibility of the binary system increases. This means that in this case there is more coherent flux than binary with smaller flux ratio. In Fig. 2.26-bottom, we represent the effect of flux ratio of the binary on closure phase. The closure phase becomes sensitive to the flux ratio and make a departure from 0.

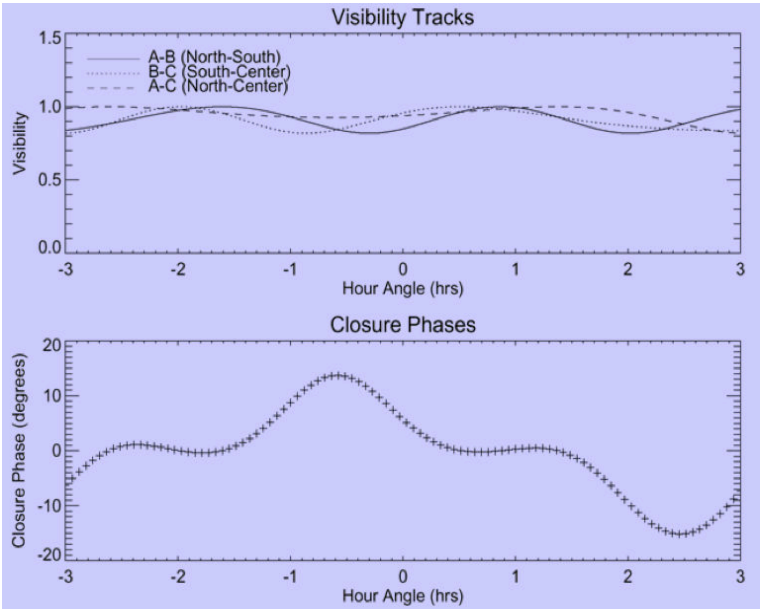

FIGURE 2.25: Top: the visibility curve for a binary system with a flux ratio of 10. Bottom: the closure phase of this binary system. Credit: talk of C.A.Haniff in Michelson Summer Workshop.

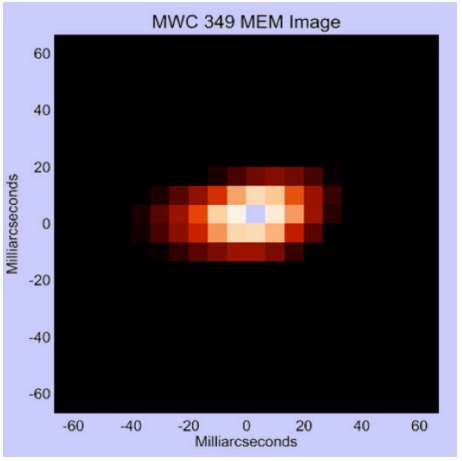

FIGURE 2.26: The image of MWC 349. Credit: talk of C.A.Haniff in Michelson Summer Workshop.

Consequently, the centro-symmetric targets have small or zero closure phases. Closure phases with short baseline triangles have small or zero closure phases since the source is not resolved. In contrast, closure phases with long baseline triangles have larger closure phases especially when the symmetric flux is resolved out. We show two real examples done by Tuthill et al. (2001) and Danchi et al. (2001). The first example is a YSO so called MWC 349. In this case, the object is not resolved. In Fig. 2.27, we show the image of this object and in Fig. 2.28, we represent the visibility and closure phase of this object versus baseline.

The second example is another YSO called LKHα 101. In this case, we better resolve

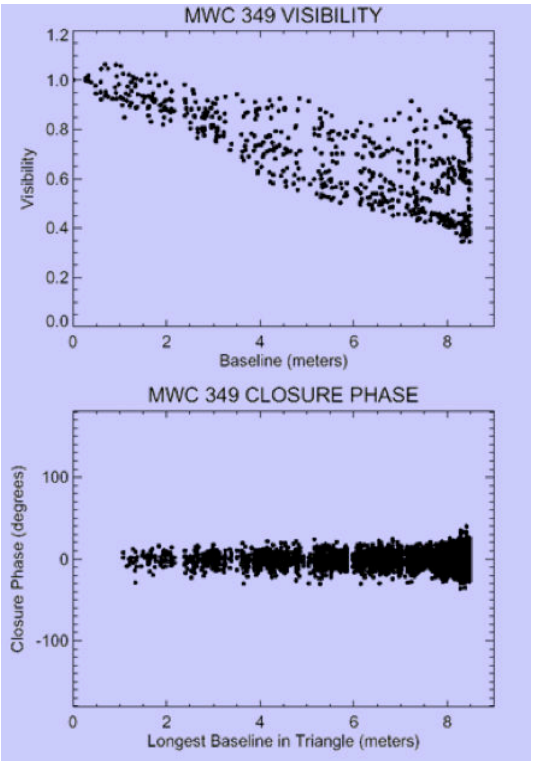

FIGURE 2.27: Top: the visibility versus baseline for MWC 349. Bottom: the closure phase versus baseline. Credit: talk of C.A.Haniff in Michelson Summer Workshop.

the object. In Fig. 2.29, we show the synthetic image of this object and in Fig. 2.30, we show the visibility and closure phase versus baseline.

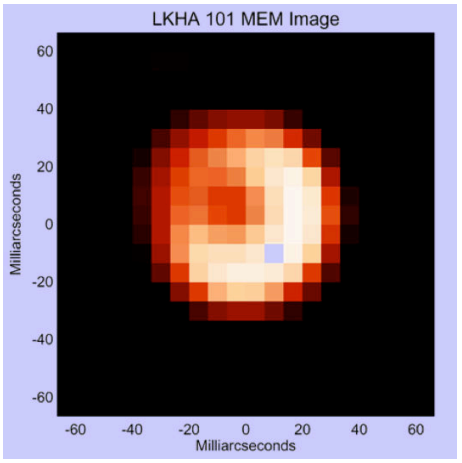

FIGURE 2.28: The image of LKHα 101. Credit: talk of C.A.Haniff in Michelson Summer Workshop.

Resolving the object, the visibility decreases and the departure of the closure phase from zero increases. If non-zero closure phases are seen from a point source, this is indicative of either non-closing baselines or baseline-dependent phase errors. We conclude that for large closure phase signals to be measured, the target being observed must be resolved.

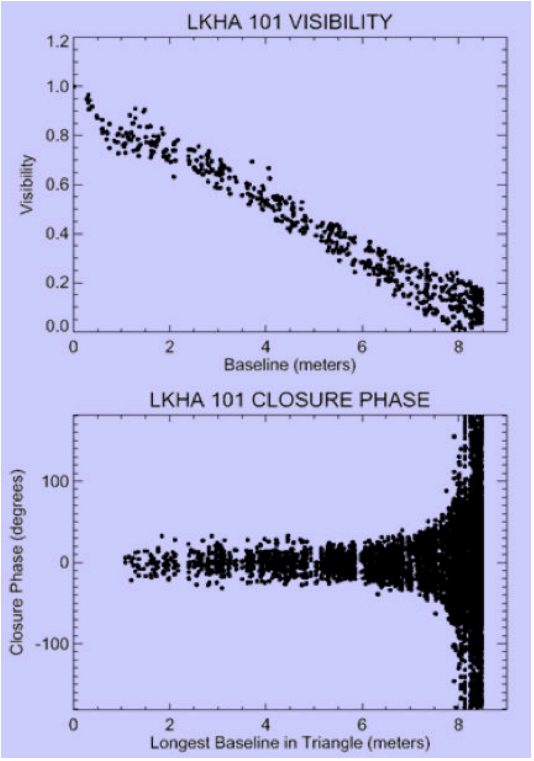

FIGURE 2.29: Top: the visibility versus baseline for LKHα 101. Bottom: the closure phase versus baseline. Credit: talk of C.A.Haniff in Michelson Summer Workshop.

One of the most valuable uses of closure phases in interferometry is to permit model-independent imaging using visibility amplitude and closure phase data.

2.2 Interferometric facilities around the world

The intent of this section is to give a short overview of the instruments available around the world for optical/infrared interferometric observations (Table 2.1). In the following, we focus on the two main interferometers currently offered to the international community: VLTI (Very Large Telescope Interferometer) and CHARA (Center for High Angular Resolution). Since VEGA/CHARA (Visible spEctroGram polAmiter; Mourard et al. 2009), PIONIER (Precision Integrated Optics Near Infrared ExpeRiment; Le Bouquin et al. 2011) and MIDI (MID-infrared Interferometric instrument; Leinert et al. 2003) were used to retrieve the data for this thesis, they will be described in more detail in Sects. 2.2.1, 2.2.2, and 2.2.3, respectively.

VLTI is the ESO interferometer located on Cerro Paranal (Chile). It is equiped with 4 Unit Telescopes (UTs) with 8 m aperture and 4 Auxiliary Telescopes (ATs) with 1.8 m aperture. It allows the combination of 2 up to 4 apertures. The instruments offered to the community are AMBER and MIDI. AMBER (Petrov et al. 2007) is a 3-way beam

TABLE 2.1: List of the instruments offered to the community or to be offered in the future. In col. 1 is reported the acronym of the instrument; in col. 2 the facility where the instrument is mounted; in col. 3 the number of apertures; in col. 4 the baseline range in meter; in col. 5 the wavelength band of observation, and in col. 6 the spectral resolution.

Working time	Instrument	Facility	Apertures	Baselines range	Wavelength	Resolution
Present	PIONIER	VLTI	4	8-130	H-band	30
Future	GRAVITY	VLTI	4	8-130	K-band	22,500,4000
Present	AMBER	VLTI	2-3	8-130	HK-bands	35,1500,12000
Past	MIDI	VLTI	2	8-130	N-band	30,230
Future	MATISSE	VLTI	4	8-130	LMN-bands	30,500,1500-2000
Present	CLASSIC	CHARA	2	30-300	HK-bands	30,10
Present	CLIMB	CHARA	3	30-300	HK-bands	10
Present	VEGA	CHARA	2-3-4	30-300	V-band	6000,30000
Present	MIRC	CHARA	6	30-300	HK-bands	30

combiner observing in the near-IR (H- and K-bands) with different spectral resolutions ($R = \lambda/\Delta\lambda = 35$, 1 500, 12 000). PIONIER and MIDI will be discussed in more details in Sect. 2.2.2 and 2.2.3 respectively.

Two second generation instruments are developed for VLTI: GRAVITY (Eisenhauer et al. 2008), and MATISSE (Multi-AperTure mid-Infrared SpectroScopic Experiment; Lopez et al. 2006). GRAVITY will combine 4 beams in the near-infrared and it will offer imaging and astrometric modes. The spectral resolution will be R = 22 ,500 ,4000. GRAVITY is expected to be started working for 2016. MATISSE will observe in the LMN-bands with 4 telescopes and at low- to mid-spectral resolutions (R = 30, 500, 1500–2000 and also 3000-5000 in L&M bands). MATISSE will be started working for 2017.

CHARA (Center for High Angular Resolution Astronomy) is an array of six 1-meter-telescopes for optical and infrared interferometry on Mount Wilson, California. It offers 15 different baselines with lengths ranging from 30 to 300 m. The instruments operating on CHARA are: CLASSIC, CLIMB, MIRC (Michigan Infrared Beam Combiner; Monnier 2006), FLOUR, PAVO and VEGA (Mourard et al. 2009, Visible spEctroGraph and polArimeter;). The first two instruments observe in H- or K-broad band and combine 2 and 3 apertures, respectively. I will explain in details the VEGA instrument that I used it in my thesis in Sect. 2.2.1.

2.2.1 The VEGA Instrument

VEGA observes in the optical (480-850 nm) with very high spectral resolutions R = 1700 to 30000. It combines 2 to 4 telescopes. The medium (6000) and high (30 000) spectral resolutions are well suited to perform kinematic analysis of the interferometric signal, providing resolution of 60 and 10 km s^{-1} respectively. These spectral resolutions are best dedicated to the extraction of differential spectral information. Radiative winds and fast rotating photospheres of hot stars can be probed efficiently with the medium spectral resolution. Another interesting possibility is the presence of a polarimeter that could be inserted into the beam. This gives new insight into many physical processes.

The low (1700) and medium resolutions are well suited for absolute visibility studies and are also well adapted for the study of binaries or multiple systems.

2.2.2 The PIONIER Instrument

PIONIER (Precision Integrated–Optics Near–infrared Imaging ExpeRiment, Le Bouquin et al. 2011) was commissioned at VLTI in Fall 2010. It is property of the Institute de Planetology et d'Astrophysique de Grenoble (IPAG) and partners. The instrument is optimised for imaging with its 4 way beam combiner working in the H band at low resolution. PIONIER combines either beams from the 8.2-m Unit Telescopes or from the 1.8-m Auxiliary Telescopes to provide visibilities of six different baselines, as well as four closure phase measurements, simultaneously. PIONIER features low resolution spectroscopic optics to measure at six different wavelengths within the H-band, increasing the (u,v) coverage, or can work in broad band light for sensitivity enhancement on faint targets.

2.2.3 The MIDI Instrument

MIDI was mounted on ESO/VLTI at Paranal (Chile). The conceptual design started in 1997. This instrument is the result of the efforts of several European institutions, and it detected the first fringes with the UTs on December 12, 2002. This instrument was decommissioned in the beginning of 2015, since the MATISSE instrument will be started working in 2017. MIDI combines the light coming from two apertures (UTs or ATs) using a two pupil- plane beam splitter. The wavelength range of observation is the N–band (8, 13 μm). Sixteen configurations are offered at the moment with a range in baselines between 11 and 130 m. The observations are dispersed in wavelength and two spectral resolutions are available: PRISM (R = 30), and GRISM (R = 230). The instrument is (as of Sept. 2011) offered in two modes: high-sensitivity (HIGH SENS),

science and photometry (SCI PHOT). In HIGH SENS mode the photometry is recorded a few minutes after (or before) the fringes. This allows to observe fainter objects but is less accurate. In SCI PHOT mode the photometric channels are recorded simultaneously during the scanning of the fringes. The gain in accuracy in this mode is possible only for targets brighter than 200 Jy.

Chapter 3

The peculiar fast-rotating star 51 Oph probed by VEGA/CHARA

3.1 Abstract

Stellar rotation is a key in our understanding of both mass-loss and evolution of intermediate and massive stars. It can lead to anisotropic mass-loss in the form of radiative wind or an excretion disk. I wished to spatially resolve the photosphere and gaseous environment of 51 Oph, a peculiar star with a very high, v sin i=267±5 km.s^{-1}(Dunkin et al., 1997a) and an evolutionary status that remains unsettled. It has been classified by different authors as a Herbig, a β Pic like, or a classical Be star. I used the VEGA visible beam combiner installed on the CHARA array that reaches a submilliarcsecond resolution. Observations were centered on the Hα emission line and in the neighbouring continuum. Data have been reduced by Dr. Philippe Berio. I used the line modeling of Stee et al. (1996). I succeed to derived, for the first time, the extension and flattening of the 51 Oph's photosphere. I found a major axis of θ_{eq}=8.08±0.70 $R_\odot$ and a minor axis of θ_{pol}=5.66±0.23 $R_\odot$. This high photosphere distortion shows that the star is rotating close to its critical velocity. Finally, using spectro-interferometric measurements in the Hα line, I constrained the circumstellar environment geometry and kinematics and showed that the emission is produced in a 5.6 ± 2 $R_\star$ disk in Keplerian rotation. I conclude that from the visible point of view, 51 Oph presents all the features of a classical Be star: near critical-rotation and double-peaked Hα line in emission produced in a gaseous disk in Keplerian rotation. However, this does not explain the presence of dust as seen in the mid-infrared and millimeter spectra, and the evolutionary status of 51 Oph remains unsettled.

3.2 Introduction

The environment of young stars is formed by a dusty and gaseous circumstellar disk in which the first stages of planet formation are thought to take place. Hence, building a comprehensive picture of the physical mechanisms governing this formation requires the understanding of the distribution and the evolution of both the dust and gas species. The content and dynamics of the gaseous component, which dominates the total mass of the disk, control the accretion-ejection processes and will define the final architecture of forming planetary systems.

Many hot stars are observed to be rotating with equatorial velocities higher than 120 km s^{-1} (Abt and Morrell, 1995; Abt et al., 2002). This fast stellar rotation can have strong effects on the observed stellar shape and the intensity distribution (gravity darkening). Some hot stars show emission lines in their spectra. These features indicate a gaseous circumstellar environment surrounding these stars. The study of the stellar photosphere and circumstellar environment of fast-rotating stars is limited by the lack of spatial resolution of single telescopes. An important and reliable way to extract this information is through long- baseline optical interferometry, which allows us to study the detailed stellar surface properties and the close-by environment through emission lines. Several rapid rotators have been studied using these techniques, including Altair, Vega, Achernar, Alderamin, Regulus, and Rasalhague (van Belle et al., 2001; Aufdenberg et al., 2006; Peterson et al., 2006; Domiciano de Souza et al., 2003; Monnier et al., 2007, respectively).

This Chapter is dedicated to the study of 51 Oph: a rapidly rotating star with an age of 0.3 Myr and a mass of ∼4 $M_{\odot}$ (Van den Ancker et al. 1998). This star appears to be a peculiar source in an unusual transitional state. Compared with Herbig Ae/Be stars, van den Ancker et al. (2001) and Meeus et al. (2001) confirmed by analyzing ISO spectra that 51 Oph has more gas than other HAeBe stars. In addition, Malfait et al. (1998) and Leinert et al. (2004) found that the dusty disk of 51 Oph is much smaller (<2AU) than the disk of most HAeBe stars.

Compared with β Pic-like stars, 51 Oph does not exhibit a far-infrared-excess bump, which is inconsistent with the presence of an outer dusty disk (Malfait et al., 1998a). Thi et al. (2013) suggested a difference between 51 Oph and β Pic because the 51 Oph dust grains can be primordial, while the dust grains in an exozodiacal ring around β Pic have to be replenished. Furthermore, 51 Oph does exhibit an H_{α} line in emission, which is not the case of β Pic stars. Berthoud (2008) and Tatulli et al. (2008) concluded that 51 Oph is most likely a classical Be star surrounded by a compact gaseous disk. This scenario agrees well with the following properties reported in previous studies: high rotational

TABLE 3.1: CHARA/VEGA observing log of 51 Oph. For the continuum observations, the calibrators HD 150366 with the uniform disk angular diameter θ_{UD}=0.28 ± 0.02 mas and θ_{UD}=0.39 ± 0.03 mas for HD 163955 were used. For the observations in the H_α line, HD 170296 with θ_{UD}=0.43 ± 0.03 mas was used. The predicted uniform disk angular diameter (in mas) in R band were derived from the JMMC SearchCal software (Bonneau et al., 2006).

Continuum		**H_α line**	
Obs. time (UTC)	Telescopes conf.	Obs. time (UTC)	Telescopes (conf.)
2014-07-04 05:40	E2-S2-W2	———	——
2014-07-04 06:15	E2-S2-W2	2013-05-25 07:12	E1-E2
2014-07-04 06:49	E2-S2-W2	2013-07-28 03:39	S1-S2 (1)
2014-07-08 05:53	E2-S2-W2	2013-07-28 05:43	S1-S2 (2)
2014-07-08 06:18	E2-S2-W2	2014-05-02 10:04	W1-W2 (1)
2014-07-08 06:43	E2-S2-W2	2014-05-02 10:47	W1-W2 (2)

velocity, most of the near-infrared continuum emission arising from the gaseous disk, and hot CO gas in a rotating Keplerian disk. However, the remaining presence of dust around 51 Oph is not supported by this scenario and suggests that this star follows an intriguing evolution scheme.

I here report new elements that lend credit to the hypothesis that 51 Oph is a Be star. Hereafter, I present observations of 51 Oph with a spectro-interferometer operating at visible wavelengths, the VEGA instrument (Mourard et al., 2009, 2011) installed at the CHARA Array (ten Brummelaar et al., 2005). This unique combination of spectrally and spatially resolved information allowed us to resolve the photosphere of the star and to probe the kinematics of the gaseous component producing the Hα line on sub-AU scales.

3.3 Observations and data processing

I collected data at the CHARA Array with the VEGA spectrometer recording spectrally dispersed fringes at visible wavelengths. Observations were performed around the Hα line, between 630 and 670 nm, using the VEGA medium spectral resolution (MR)(R=5000) to study the gaseous disk by combining three pairs of telescopes: W1W2, E1E2, and S1S2. The observation log is given in Table 5.1. The source 51 Oph was also observed in the continuum at 700 nm at MR using the triplet E2S2W2 to study its photosphere. The (u,v) plane coverage corresponding to these data is presented in the left panel of Fig. 3.1 in continuum and in the right panel in the Hα line.

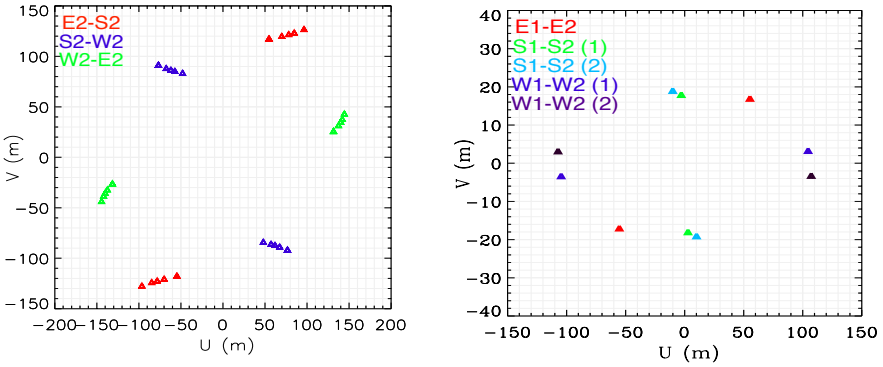

FIGURE 3.1: (u,v) coverage obtained for the observations of 51 Oph in the continuum (left) and the in the Hα line (right).

Data were reduced by Dr. Philippe Berio. The data processing of VEGA is composed of two parts. The data in the continuum are processed using the power spectral method giving the squared visibilities (see Mourard et al., 2009, for details). For this analysis, he used a spectral bandwidth of 15 nm. The processing of the data in the spectral line is based on the cross-spectrum method, which provides differential visibilities and phases across the line. This method was applied with a spectral bandwidth of 0.2 nm.

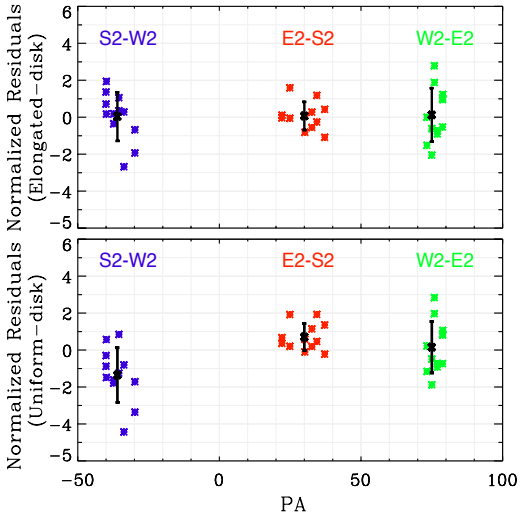

FIGURE 3.2: The normalized residuals between the continuum data and an elongated disk model (top) and a uniform disk model (bottom) are represented for three pairs of telescopes. The black points represent the residual average for each baseline.

3.4 Continuum emission: stellar photosphere

Stellar photosphere was modelled by Dr. Philippe Berio. He used the LITpro2 model-fitting software for optical-to-infrared interferometric data developed by the Jean-Marie

Mariotti Center (JMMC) to interpret our data. Fig. 3.2 shows that the elongated disk model is more consistent with the data than the uniform disk model for the stellar photosphere for the baselines S2-W2 and E2-S2: the mean of the residuals of S2-W2 and E2-S2 is not equal to zero for the uniform disk model. However, both models have nearly the same normalized residuals for the baseline W2-E2. Fig. 3.3 shows the squared visibility versus spatial frequency for an elongated disk model. According to Table 3.2, we found the major axis, $\theta_{\rm eq}$, the minor axis, $\theta_{\rm pol}$, the elongated ratio, $\theta_{\rm eq}/\theta_{\rm pol}$, and the major axis orientation, PA, using an elliptical model. Using Hipparcos 2007 data (van Leeuwen, 2007) and calculating the distance from the parallax (d=124 ±4 pc), we derived an equatorial radius $R_{\rm eq} = 8.08 \pm 0.7\ R_{\odot}$ and a polar radius $R_{\rm pol} = 5.66 \pm 0.23\ R_{\odot}$ from $\theta_{\rm eq}$ and $\theta_{\rm pol}$, respectively. We assumed the continuum flux to exclusively come from the central star. A comparison of the Hα emission line of 51 Oph with classical Be stars shows that the intensity level of 51 Oph is low (only 1.2 time above the continuum, see Fig. 3.4). The flux ratio between the disk and the central star is therefore lower than in classical Be stars. In classical Be stars, this flux ratio in the continuum is between 5 % and 20 % in the visible. We therefore assumed that the disk contribution in the continuum is negligible. The fit of an elliptical model for the stellar photosphere produces a reduced χ^2 (χ^2_r) of 1.52.

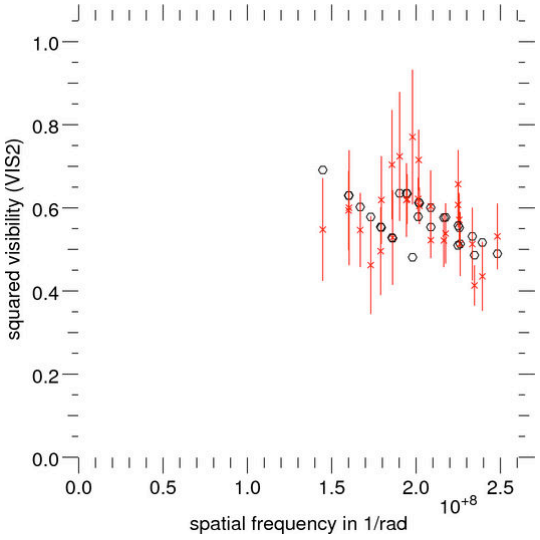

FIGURE 3.3: The squared visibility versus spatial frequency. The red lines are observational data and black circules are related to an elongated disk model for star 51 Oph.

TABLE 3.2: Best-fit parameters obtained from the elliptical model for the stellar photosphere. χ^2_r is the total reduced χ^2

Parameter	Value
Major axis of $\theta_{\rm eq}$	0.6±0.05 mas
Minor axis of $\theta_{\rm pol}$	0.42±0.01 mas
Elongated ratio ($\theta_{\rm eq}/\theta_{\rm pol}$)	1.45 ± 0.12
Position angle (PA)	138 ± 3.9°
χ^2_r	1.52

3.5 Hα emission line

3.5.1 Qualitative analysis

The differential visibility and phase for the five baselines are plotted in Fig. 3.4. The "S" shape of the phase variation clearly favors the hypothesis that the circumstellar environment velocity field is dominated by rotation. Using either differential visibility or phase, we can roughly determine the major-axis position angle in the plane of the sky for a purely rotating disk knowing that:

⋆ The more pronounced the "V" shape of the visibility, the closer the baseline is to the minor axis. The more pronounced "W" shape is related to a position closer to the major-axis.

⋆ For the same projected baseline length, the amplitude of the differential phase variation through the emission line is zero if the baseline is aligned with the minor-axis and maximal if aligned with the major-axis. This is true only if the disk is not fully resolved by the interferometer. For larger baselines, the phase amplitude first saturates and then drops, thus second order effects become visible causing the phase to lose its simple "S" shape.

According to Fig. 3.4, the visibility exhibits a drop in the emission line that is caused by a variation of the circumstellar environment extension and relative flux between the continuum and the line. The phase shows S-shaped variations in the line. This is characteristic of a rotating equatorial disk, as described in Meilland et al. (2012). For the longest baseline, W1W2 the disk is probably over-resolved, so that the differential phase deviates from the S shape, as explained in (Meilland et al., 2012). The VEGA spectrum of 51 Oph obtained during my observations exhibits an Hα emission line with a double-peak similar to the spectrum found by Dunkin et al. (1997b), which reflects the presence of the circumstellar disk. The Hα profile wings wth a sharp absorption in the center show that the disk is seen nearly edge-on.

3.5.2 Kinematic model

To model the wavelength dependence of the visibility, the differential phase and the intensity profile of the Hα line emission, I used a simple kinematic model of an expanding and/or rotating thin equatorial disk[1]. This model has been developed by Stee et al. (1997) and previously used for some classical Be stars, for instance, by Meilland et al. (2011) and Meilland et al. (2012) and is described in detail by Delaa et al. (2011).

The star is modeled as a uniform disk, the envelope emission in the continuum and the emission line has an elliptical Gaussian distribution with a flattening due to a projection effect of the geometrically thin equatorial disk, i.e., f = 1/cos(i), where i the the object inclination angle. The radial and azimuthal velocities are given by:

$$V_r = V_0 + (V_\infty - V_0)\left(1 - \frac{R_\star}{r}\right)^\gamma \tag{3.1}$$

$$V_\phi = V_{rot}\left(\frac{r}{R_\star}\right)^\beta \tag{3.2}$$

For each spectral channel in the line an iso-velocity map projected along the line of sight is then calculated and multiplied by the whole emission map in the line. Finally the whole emission map for each wavelength consists of the weighted sum of the stellar map, the disk continuum map and the emission line map within the spectral channel under consideration. The map is then rotated by the major-axis PA, and scaled using the stellar radius and distance. Finally, visibilities, differential phases, and closure phases are extracted using two-dimensional fast-Fourier transforms (FFT). The free parameters of the model can be classified into 4 categories:

1. The global geometric parameters: stellar radius ($R_\star$), distance (d), inclination angle (i), and disk major-axis position angle (PA).

2. The global kinematic parameters: stellar rotational velocity (V_{rot}), expansion velocity at the photosphere (V_0), terminal velocity (V_∞), exponent of the expansion velocity law (γ), and exponent of the rotational velocity law (β). These parameters describe the global disk kinematics and thus also should not depend on the observed line.

3. The disk continuum parameters: disk radius in the continuum (a_c), disk continuum flux normalized by the total continuum flux (F_c). These parameters depends on the observed wavelength. We neglect the contribution of the disk continuum emission in our

[1] As input of our model, we used a synthetic absorption in H_α line calculated with the TLUSTY code (Hubeny, 1998).

TABLE 3.3: Best-fit parameters obtained from our simple kinematic model of the circumstellar disk.

Parameter	Value	Remarks
Geometric parameters		
$R_{\rm eq}$	$8.08 R_{\odot}$	This work (Sect 5.4)
d	124 pc	(van Leeuwen 2007)
i	80^{+7}_{-30} deg	This work
PA	122^{+15}_{-25} deg	This work
Kinematic parameter		
$V_{\rm rot}$	267 km.s $^{-1}$	(Dunkin et al. 1997a)
H_α line parameters		
a_l	5.6 ± 2 $R_\star$	This work
EW	5.0^{+2}_{-3} $\mathring{A}$	This work
χ^2_r	0.7	

modeling and we assume that all continuum flux come from the central star. The disk emission line parameters: disk radius in the line (a_l) and line equivalent width (EW).

Consequently, I need a model with a total of 15 free parameters. To reduce the number of free parameters assuming no expansion, I have finally decided:

- The star distance was calculated following van Leeuwen (2007),
- The equator stellar radius was derived from the fit of the elliptical model according to Sect. 5.4 (in solar radius),
- We assumed that the disk is directly connected to the stellar surface, therefore the rotational velocity ($V_{\rm rot}$) should be equal to the stellar rotational velocity, and
- We also assumed that the gaseous disk surrounding 51 Oph is Keplerian, so that we set β, the rotation velocity law to -0.5.

The other four parameters, i.e., i, PA, a_l and EW were left free.

For this target I computed several hundreds of models to constrain the free parameters, determined the uncertainties, and tried to detect any degeneracy or linked parameters. To reduce the number of computed models, I started with a qualitative estimation of the parameters from our interferometric data (P.A., i, a_l, and EW) and explored the parameter space with decreasing steps to converge to the χ^2 minimum (χ^2_r). The final parameter values for the best-fit models are presented in Table 3.3. The corresponding differential visibilities and phases are overplotted in Fig 3.4. The final reduced χ^2_r is 0.7.

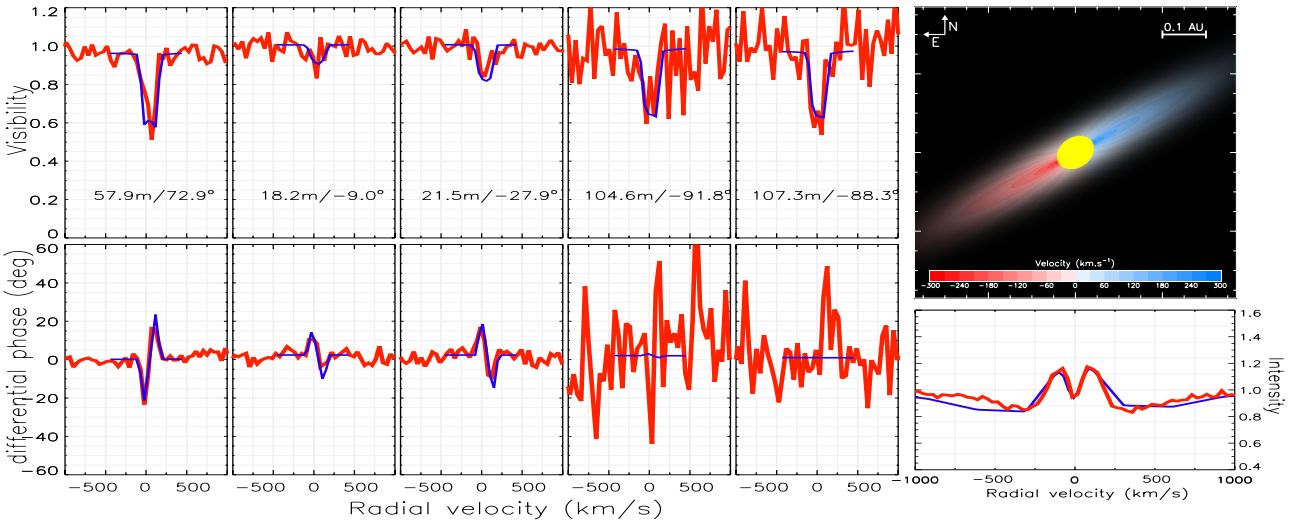

FIGURE 3.4: Visibility and differential phase variations in the Hα emission line and in the surrounding continuum obtained from our medium spectral-resolution (MR) CHARA/VEGA observations (red). The best-fit kinematic model for this dataset is overplotted in blue. The plot (right bottom panel) corresponds to the Hα intensity profile. The top right panel of the figure shows the elliptical model for the central star 51 Oph and our kinematic model for a purely rotating disk.

The inclination angle found for the gaseous disk in our study is compatible with the previous estimate of Thi et al. (2005), that is, $88^{\circ}{}^{+2}_{-35}$ and that of Tatulli et al. (2008), $82^{\circ}{}^{+8}_{-15}$. Moreover, the disk position angle that I derived, that is, $122^{\circ}{}^{+15}_{-25}$, is also compatible with that of Tatulli et al. (2008), $126^{\circ}{}^{+15}_{-5}$, and is likewise consistent with the angle found by Stark et al. (2009), $126^{\circ}{}^{+0.5}_{-0.15}$. Finally, the position angle of the gaseous disk in our study also agrees well with the position angle found for the major axis of the central star, that is, 138± 3.9°, showing that the disk is in the equatorial plane.

3.6 Discussions

The first main result from our CHARA/VEGA observing campaign on 51 Oph is the measurement of the highly flattened stellar photosphere. Assuming that the photosphere distortion is due to the high rotational velocity of the star, the stellar rotational rate can be inferred. Assuming a Roche model and for an edge-on star, a 1.45±0.12 distortion corresponds to an angular rotation rate of Ω/Ω_c=0.99±0.02, or a linear one of V/V_c=0.96±0.1. Another method for deriving the rotational rate is to use the mass and radius of the star and the measured $v \sin i$. The critical velocity is given by $V_c = \sqrt{GM_\star/R_e} = \sqrt{2GM_\star/3R_p}$, where the 'e' and 'p' subscripts correspond to

the equatorial and polar values. Knowing the mass of 51 Oph, $4M_{\odot}$ (van den Ancker et al. 1998) and $R_{\rm eq}$, $8.08R_{\odot}$, the calculated critical velocity is 308 km s $^{-1}$. Neglecting the stellar inclination angle, the rotational velocity of the star, that is, 267 km s $^{-1}$, is 86 % of the critical one in linear velocity. As the star might not be seen fully edge-on, this represents a lower limit of the rotational rate. These two different methods give coherent results, and it is clear that 51 Oph is very close to critical rotation.

Assuming critical rotation for a star with a rotational velocity of $267\,\mathrm{km\,s^{-1}}$ and a polar radius of R_p=5.66±0.23 $\mathrm{R}_{\odot}$, we can deduce a mass of 3.3±0.1 $\mathrm{M}_{\odot}$. This is 25% lower than the estimate of van den Ancker et al. (1998), who assumed pre-main sequence evolutionary tracks, that is, 4 $\mathrm{M}_{\odot}$, and 15% lower than the estimate of van den Ancker (2001), who assumed post-main sequence evolutionary tracks, that is, 3.8 $\mathrm{M}_{\odot}$. Nevertheless, even if our measurement favors the post-main sequence hypothesis, the difference between the two estimated masses is too small to conclude on the evolutionary status of 51 Oph.

The second important result of our study is the direct measurement of the polar radius. Considering the estimate of the effective temperature by Van den Ancker et al. (1998) of 10000 K, it is too high for the star to be classified as a main-sequence star. The standard value for a B9.5V to A0V star is about 2.4-2.6 $\mathrm{R}_{\odot}$. Accordingly, 51 Oph should be classified as a giant star. This distance from the main sequence, which was already found by Ancker et al. (1998), was used to compute the age, assuming that 51 Oph was a pre-main sequence star still in the contraction phase. Nevertheless, as we stated above, this value is also compatible with a post-main sequence star. The last main result from our CHARA/VEGA observing campaign concerns the circumstellar environment geometry and kinematics. We first note that the extension in the Hα line converted to AU, 0.20±0.07AU, is compatible with the one found by Tatulli et al. (2008) in the K-band CO lines using the VLTI/AMBER instrument, $0.15^{+0.07}_{-0.04}$ AU. This emission is also lower than the dust sublimation radius of 51 Oph computed using Eq. 1 from Dullemond and Monnier (2010), 1.17 AU (i.e., with T_{eff}=10000 K, T_{rim}=1500 K and $\mathrm{R}_{\star}$=R_p). This means that the Hα emission and CO emission both are inside of dust sublimation radius. With our kinematic model, we showed that the spectro-interferometric data in the Hα emission line are fully compatible with a geometrically thin disk in Keplerian rotation. The disk features are similar to those of the few classical Be stars studied with the same instrument (Meilland et al. 2011, Delaa et al. 2011), even if the extension in Hα is slightly smaller in the case of 51 Oph. On the other hand, the emission could come from an accretion disk whose geometry and kinematics would not differ strongly from the one of the excretion disk of classical Be stars. The main difference between the two models would be the radial velocity, positive for the excretion disk and negative for the accretion disk. However, this low radial velocity of about 0.1 to $1\,\mathrm{km\,s^{-1}}$ is negligible

compared to the high rotational velocity in the disk and cannot be constrained in our data.

Finally, from the visible point of view, 51 Oph presents all the features of a classical Be star: critical rotation, double-peaked Hα line in emission, and a circumstellar gas disk of a few stellar radii in Keplerian rotation. However, this does not explain the presence of dust as seen in the mid-infrared and millimeter range, and the evolutionary status of 51 Oph still remains unclear. Nevertheless, even if 51 Oph were a pre-main-sequence star, it would make a perfect progenitor for a classical Be star because it is very unlikely that it will lose enough angular momentum to significantly slow down during its on-going contraction phase.

Chapter 4

Probing the inner region of the pre-transitional disk of HD 100546

4.1 Abstract

In this study, we focus our research on the sub-AU disk structure of the Herbig Be star HD 100546 that shows evidence for a gap within the first 12 AU of its pre-transitional disk. We seek a more detailed understanding of the radial and the vertical structure of the inner rim of HD 100546. We obtained a large amount of new interferometric data using the PIONIER/VLTI instrument at H band. The essential part of the emission comes from the hot dust in the innermost circumstellar disk. Combining the observational measurements with photometric observations, we investigate the circumstellar environment of HD 100546 by modelling the disk infrared emission using the 3D Monte-carlo radiative transfer code MCFOST.

Building on previous work (Benisty et al. 2010 (B10); Tatulli et al. 2011 (T11)), we refined a model of the inner astronomical units consisting two disk components separated by a gap. We explored the parameter space in order to constrain the disk structure quantitatively. Our large dataset allowed us to measure an inclination of 48° and a position angle of 119°. We constrain an inner and outer radius of 0.25 AU and 4 AU for the inner disk and an inner radius of 12 AU for the outer disk, which are consistent with T11. The scale height of 6 AU at a radius of 100 AU for the inner disk and the scale height of 12 AU for the outer disk are derived by our analysis. These quantities are consistent with T11 as well.

We successfully reproduced the SED (Spectral Energy Distribution) from the UV to the milimeter range simultaneously with the visibilities in the near-IR (NIR) with our model but not the closure phase.

The detection of non-zero closure phase at long baselines leads us to propose that the inner rim of the disk of HD 100546 might not be smooth. The natural departure from centro-symmetrical disk models ,i.e. inclined disk models or the sharp inner rim edge of the disk can not explain the non-zero closure phase. We tested a hypothesis based on the presence of a clumpy structure in the inner rim, which seems promising but requires further investigations.

4.2 Introduction

HD 100546 is a Herbig Be star, which shows a range of phenomena suggesting it may be the host of a planetary system in the early stage of its formation and evolution. Its age is not well determined, but is likely to be in the range of 3.5–10 Myr. The lower limit comes from Manoj et al. (2006) and the upper one from van den Ancker et al. (1997). The old and new Hipparcos distances are 103^{+7}_{-6} pc (van den Ancker et al. 1997) and 97±4 pc (van Leeuwen 2007). HD 100546 and its environments have been extensively studied over the last 20 years.

The disk around this star has a gap in gas and dust distribution inwards from approximately 10–13 AU. This is confirmed by observational evidence including both SED modeling and direct observations (Bouwman et al. 2003; Benisty et al. 2010; Tatulli et al. 2011; Mulders et al. 2011; Grady et al. 2005a; Acke & van den Ancker 2006; van der Plas et al. 2009). The large outer disk has been imaged using scattered light observations (Pantin et al. 2000; Augereau et al. 2001; Grady et al. 2005b; Ardila et al. 2007; Quillen 2006; Boccaletti et al. 2013; Avenhaus et al. (2014a)), and it exhibits a multiple spiral arm structure.

Independent observations are indicative of the presence of at least two sub-stellar/planetary objects. This makes this system the subject of intense study (see e.g. Bouwman et al. 2003; Acke & van den Ancker 2006; Quanz et al. 2013; Mulders et al. 2013; Brittain et al. 2013, 2014; Walsh et al. 2014).

In particular, there have been several claims that a protoplanet is located in the outer disk, at $\sim$ 50 AU (Quanz et al. 2013; Currie et al. 2014; Quanz et al. 2015; Pinilla et al. 2015), and another candidate in the disk gap at $\sim$ 10 AU (Brittain et al. 2014; Pinilla et al. 2015).

TABLE 4.1: Log of long baseline interferometry observations. Our PIONIER/VLTI observations with ATs (P.I.: Berger 2012) were conduced in December 2012 plus January and February of 2013.

Date	**Baseline**	B_p **[m]**	**P.A.** [°]	**Date**	**Baseline**	B_p **[m]**	**P.A.** [°]
2012–12–20	B2-D0	27	17	2012–12–22	C1-D0	18	9
	A1-B2	10	85		B2-C1	9	6
	C1-D0	18	16		A1-C1	16	42
	A1-C1	16	52		A1-D0	33	23
	B2-C1	9	18		A1-B2	9	71
	A1-D0	32	34		B2-D0	27	8
2013–01–29	A1-K0	127/118	47/86	2013–02–01	J0-K0	42/44	-43/-35
	A1-J3	110/123	64/29		A1-J3	120/117	43/51
	J3-K0	39/45	-55/-25		A1-G1	77/78	-85/-77
2013–01–30	J3-K0	37/44	-61/-33		G1-J3	94/93	3/9
	A1-K0	127/121	41/76		A1-K0	125/122	63/72
	A1-J3	125/115	23/54		G1-K0	71/69	29/-35
2013–02–17	D0-I1	81	-37	2013–02–18	G1-I1	35	70
	H0-I1	34	-5		D0-I1	82	-59
	D0-H0	55	-56		G1-H0	48	26
	G1-H0	44	39		D0-H0	59	-80
	G1-I1	32	-88		D0-G1	65	-35
	D0-G1	66	-16		H0-I1	33	-21
2013–02–19	D0-G1	67/53/58/62	-22/90/-72/-54	2013–02–20	D0-H0	62	76
	G1-H0	45/50/51/51	35/-13/-1/11		D0-I1	81	-84
	H0-I1	34/26/29/32	-10/-70/-55/-39		D0-G1	61	-56
	G1-I1	32/42/41/38	85/19/34/51		G1-H0	51	10
	D0-I1	81/77/80/82	-44/59/78/-81		G1-I1	39	50
	D0-H0	56/64/63/62	-65/40/58/78		H0-I1	32	-41

HD100546 has a $\sim$ 2–45 μm spectrum measured by the Infrared Space Observatory (ISO, Malfait et al. 1998). The spectrum shows similar features as comet Hale-Bopp indicative of a large fraction of crystalline silicates especially forsterite. Mulders et al. (2011) estimate a crystalline mass fraction of 40–60 %, located especially between 13 and 20 AU.

In this Chapter, we present new spectro-interferometric measurements obtained in the H band using the PIONIER instrument installed on VLTI. We build a complete SED from previously published photometric and spectroscopic data. Based on our extensive and unique dataset, we revisit the disk morphology and focus mostly on the inner rim of the inner disk to verify whether or not there is any asymmetry in this region.

4.3 Observations

The observations were performed with the PIONIER 4-telescope beam recombiner instrument (Le Bouquin et al. 2011) using the four 1.8 m Auxiliary Telescopes (AT) of the Very Large Telescope Interferometer (VLTI, Haguenauer et al. 2010) at the Paranal

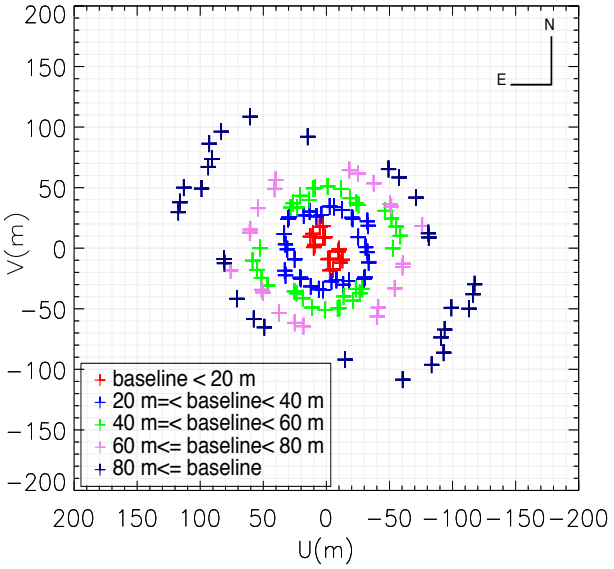

FIGURE 4.1: UV coverage of our PIONIER data.

Observatory of the European Southern Observatory (ESO). In total, 9 nights were allocated to the object with short and long baselines configuration. For the long baseline survey, 3 nights were observed, i.e., two nights in January 2013, two points at each epoch, and, one night in February 2013, two points at each epoch. The remaining nights were fully dedicated for the intermediate and short baselines measurements for single point or number of points at each epoch (See Table 4.1).

The observation strategy consisted in interleaving the science target and observed calibrators. A typical observation sequence (5 blocks) was Calibrator 1 – Science Target – Calibrator 2 – Science Target – Calibrator 1. The calibrators were chosen from the JSDC catalog (Lafrasse et al. 2010) and selected to be unresolved single stars. The calibrators have H-magnitudes that are usually a little brighter than the science targets. Each block, either science or calibrator, was composed of 5 or 10 exposures, each of which composed of 100 fringe scans, followed by the acquisition of the dark frame and the internal, flat-fielded flux splitting ratio (Le Bouquin et al. 2011). Data were reduced and calibrated with the dedicated PNDRS package (Le Bouquin et al. 2011). The fringe measurements were dispersed over three spectral channels across the H band (1.6, 1.656 and 1.765 μm).

A summary of the observations used in this Chapter is given in Table 4.1 and the total UV plane covered by the observations is shown in Fig. 4.1.

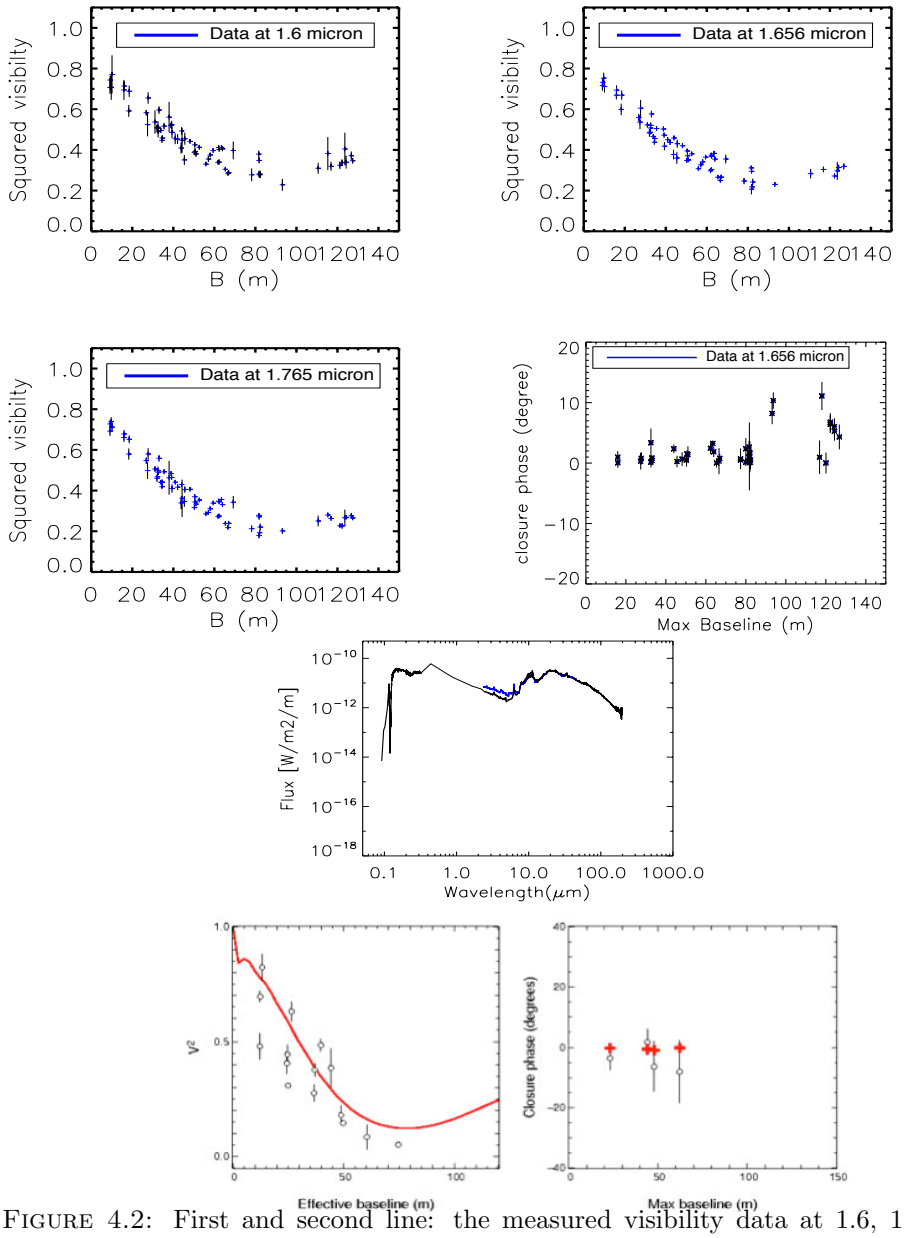

FIGURE 4.2: First and second line: the measured visibility data at 1.6, 1.656 and 1.765 μm. Second line-right: the measured closure phase at 1.656 μm. Third line: Observed spectral energy distribution of HD 100546. Plotted in black are the FUSE, IUE, 2MASS, ISO-PHOT, ISO-LWS for wavelengths 0.1 – 0.2 μm, 0.2 – 0.35 μm, 1.25, 1.65, 2.17 μm, 2.25 – 40 μm, 45 – 190 μm respectively. Over plotted in blue is the ISO-SWS data for wavelengths 2.3 – 12 μm. Fourth line: A plot of visibility and closure phase of AMBER data in H band (circles) and the best models (red solid lines) obtained by Tatulli et al. (2011).

4.4 Data description

4.4.1 Visibilities

In Fig. 4.2, we show the measured visibilities after data processing. They are plotted against baseline, B. Our measured visibilities are plotted for three wavelengths, i.e., 1.6, 1.656 and 1.765 μm.

At baselines shorter than B $\sim$ 10 m, visibilities have a value lower than 1, which can be interpreted as the signature of extended, over-resolved emission. This is evidence for an extended flux. In Fig. 4.2, we show the chromatic dependence of the visibilities. We interpret the chromatic behaviour of the visibilities as a consequence of the varying flux ratio between the star and the inner disk. H band emission is clearly resolved and showed evidence for an asymptotic azimuthal variations which we interpret as the structure of an extended flattened structure in addition to the star.

As we show in Fig. 4.2, compared to T11 data at H band, obtained with AMBER, the number of our data points are larger, data are less scattered with smaller errorbars.

4.4.2 Closure phase

Besides the visibilities that probe the location of the inner rim and its dust properties, we measure the closure phase for HD 100546. The closure phase can be related to the departure from centro-symmetry of the object, in this study the NIR continuum emission. The closure phase values are given in degree. In Fig. 4.2, we plot the measured closure phase versus the maximum baseline. Our closure phase measurements do show a significant departure from zero for maximum baselines greater than $\sim$ 90 m. The closure phase signal at longer baselines is about $10 - 15^{\circ}$ at H band with the average error bars up to $\sim 5^{\circ}$. The precision of our measurements is significantly improved when compared to T11. Note that we have more data points in closure phase than T11 as well.

4.4.3 The spectral energy distribution

We have extracted from the literature photometric measurements from the UV to the far-Infrared wavelengths to produce a complete SED. FUSE is for wavelengths 0.1 – 0.2 μm, IUE for wavelengths 0.2 – 0.35 μm, 2MASS for wavelengths 1.25, 1.65 and 2.17 μm, ISO-PHOT for wavelengths 2.25 – 40 μm and ISO-LWS is for wavelengths 45 – 190 μm (Martin-Zaïdi et al., 2008; Valenti et al., 2003; Cutri et al., 2003; Ábrahám and Kun,

2004; Clegg et al., 1996). We also over plot the ISO-SWS data (Malfait et al., 1998b) in the SED (in blue color) for wavelengths 2.3 – 12 μm (See Fig. 4.2).

4.5 Modeling

In this section, we describe the circumstellar environment of HD 100546 using a disk model proposed first by Bouwman et al. (2003) and later refined by Benisty et al. (2010) and Tatulli et al. (2011). In this model, the disk is composed of two components: inner disk, gap and outer disk (See Fig. 4.3). We add a surface layer to the top layer of the outer disk including small grains to better reproduce the SED as T11.

4.5.1 The radiative transfer code

We used the Monte Carlo 3-D radiative transfer code MCFOST to generate the disk images and the SED (Pinte et al. 2006).

We consider that the disk is comprised of astronomical silicate grains (Draine & Lee 1984) for the inner and outer disk and amorphous olivine (Dorschnet et al. 1995) for the surface layer above the outer disk. The structure of the disk is defined by power laws. Therefore, the surface density and the scale height, i.e, Σ and H, can be expressed by:

$$\Sigma_r = \Sigma_{100AU} \left(\frac{r}{100AU}\right)^p \tag{4.1}$$

$$H_r = H_{100AU} \left(\frac{r}{100AU}\right)^\beta \tag{4.2}$$

Where Σ_{100AU} and H_{100AU} are the values of the surface density and the scale height at a radius of 100 AU, p is the surface density exponent and β is the flaring exponent. The dust grain sizes, a, are distributed following a power law $a^{-3.5}$ (ISM) ranging from minimum and maximum sizes, a_{min} and a_{max} respectively. The total dust mass (M_{dust}) of the disk is fixed and is derived by its inner and outer radius (r_{in} and r_{out}).

We started from the parameters obtained by T11 to which we added the edge of the inner rim. Our aim is to see if our data confirms the model and helps further refinements. This parameter is a prescription to allow for a smooth density transition. The edge is given in AU and defines the scale of density decrease. For edge=0 AU, the inner edge is considered sharp and with an increasing edge, the inner rim gets rounded.

The model parameters can be classified into four categories:

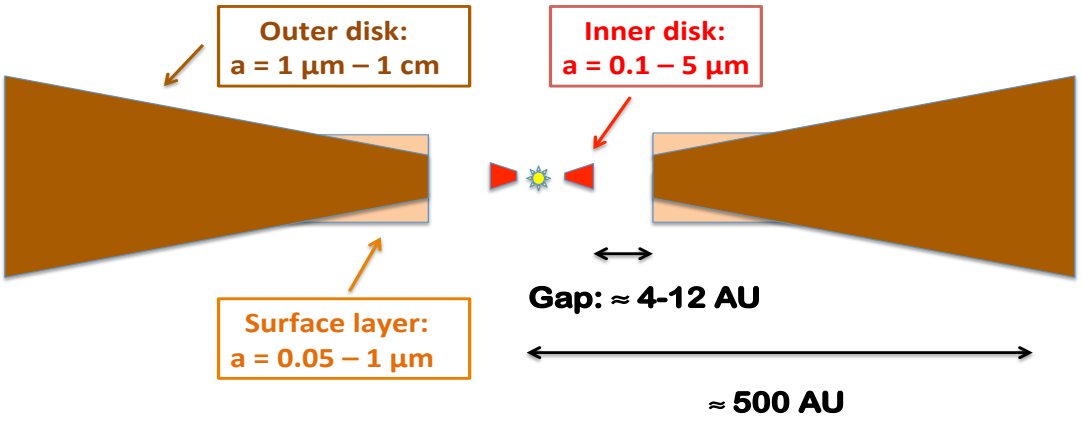

FIGURE 4.3: Schematic view of our best disk model that includes different zones: an inner disk with micron-sized silicate grains, a gap, a massive outer disk with small grains in an upper layer.

1) the stellar parameters;

2) the inner disk parameters: r_{in}, r_{out}, scale height, flaring index, surface density index, edge of inner rim;

3) the surface layer above the outer disk parameters: r_{in}, r_{out}, scale height, flaring index, surface density index;

4) the outer disk parameters: r_{in}, r_{out}, scale height, flaring index, surface density index, edge of inner rim.

4.5.2 Methodology

To model the stellar flux, we consider photospheric models from the Kurucz grid of LTE models (Kurucz 1979; Castelli & Kurucz 2004) providing a temperature of T=10500 K (Van den Ancker et al. 1997), a log g of 4.0. We take a stellar radius of 1.54 $R_{\odot}$, a mass of 2.4 $M_{\odot}$ (Van den Ancker et al. 1997), and a non-zero extinction ($A_v \sim 0.2 - 0.3$) for HD 100546.

To interpret in a consistent approach all our observational measurements, we developed a methodology. Since our data have been obtained using Auxiliary Telescopes (ATs) of VLTI with a field-of-view of $\lambda/D \simeq 240$ mas $\equiv$ 25 AU, where D is the diameter of the telescope, we are probing both the inner part of the disk and the extended scattered light. We compute first the visibilities taking into account the telescope field-of-view for three wavelengths 1.6, 1.656 and 1.765 μm. These visibilities are calculated by Fourier transform of the images, which are generated by the MCFOST code at the specific spatial frequencies sampled by the observations. Then, for each triplet of telescopes and

TABLE 4.2: Best-model parameters. The best values of our model, which differ from T11 are bold and the values in the Parenthesis have the best values found by T11. The rest of parameters in the table are the same values as in T11.

Parameters	Units	Inner disk	Surface layer	outer disk
i	[degree]	$\mathbf{48 \pm 6}$ (33 ± 11)	...	...
P.A.	[degree]	$\mathbf{119 \pm 14}$ (140 ± 16)	...	...
M_{dust}	$[M_\odot]$	$\mathbf{0.5^{+0.01}_{-0.03}}$ $\times 10^{-10}$ (1.75×10^{-10})	$\mathbf{2 \pm 0.6}$ $\times 10^{-7}$ (3×10^{-7})	4.3×10^{-4}
r_{in}	[AU]	$\mathbf{0.25^{+0.02}_{-0.01}}$ (0.24 ± 0.02)	$\mathbf{12^{+2}_{-1}}(13)$	$\mathbf{12^{+2}_{-1}}(13)$
r_{out}	[AU]	4	50	500
H_{100}	[AU]	6	12	12
β		1	0.5	1.125
p		-1	-1	-1
a_{min}	[μm]	0.1	0.05	1
a_{max}	[μm]	5	1	10 000

using the obtained complex visibilities for each baseline, we compute the closure phase calculating the bispectrum (see Eq. 2.62, Chapter 2).

We computed several hundreds of models to constrain the parameters, i.e. i, P.A., r_{in} and r_{out} of the inner disk, r_{in} of the outer disk and the scale height of the inner and the outer disk. Owing to the large number of free-parameters, an automatic model-fitting method would have resulted in the computation of millions of models, which was not within our possibilities. Therefore, we explored the parameters starting from an existing solution based on a defined model reference and tried to narrow down the parameters estimations. The best modeled parameter values are presented in Table 4.2.

In Fig. 4.4, we plot the χ^2 for each parameter fixing other parameters. This figure is plotted only to show our quantitative evaluation of each parameter.

4.5.3 Evaluation of sensitivity to parameters

To check the consistency of our modeling, we tried to determine the effects of all model parameters on the visibility and the closure phase. Our simple approach was to vary each parameter around the reference model values. Some of the parameters strongly affect the visibilities and are consequently easily and unambiguously constrained with only a few measurements with our data:

The mass of the inner disk has the most significant effect on the visibilities. In Fig. 4.5, we represent the effect of the inner disk mass on the visibility and the closure phase.

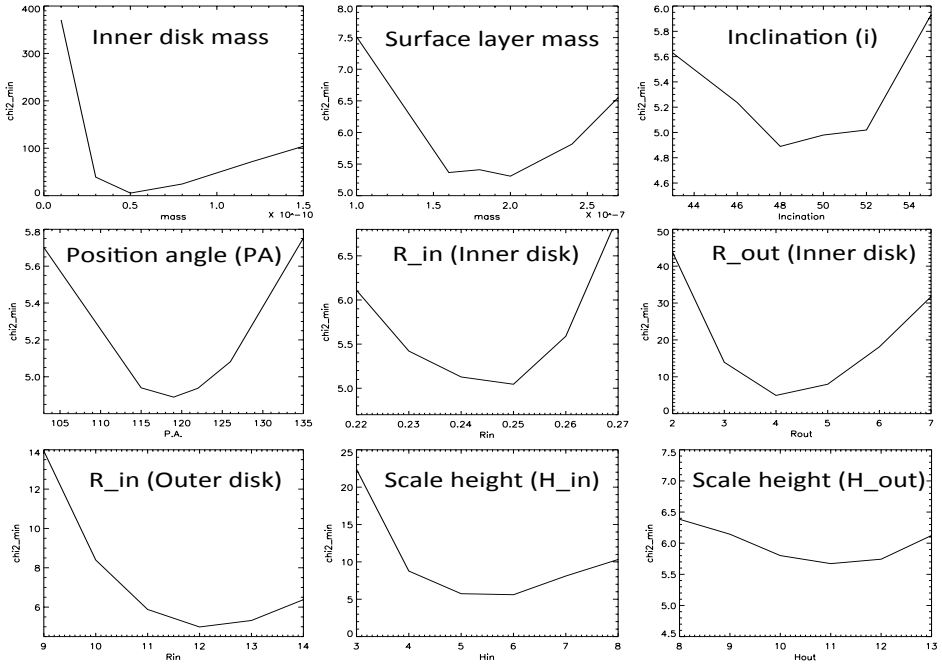

FIGURE 4.4: Plots of χ^2 versus each parameter. χ^2 minimizes for each parameter assuming that other parameters are fixed.

Increasing the mass of inner disk, the visibility values decrease mostly for intermediate and long baselines because of increasing incoherent flux in this region. Increasing the mass also causes the closure phase to slightly increase for baselines greater than $\sim 115m$.

The mass of the surface layer above the outer disk affects the visibilities for all baselines. As we show in Fig. 4.6, increasing the mass causes the visibility to decrease because of increasing more uicoherent flux in the surface of outer disk . The mass of the surface layer has no effect on closure phase.

The inclination angle (i) has a strong influence on the visibility at all baselines. In Fig. 4.7, we plot the visibilities and the closure phases for a limited range of inclinations to demonstrate how varying the inclination influences our interferometric observables. As we show in Fig. 4.7, increasing the inclination causes the visibility for all baselines to decrease. Increasing the inclination causes more coherent flux because of scattering in the inner disk, so that the visibility decreases. For the shorter baselines, increasing the inclination causes more extended emission from the inner edge of the outer disk, so that the visibility decreases. The closure phase does not seem to be dependent on the inclination.

The major-axis position angle (PA) also has a significant effect on visibilities. Increasing the PA, the visibility decreases for intermediate and long baselines (See Fig. 4.8).

The inner radius r_{in} of the inner disk affects the visibility mostly for long baselines. Increasing this value causes an increase in the visibility. This fact could be due to decreasing the correlated flux of the inner disk (See Fig. 4.9). This parameter has no effect on the closure phase,

The outer radius r_{out} of the inner disk has a significant effect on the visibility at intermediate and longer baselines. Increasing this value causes higher values for visibilities. There is no effect on the closure phase (See Fig. 4.10).

The visibility decreases when increasing the scale height of the inner disk at 100 AU, H_{100}. Increasing H_{100} causes the visibility to decrease down to ~ 0.25 for intermediate baselines because the inner disk contributes more to the correlated flux (See Fig. 4.11). Varying the scale height does not have an effect on the closure phase at the current angular resolution.

The inner radius, r_{in}, of the outer disk significantly affects the visibility plot especially for the shorter baselines. The outer disk emission contributes in our visibility as extended emission. Therefore, the visibility is sensitive to the location of the inner radius of the outer disk. Increasing the inner radius at constant scale height causes less extended emission, so that the visibility values at short baselines increases (See Fig. 4.12). The closure phase does not change with inner radius of the outer disk.

The scale height of the outer disk at 100 AU, H_{100}, has a significant effect in the short baselines and a minor effect on the long baselines of visibility. Increasing the scale height leads to more light being intercepted, so that the visibility decreases (See Fig. 4.13). The closure phase does not change with this parameter.

To test the effect of the edge of the inner disk in the closure phase, we explore the influence of the edge for 3 different values of the edge. According to Fig. 4.14, increasing the edge does not seem to affect the closure phase. Increasing the value of the edge causes the edge of the inner rim to become more rounded. In Fig. 4.14, we show the plot of closure phase for the inner disk and for three different values of the edge of the inner rim. We also plot the image of the inner disk for these three values.

4.5.4 Results

While our semi-quantitative approach leads us to define a model that fits the visibility and the SED, we were not able to reproduce the closure phase data. Comparing the model predictions with the plot of visibilities for three wavelengths at H band and the SED, the models agree well with the entire set of data for all baselines and for all wavelengths respectively (See Fig. 4.15).

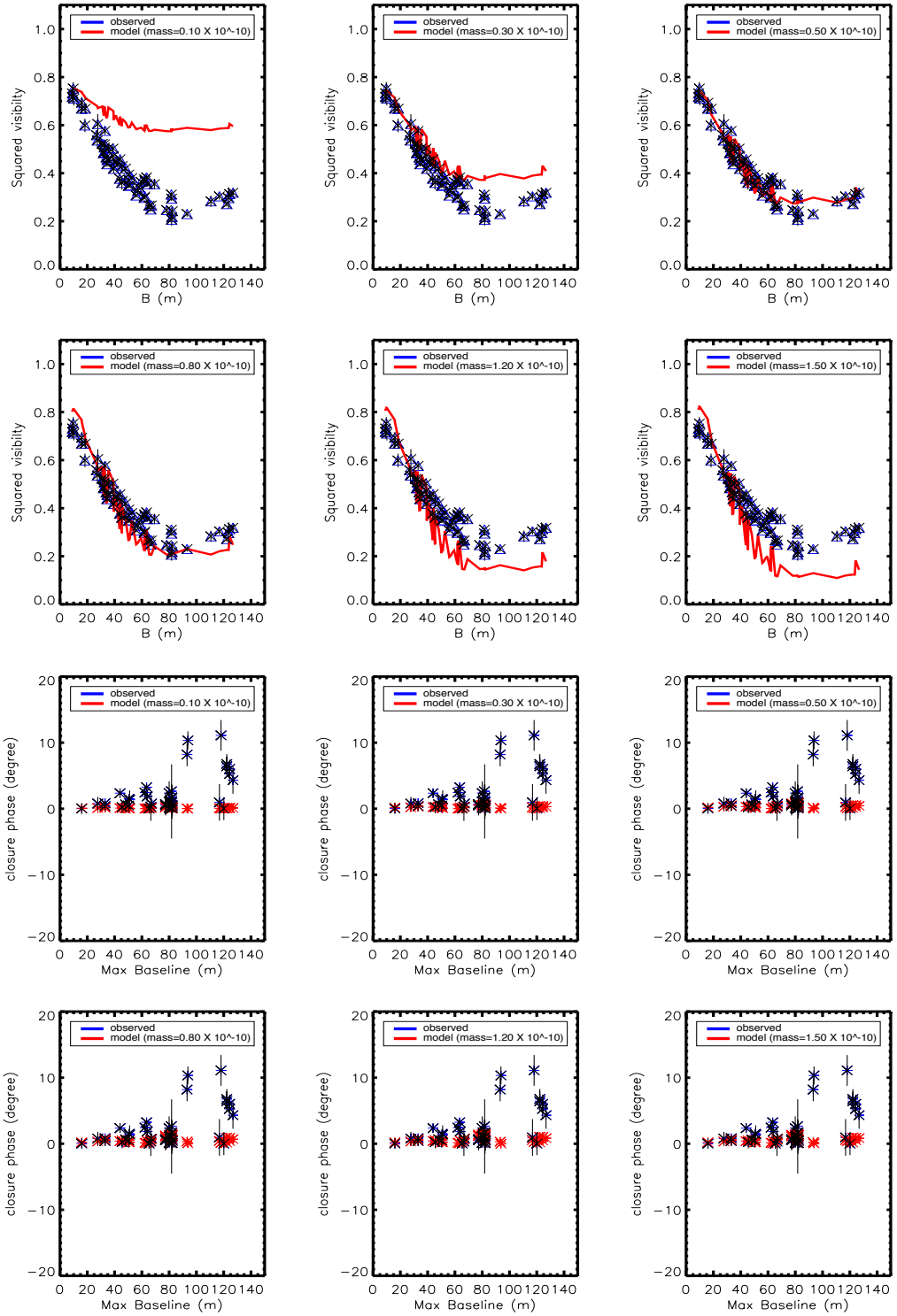

FIGURE 4.5: Top: Visibilities versus baseline for different masses of the inner disk and bottom: Closure phase versus Maximum baseline for different masses of the inner disk at λ=1.656 μm.

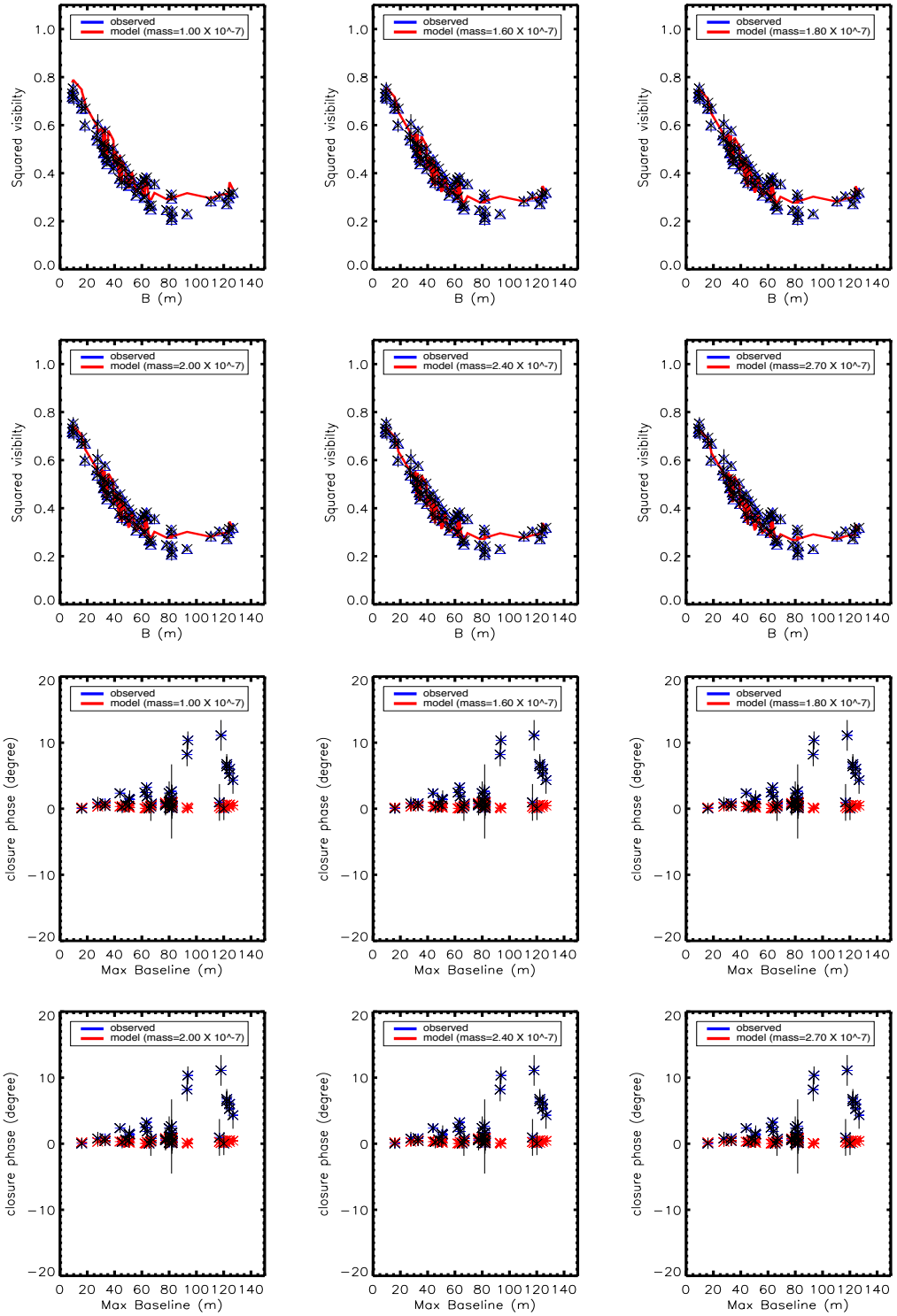

FIGURE 4.6: Top: Visibilities versus baseline for different masses of the surface layer above the outer disk and bottom: Closure phase versus Maximum baseline for different masses of the surface layer above the outer disk at λ=1.656 μm.

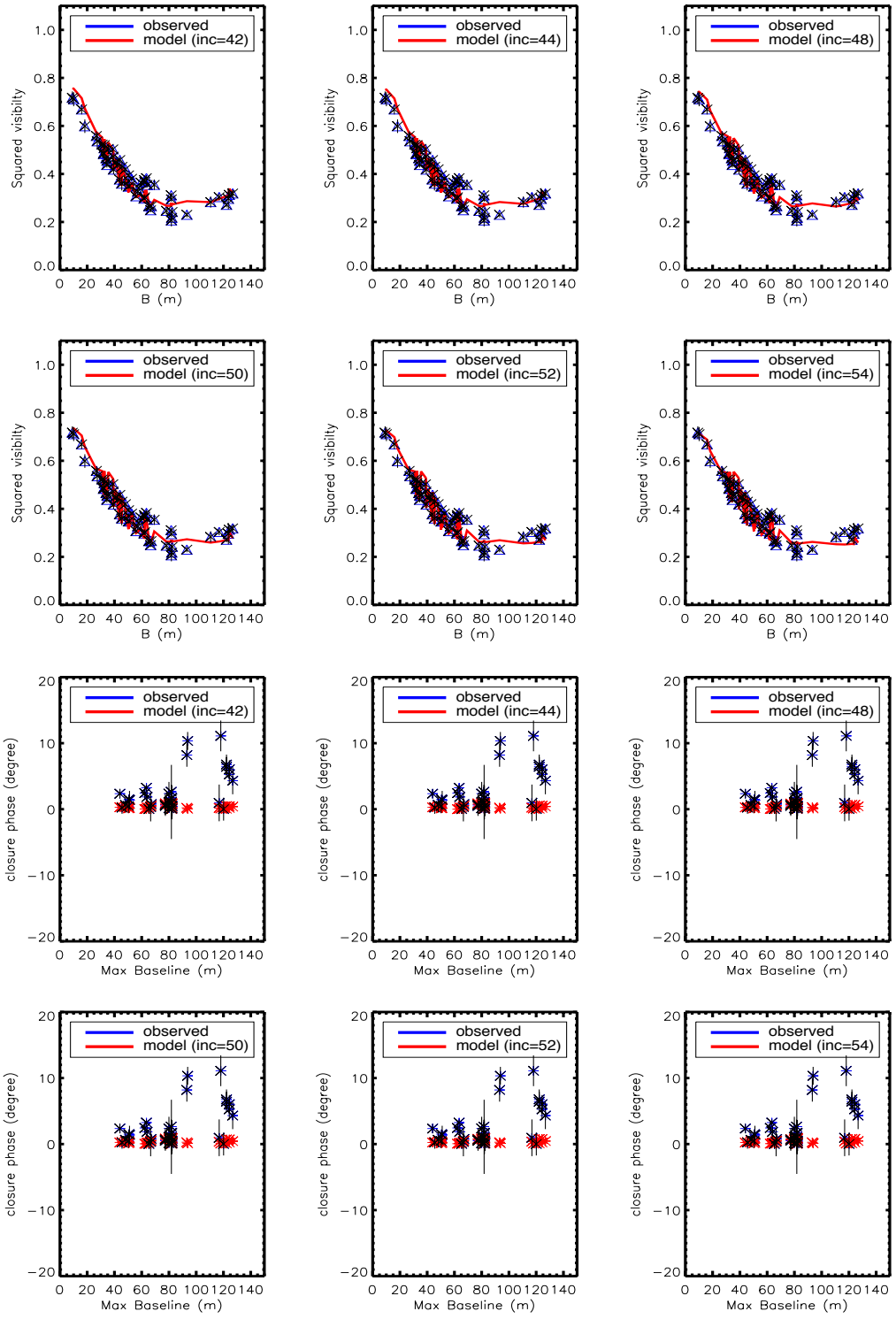

FIGURE 4.7: Top: Visibilities versus baseline for different disk inclinations and bottom: Closure phase versus Maximum baseline for different disk inclinations at λ=1.656 μm.

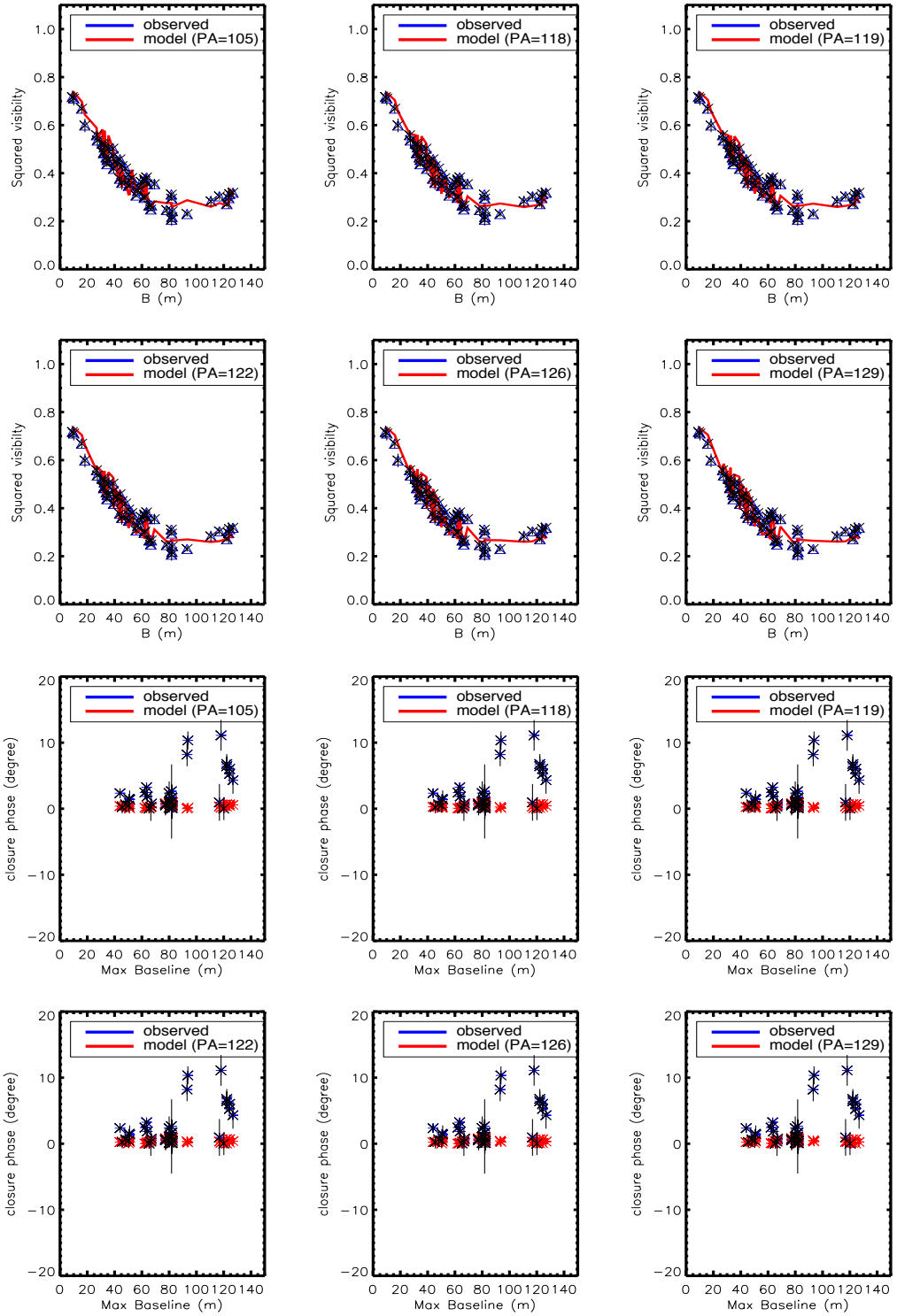

FIGURE 4.8: Top: Visibilities versus baseline for different disk position angles and bottom: Closure phase versus Maximum baseline for different disk position angles at λ=1.656 μm.

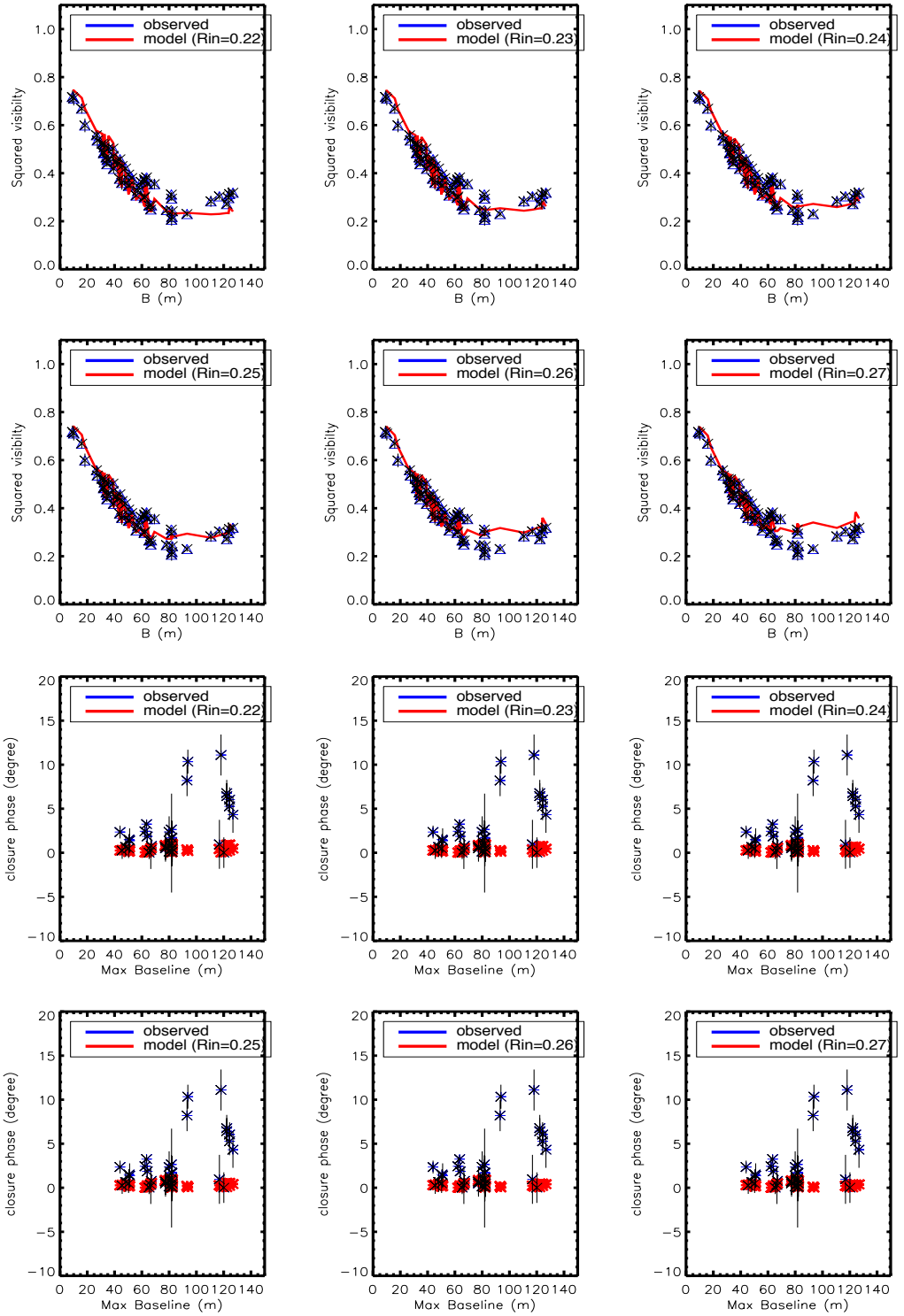

FIGURE 4.9: Top: Visibilities versus baseline for different inner radii of the inner disk and bottom: Closure phase versus Maximum baseline for different inner radii of the inner disk at λ=1.656 μm.

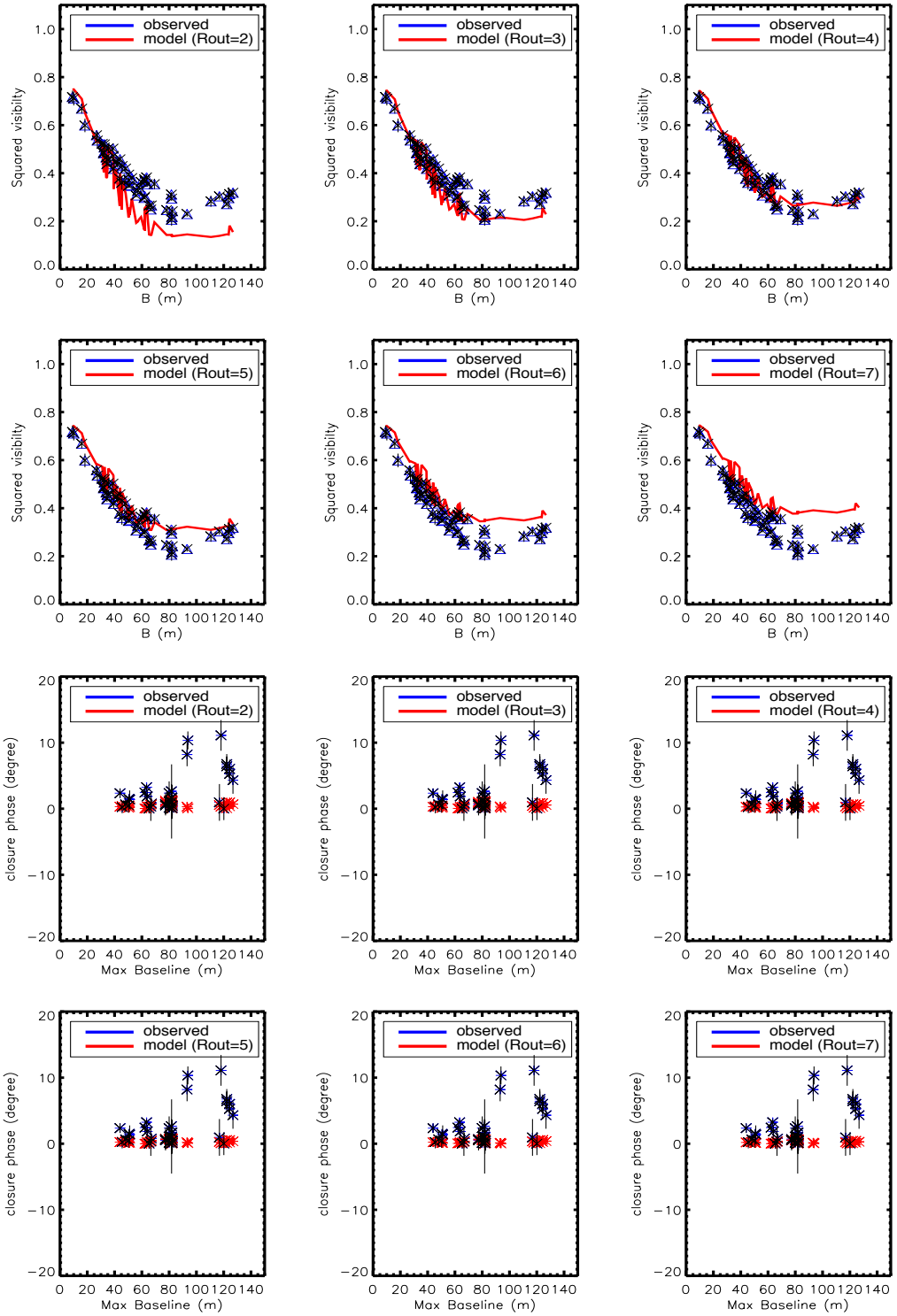

FIGURE 4.10: Top: Visibilities versus baseline for different outer radii of the inner disk and bottom: Closure phase versus Maximum baseline for different outer radii of the inner disk at λ=1.656 μm.

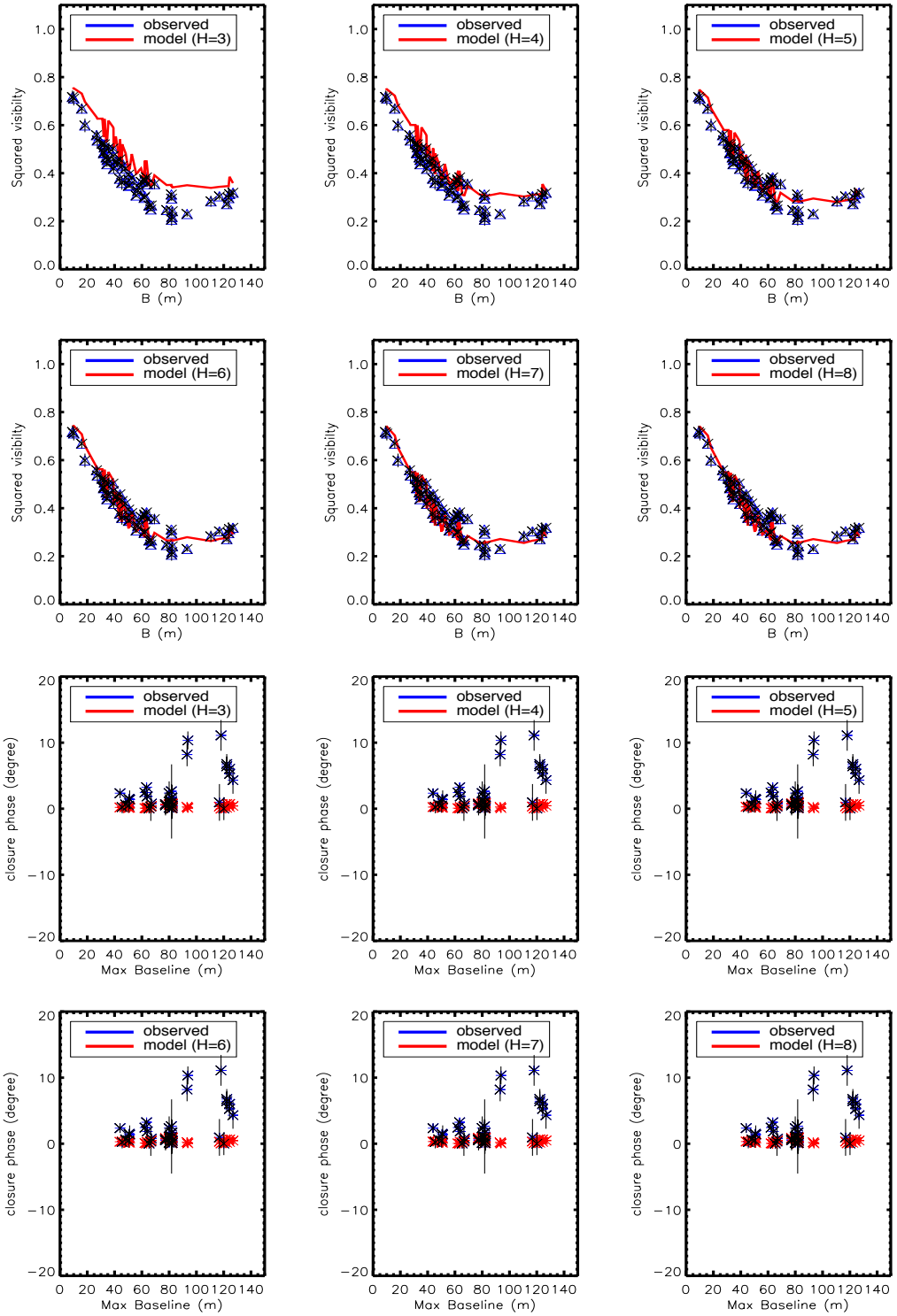

FIGURE 4.11: Top: Visibilities versus baseline for different scale heights of the inner disk at 100 AU and bottom: Closure phase versus Maximum baseline for different scale heights of the inner disk at 100 AU at λ=1.656 μm.

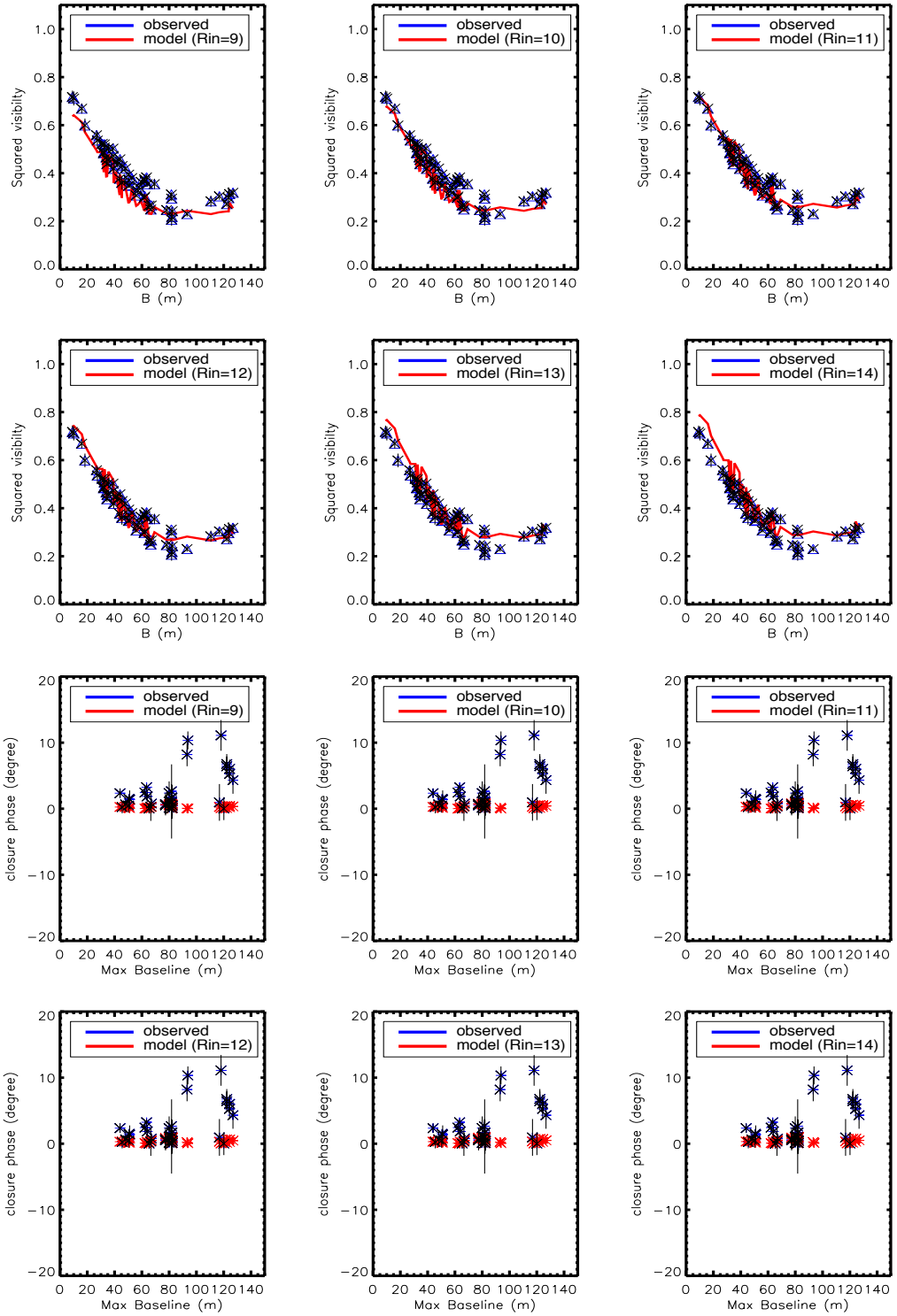

FIGURE 4.12: Top: Visibilities versus baseline for different inner radii of the outer disk and bottom: Closure phase versus Maximum baseline for different inner radii of the outer disk at λ=1.656 μm.

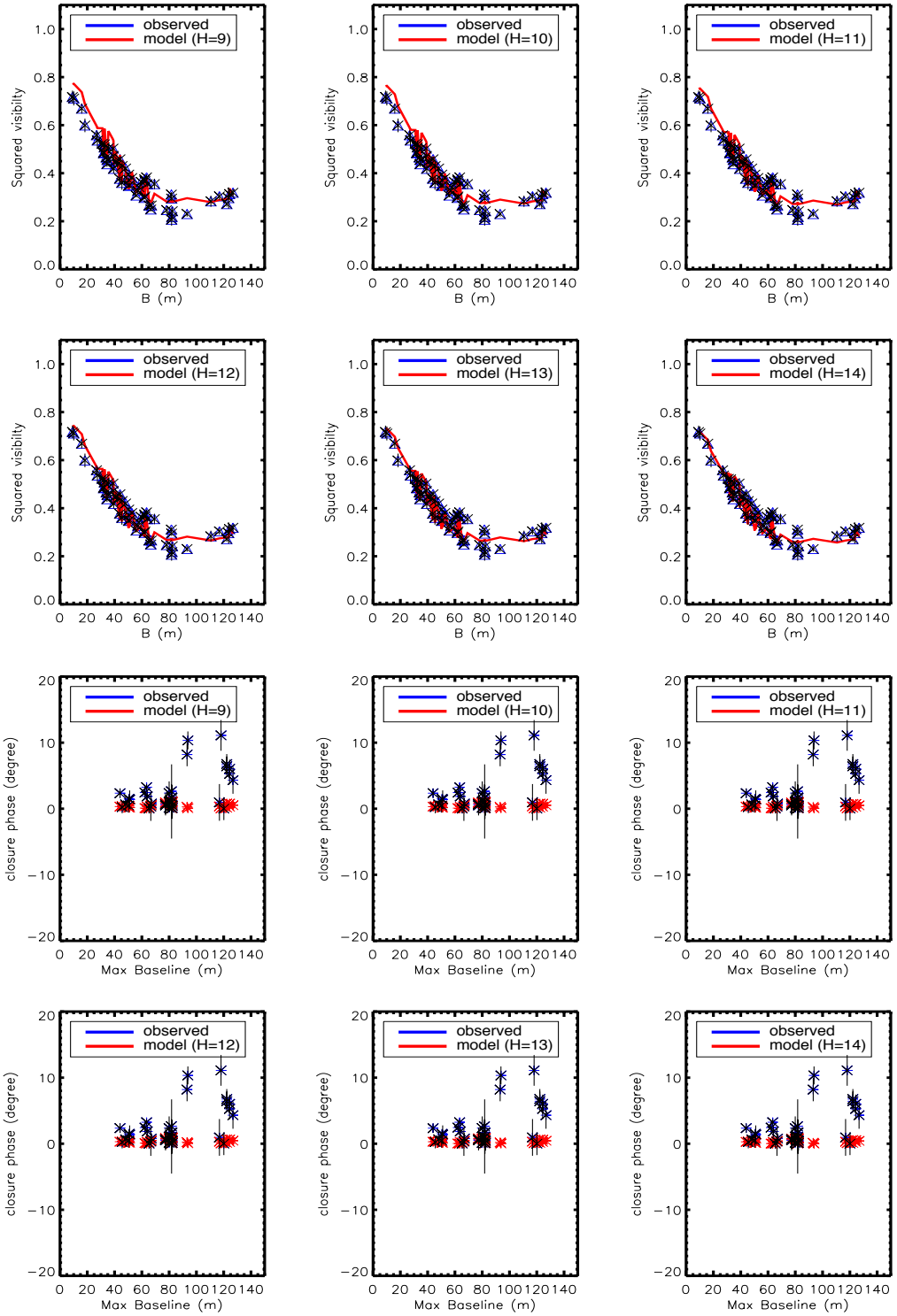

FIGURE 4.13: Top: Visibilities versus baseline for different of the scale heights of the outer disk at 100 AU and bottom: Closure phase versus Maximum baseline for different scale heights of the outer disk at 100 AU at λ=1.656 μm.

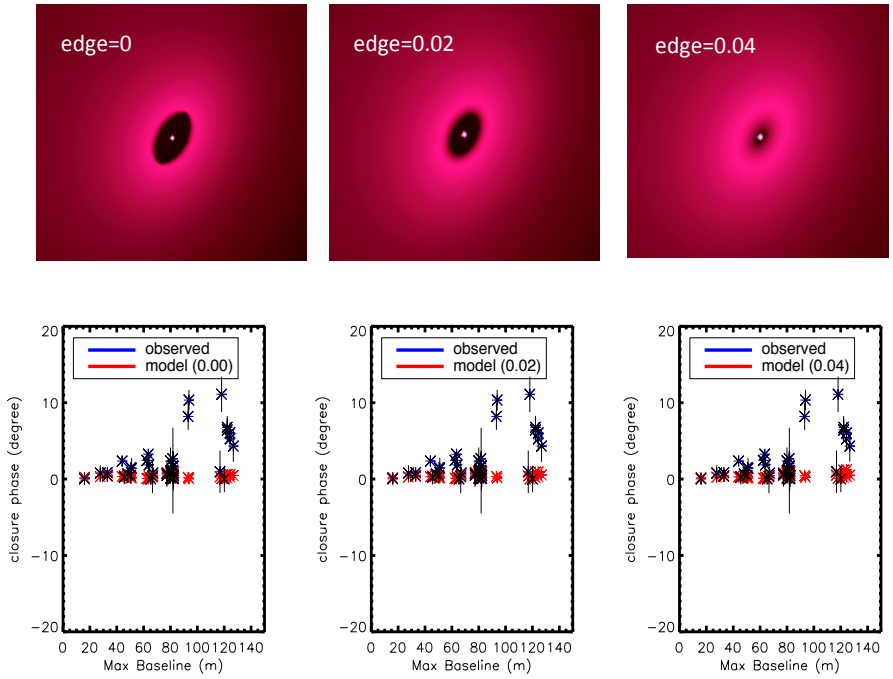

FIGURE 4.14: Top: The synthetic image of the inner rim of the inner disk for three different values of the edge. Bottom: The effect of the edge of the inner rim of the inner disk on the closure phase.

The natural departure from centro-symmetrical models could be due to the inclination. If the disk is faced-on, there is no asymmetry in the brightness distribution. As the disk gets inclined, this inclination may produce a natural asymmetry in the disk. In Fig. 4.7, we show that the inclined disk models fail to reproduce the non-zero closure phase for the long baselines. As we mentioned before, an edge value of zero creates a sharp inner rim. For an inclined disk, this sharp inner rim could produce an asymmetry as mentioned by Isella et al. 2015. However, Fig. 4.14 shows that even a sharp inner rim with an edge value of zero can not produce any asymmetry to match our non-zero closure phase at long baselines.

Inner disk properties:

We constrain the location of the disk inner edge at 0.25 AU from the central star. The inner disk is composed of micron size astronomical silicate grains, which contribute to the scattered light as an influential part of total H-band emission of the disk. Larger grains need to be included, i.e., a_{max}=5 μm, to survive at the inner edge of 0.25 AU derived by the interferometric observations. Exploring the free parameters used in the MCFOST code, we constrain the scale height of the inner disk at 6 AU, consistent with B10 and T11. In order to reproduce the SED and the visibilities, we find a lower dust mass of 0.5×10^{-10} $M_{\odot}$ for the inner disk compared to T11 (Table 4.2). As we mentioned

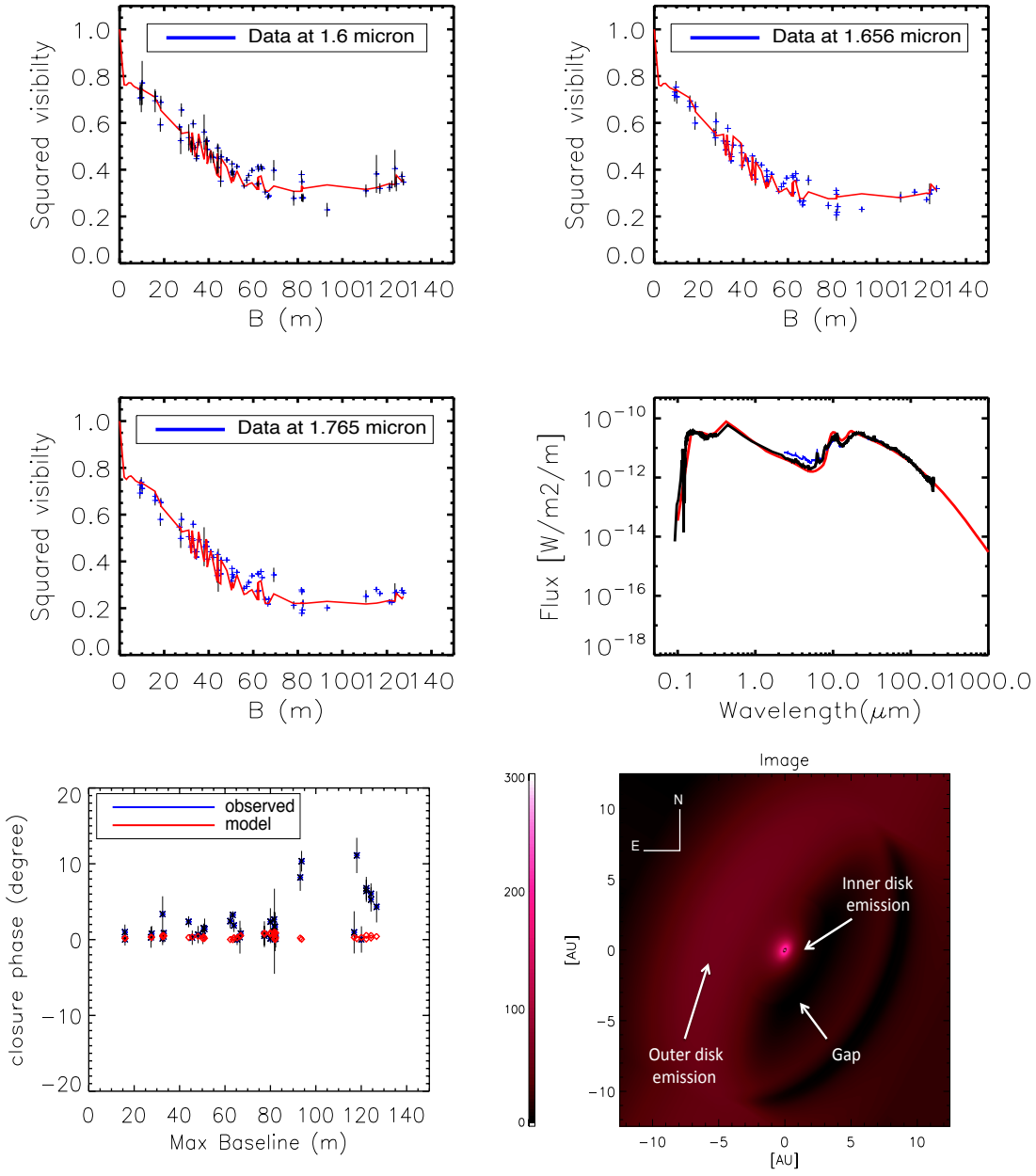

FIGURE 4.15: Best model to the SED and PIONIER data. Top, middle-left and bottom-left panels: Visibilities for three wavelengths, i.e., 1.6, 1.656 and 1.765 μm (red solid lines) and closure phase (red crosses) for wavelength 1.656 μm, compared with the interferometric observations (black crosses and error bars). Middle-right: Observed spectral energy distribution of HD 100546 (black and blue lines) compared to our best-model prediction (red solid line). Bottom-right: The synthetic image of HD 100546 at λ=1.656 μm. This image has been plotted taking into account the Auxiliary Telescope's field of view of λ/D 25 AU. The "kink" in the visibility plots at B $\sim$ 10 m is a real feature caused by the sharp inner edge of the outer disk as discussed in T11.

before, the mass of the inner disk has an important effect on the visibility. We can not reproduce the visibility if we keep the mass of the inner disk as in T11. As we show in Fig. 4.4, 0.5×10^{-10} $M_{\odot}$ is the best value to reproduce the visibility. Since our data provide a good coverage of the spatial frequency (See Fig. 4.1), we are also able to estimate the inclination and position angle of the inner disk. The values are $i = 48 \pm 6°$ and PA$=119 \pm 14°$ respectively.

Gap and outer disk properties:

The extended emission of the outer disk is within the telescope field of view and not the interferometer one. This affects the visibility profile at short baselines and decreases the value of the visibility down to 0.8. In Fig. 4.15, the "kink" in the model visibilities at B $\sim$ 10 m is caused by the outer disk that has a sharp inner edge. We constrain the value of 12 AU for the inner radius of the outer disk. T11 found a value of 13 AU and suggest that the gap must end somewhere between 9 AU and 17 AU. The scatter in their data did not allow them to estimate better the inner radius of the outer disk. We also constrain a value of 12 AU for the scale height of the outer disk. We slightly reduced the mass of the surface layer down to a value of 2×10^{-7} $M_{\odot}$ compared to the value set by T11, i.e., 3×10^{-7} $M_{\odot}$ to reproduce better the visibility mostly for intermediate and shorter baselines as we show in Fig. 4.6

4.6 Do we have evidence for a clumpy structure?

As we demonstrated in previous section, the natural departure from centro-symmetrical disk models caused by inclination effects on the radiative transfer of the sharp inner rim edge of the disk can not explain the non-zero closure phase for long baselines (See. Fig. 4.15). This fact leads us to propose that the inner rim of the disk of HD 100546 might not be smooth. Indeed, to match the closure phase, an asymmetry in the inner rim is needed. This asymmetry could be a companion or a local dust concentration in a clump. We propose that the presence of a clump of dust, related to planet formation could generate such an asymmetry. This scenario is motivated by indirect evidence of clumpiness in this star as revealed by photometric variability (Mendigutía et al., 2015; Brittain et al., 2015).

To construct our model, we add to our best MCFOST simulation a clump of dust with a fixed angular diameter of 2 mas characterized by its position angle and the distance from the central star and its flux.

We explore the coordinate parameters for different values of the flux ratios to minimize χ^2. In Fig. 4.16, we plot the χ^2 surface map in terms of Right Ascension (RA) and

TABLE 4.3: Best parameters of the clump of dust for 1.656 μm.

Parameter	Value
Distance (AU)	$0.25^{+0.06}_{-0.05}$
P.A. (°)	56^{+15}_{-11}
Flux ratio	$0.085^{+0.08}_{-0.05}$

Declination (in mas) for the best flux ratio between the star and the clump at 1.656 μm. We over plotted the best inner edge of the inner disk in AU derived from our interferometric data. The best values of the clump are presented in Table. 4.3. We find a satisfying χ^2_r, i.e., 1.43. We illustrate our best model including the clump in Fig. 4.17.

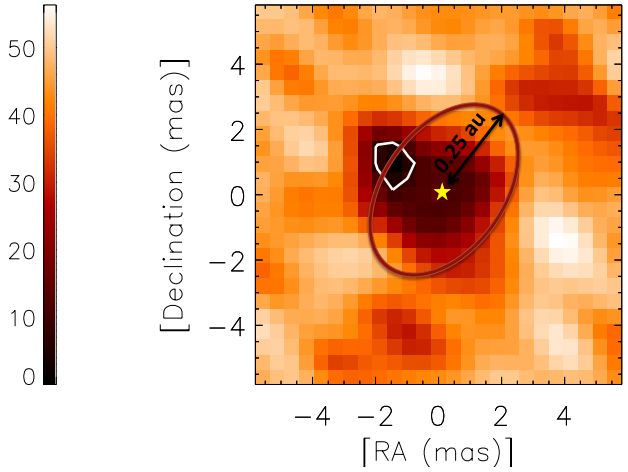

FIGURE 4.16: The plot of χ^2 surface map in terms of RA and Declination in mas for 1.656 μm. The red narrow ring is the position of the inner rim constrained by our best model without clump. The minimum χ^2 in black color is related to the best position of the clump. The white contour is indicative of the σ^2-1 boundary.

Results:

In Fig. 4.17, we show the effect of the clump on the visibilities and on the closure phase. As we see in this figure, the visibility plots compared to the ones without the clump have few bounces, which could be due to the effect of the clump.

For the closure phase, we see a significant effect in Fig. 4.17. Compared to Fig. 4.15, closure phase values of our best model especially for longer baselines can be matched with data with $10 - 15°$ deviation from zero. We could successfully reproduce the closure phase, the visibilities and the SED simultaneously. The synthetic image of our best model including a clump of dust is represented in Fig. 4.17.

If the clump has moved, knowing the period of its movement is of importance. With a location of the clump found to be at $0.25^{+0.06}_{-0.05}$ AU from the central star, and knowing

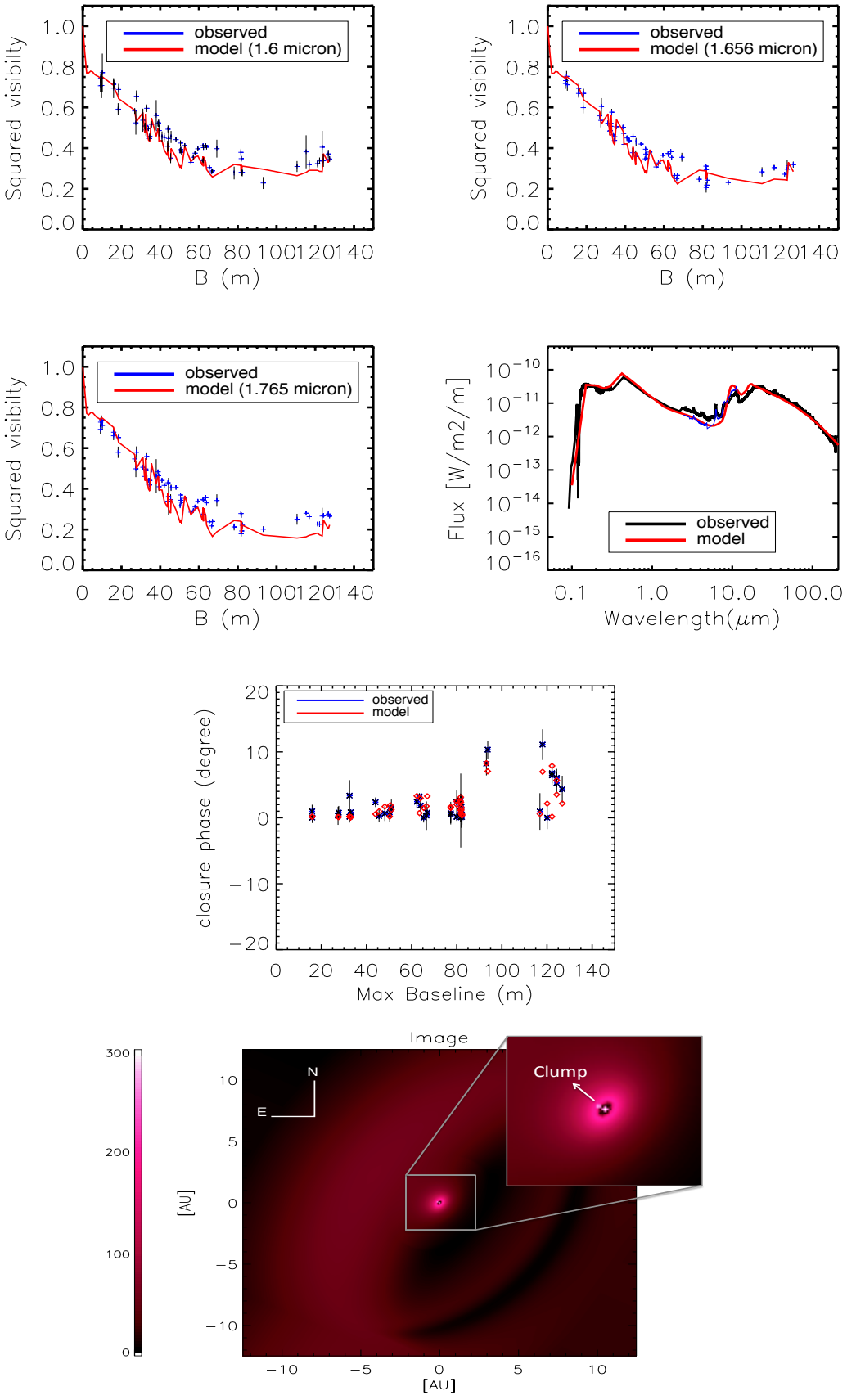

FIGURE 4.17: Best model to the SED and PIONIER data with the clump. See caption of Fig. 4.12.

the mass of the star $M_\star$=2.4 ± 0.1 $M_\odot$ (Van den Ancker et al. 1997), the orbital period of this clump can be estimated to T=0.38 ± 0.09 year. As we mentioned in previous sections, the non-zero closure phase is mostly seen for long baselines greater than ∼ 90 m. As we represented our data in Table 4.1, measurements at the long baselines greater than 85 m were obtained in 3 days, i.e., 29/01/2013, 30/01/2013 and 01/02/2013. These three days are less than the period of the clump, T=0.38 ± 0.09 year. This shows that the clump can not be tracked by our observations and we can assume that during our observations it has not moved.

4.7 Conclusion

We have validated a model of the inner structure of the HD 100546 pre-transitional disk through a radiative transfer modeling of our new and unique PIONIER dataset. We constrain the structure of the inner disk as well as provide more precise constrains on the outer disk inner edge.

1) Exploring the parameters of MCFOST code, we obtained the best model comprising of (i) an inner disk with a dust mass of ∼ 0.5×10^{-10} $M_\odot$ from ∼ 0.25 AU to ∼ 4 AU,

(ii) a gap from ∼ 4 AU to ∼ 12 AU,

(iii) a surface layer on the top of outer disk with a dust mass of ∼ 2×10^{-7} $M_\odot$ extended from ∼ 12 AU to ∼ 50 AU,

(iv) a massive outer disk with a dust mass of ∼ 4.3×10^{-4} $M_\odot$ extending from ∼ 12 AU to ∼ 500 AU.

This model reproduces the visibilities and the SED but not the closure phase for longer baselines.

2) We show that the presence of a clump of dust can reproduce our closure phase simultaneously with the visibilities and the SED. To minimize χ^2, we explored the free parameters of the clump, i.e., the position angle and the distance from the central star, for different values of the flux ratio between the clump and the central star. As a result, we obtained a clump at a distance of $0.25^{+0.06}_{-0.05}$ AU from the central star and a position angle of 56^{+15}_{-11} degree for the clump for a best flux ratio of 0.085.

Chapter 5

Study of the inner disk of the Herbig star MWC 480

5.1 Abstract

The inner structure and properties (e.g., temperature, mass) of the circumstellar disk of Herbig star MWC480 are studied by the stellar interferometry method used in the infrared and are interpreted using semi-analytical models. From these models, the SED was reproduced and the intensity map of the source was calculated. The intensity map provides the input for modeling the Keck Interferometer (KI) data at near-IR wavelengths and the mid-infrared instrument MIDI data at mid-IR wavelengths installed on VLTI. We conclude that with our limited set of data, we can reproduce the SED, the Keck and the MIDI visibilities using a two-component disk model. Furthermore, we suspect that MWC480 has a transitional dusty disk. However, we need more MIDI observations with different baseline orientations to confirm our modeling.

5.2 Introduction

Circumstellar disks around young stellar objects provide the physical conditions at the origin of the formation of planets.

MWC480 (HD 31648, A2/3ep + sh) is an Herbig Ae star of 1.8 $M_{\odot}$ (Simon et al. 2000) located at $d = 137 \pm 31$ pc (van Leeuwen 2007). This star is one of the brightest Herbig Ae stars at millimeter wavelengths (Mannings et al. 1997) surrounded by a Keplerian disk (Mannings et al. 1997; Simon et al. 2000; Pietu et al. 2007). The existence of

a disk around this star was first reported by Mannings et al. (1997). These authors and Mannings and Sargent (1997) have mapped the thermal dust millimeter-continuum and gaseous CO emission towards MWC480 and found that a circumstellar (CS) disk surrounding the star has an extent of 85 AU (FWHM). The disk continuum emission was resolved by Pietu et al. (2006). The IR excess of the object was investigated by Sitko (1981) and Meeus et al. (2001). The dust disk can be studied in the infrared domain through its infrared emission and the gas disk can be studied in spectral lines since hydrogen in accretion flows or in the innermost regions of outflows can be ionized. One of the hydrogen spectral lines which has special importance is the Brγ line, that is strongly correlated with accretion onto young stars (Muzerolle et al. 1998). In this chapter, we report the first interferometric observations of MWC480 using the VLTI instrument MIDI (Leinert et al. 2003), observing in the N band (8—13 μm). We simultaneously modeled the SED, the near-IR and mid-IR interferometric data of MWC480 to constrain the overall spatial structure of the inner disk region.

5.3 Observations

5.3.1 MIDI observations and data reduction

Using the instrument MIDI of the VLTI (Leinert et al., 2003) in operation at the ESO Paranal Observatory, MWC480 has been observed during one night in 2007. This observation was carried out on the 4th of February 2007 in one run using the 8m Unit Telescopes (UTs). The observations were performed using the prism as the dispersive element giving a spectral resolution of R $\sim$ 30 in the N-band. I reduced MIDI data by help of Sebastien Flament and Alain Spang at Observatoire de la Cote d'Azur (OCA). We obtained three fringe and photometry measurements for MWC480 using the HIGH-SENS mode. In this mode, the photometry or total flux is measured just after the fringe acquisition. In order to calibrate the visibility of the science target, we select HD20644 as calibrator. This calibrator was selected from the MIDI calibrator list with the SearchCal JMMC[1] tool. This tool provides a validated database for the calibration of long-baseline interferometric observations (Bonneau et al., 2006).

MWC480 also was observed with the KI in 2007 by Eisner et al. (2009). We downloaded the reduced data from the Keck Archive (See. Fig. 5.1). The peak in the Keck data, which has higher visibility value is related to the Brγ emission at 2.165μm.

We show a summary of the observing log, containing the length and Position Angle (P.A.) of the projected baselines in Table 5.1.

[1] http://www.mariotti.fr/

The UV coverage of the interferometric observations is shown also in Fig. 5.1.

The calibration of the visibility measurements and total flux of MWC480 were performed using the data-reduction software package named MIDI Interactive Analysis (MIA) and Expert WorkStation [2](EWS). This software performs a coherent analysis of dispersed fringes to estimate the complex visibility of the source. The method and the different processing steps are described in Jaffe (2004). The calibrated visibilities were then obtained by dividing each raw visibility measurement by the instrumental visibility measured on the closest calibrator in time.

5.3.2 Spectroscopic observations

We tried to obtain the uncorrelated flux using VLTI/MIDI for wavelengths 8–13.5 μm. In Fig. 5.1, we show this flux in the SED with pink color. To have the same date observations with the interferometric observations in 2007 in the SED, we used the SpeX data (SpeX is a medium-resolution 0.7-5.3 μm spectrograph built at the Institute for Astronomy (IfA), for the NASA Infrared Telescope Facility (IRTF) on Mauna Kea) and the BASS data (BASS is a medium resolution 3-14 μm spectrometer) (Kusakabe et al., 2012). We show these data in the SED with red color (See Fig. 5.1).

5.3.2.1 Variability

Sitko et al. (2008), Grady et al. (2010) and Kusakabe et al. (2012) reported the variability of MWC480 in the near- and mid-IR emission. It is now well-established that the near-IR and mid- to far-IR variability are often anti-correlated, at least in transitional disks (Kusakabe et al., 2012). The most likely scenario is changes in the scale height of the inner disk. This leads to changes in the shadowing of the outer disk so that the illumination by the central star changes with time. This affects both the scattered light by dust particles (e.g., Kusakabe et al., 2012) and thermal emission (e.g., Tannirkulam et al., 2007). Kusakabe et al. (2012) do show that this variability in the near-IR is due to the scale height variability of the dust disk at the sublimation radius, which can affects the shadowing of entire disk. Sitko et al. (2008) also detect the mid-IR photometric variability for MWC 480. As we mentioned above, in most cases of transitional disks, the near- and mid- to far-IR variability are anti-correlated. For instance, if the scale height of the dust disk at the sublimation radius is smaller than usual, which means that the object is observed in its minimum brightness state in the near-IR, the outer

[2]The software package is available at http://home.strw.leidenuniv.nl/∼jaffe/ews/index.html and the software manual is available at http://home.strw.leidenuniv.nl/∼jaffe/ews/MIA+EWS-Manual/index.html

TABLE 5.1: Log of observations. The MIDI observations come from a program prepared by Di Folco et al. (2007), the Keck observations come from the Keck Archive with program ID of 'ENG' by Eisner et al. (2007).

Instrument	**Telescopes**	**Date**	B_p **[m]**	**P.A.** [°]
MIDI	UT2-UT3	2007–02–04	42.8	52°
KI/V2	K1-K2	2007–07–03	84.9	48°

disk is expected to be detected more in scattered light than in its maximum brightness state (Kusakabe et al., 2012). According to Fig. 5.1, for the SED, we used the ISO data obtained in 1998 for wavelengths 2.3–198 μm (Creech-Eakman et al., 2002). The ISO data have almost less than 10% difference with the brightness state in 2007 data in the near-IR according to Fig. 5 of Kusakabe et al. (2012). We used also the Spitzer data for wavelengths of 3–198 μm by Houck et al. (2004). As we see in Fig. 5.1, these data compared to other data we represent in this figure are in the maximum brightness state in the near-IR.

Results According to Fig. 5.1, the total flux obtained by the MIDI observation in 2007 between wavelengths 8–13.5 μm are almost consistent with the BASS data in 2007. Since there were no data available for wavelengths 20–200 μm in 2007, we used the ISO data from 1998, which have less than 10% difference with the brightness state in the near-IR with 2007 data. As we mentioned above, the Spitzer data are in the maximum brightness state in the near-IR of the SED and roughly a factor of 2 above the 2007 data. We over plotted these data only to show how the near-IR flux affects on the outer disk. As we represent in Fig. 5.1, although the Spitzer data are a factor of almost 2 above the 1998 and 2007 data in the near-IR, for wavelengths $\sim$ 4–8 μm, they are a factor of roughly 2 below the 2007 and 1998 data for wavelengths $\sim$ 8–15 μm.

5.4 Modeling

I developed and compared some semi-analytical models to study the circumstellar environment of the Herbig star MWC480 based on IDL program. The semi-analytical models simulate the disk emission assuming different possible geometries and dust opacities. The models allowed me to reproduce the KI and MIDI visibilities and the SED. I explored a range of possible parameters describing the object including the size and mass of the disk for example.

I constructed a disk model with a temperature gradient. The temperature decreases with increasing radius. In my model, I computed the visibilities from the Fourier transforms of the image for the star plus the disk at each wavelength. The star was modeld by

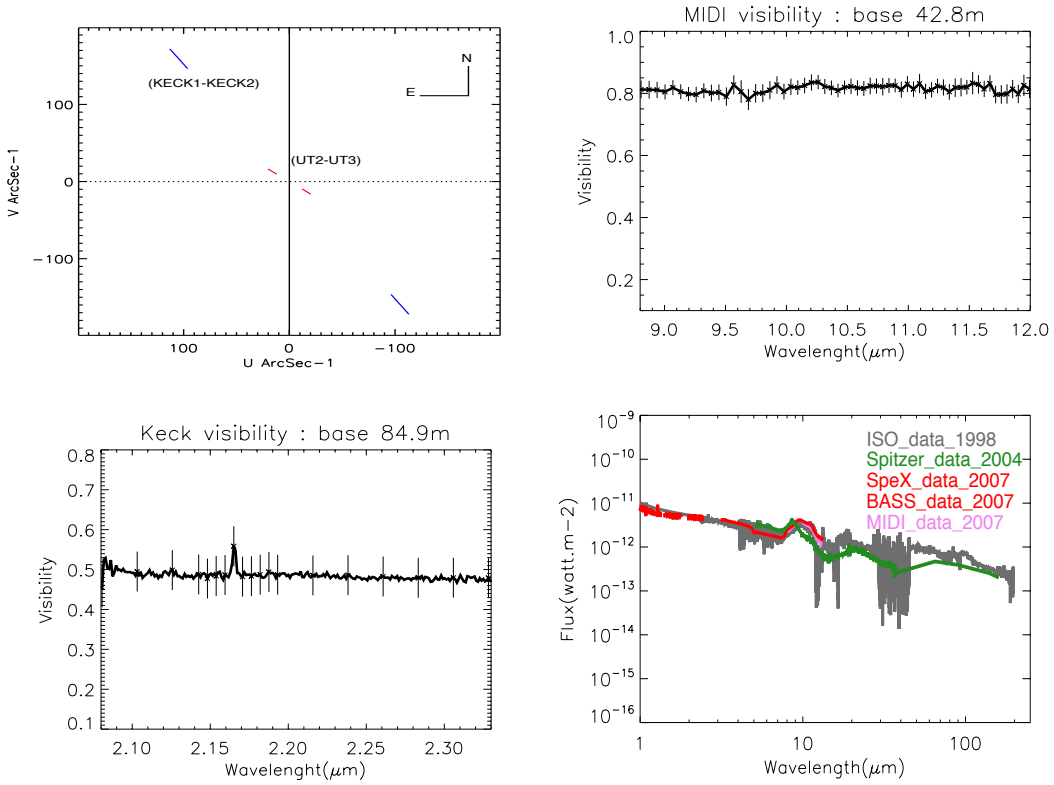

FIGURE 5.1: Top left: UV coverage for the two sets of observations; the red color refers to B =42.8 m and blue color refers to B =84.9 m (as detailed in Table 5.1). Top right: Measured N-band visibility of MWC480 (with error bars) as a function of wavelength. Bottom left: Measured K-band visibility of MWC480 (with error bars, which are selected for few points because of plenty of Keck data). Bottom right: ISO data in 1998 between wavelengths 2.2 μm and 200 μm in gray color, averaged MIDI uncorrelated spectrum in 2007 between wavelengths 8 μm–13.5 μm in pink color, SpeX and BASS data in 2007 for wavelengths 0.8 μm–5.5 μm and 5.8 μm–14 μm respectively in red color and Spitzer data in 2004 for wavelengths 4 μm–180 μm in green color.

a blackbody $B_\lambda(T_\star)$. B_λ is the monochromatic intensity represented by the Planck function. The star has an angular radius of $\alpha_\star$=$R_\star$/d in radians, where d is the distance of the star and $R_\star$ is the stellar radius.

The total received flux is $B_\lambda(T_\star) \times (\pi\ {\alpha_\star}^2)$ expressed in Wm^{-2} m^{-1}, where $\pi\ {\alpha_\star}^2$ is the solid angle of the star seen from the observer and $T_\star$ is the stellar temperature.

The disk was also modeled by a black body emission $B_\lambda[T(r)]$, where $T(r)$ is the temperature law according to the distance r to the star. In fact for an optically thick disk, the disk will emit as a black body. However, as described below, the vertical optical depth of the disk itself is related to the opacity of the dust material that has to be taken into account. We adopted a power law form for $T(r)$:

$$T(r) = T_{in}\left(\frac{r}{r_{in}}\right)^{-q}, \tag{5.1}$$

with q ranging from 0.5 (flared irradiated disks) to 0.75 (flat irradiated disks), see e.g., Pringle (1981). T_{in}=T_g is the temperature of a free grain[3] located at r=r_{in} which is the inner radius of the disk.

Equating the absorption and the emission of a grain with non-chromatic (gray) absorptivity, one can calculate the T_{in} at r_{in} in Eq.(1):

$$T_{in} = T_g = T_\star\left(\frac{R_\star}{2r_{in}}\right)^{\frac{1}{2}}, \tag{5.2}$$

when the disk is optically thick (we are interested in the optical depth in the vertical direction, assuming the observer is looking nearly perpendicularly to the disk), then for each surface area s_{disk} of the disk, the observer receives $B_\lambda[T(r)] \times (s_{disk}/d^2)$. The quantity s_{disk}/d^2 represents the solid angle of each elementary surface area[4] of the disk seen at the distance d. Defining r_{in}, r_{out}, $T(r)$, $\Sigma(r)$ and κ_λ completely characterizes the disk. r_{out} is the outer radius of the disk, κ_λ is the opacity of the dust and $\Sigma(r)$ is the surface density law. The quantity $B_\lambda(T_r)[1 - exp(-\tau_\lambda(r))]$ represents the general expression of the brightness of the surface of the disk according to $\tau_\lambda(r)$, the optical depth in the vertical direction (Beckwith et al., 1990; Dullemond et al., 2001). In this case, the observer receives $B_\lambda[T(r)]\ [1 - exp(-\tau_\lambda(r))]\ (s_{disk}/d^2)$. When the disk is inclined by an angle i, this quantity becomes

$$B_\lambda\left[T(r)\right]\left[1 - exp\left(-\frac{\tau_\lambda(r)}{cos(i)}\right)\right]\left(\frac{s_{disk}}{d^2}\right) \tag{5.3}$$

The relation of $\tau_\lambda(r)$ with surface density and κ_λ is described as below

$$\tau_\lambda(r) = \Sigma(r)\kappa_\lambda \tag{5.4}$$

We used the dust opacity from Fig. 3 of Thi et al. (2010), computed from Mie theory for a grain size distribution following the "$a^{-3.5}$" power law and with a minimum size of 0.02 μm and three values of the maximum grain size (a_{max}=[10, 50, 200] μm). The power law form for $\Sigma(r)$ is described as

$$\Sigma(r) = \Sigma_0\left(\frac{r}{r_0}\right)^{-p} \tag{5.5}$$

[3] A grain illuminated directly by the central star assuming no radiative exchange with other grains.
[4] The elementary surface area of the disk is defined by our pixel size in the images of our model.

In the models of Dullemond et al. (2001) and Chiang and Goldreich (1997), Σ_0 has been considered at $r = 1$ AU, while in e.g., Dutrey et al. (1998), Dutrey et al. (2011), who used millimeter observations, Σ_0 is assumed to be defined from the outer radius of the disk. Since we measured directly by long baseline interferometry, the dusts located at the inner radius, we choosed to consider Σ_0 from r_{in}. Therefore in our model, the $\Sigma_0 = \Sigma_{in}$ and r_0=r_{in} gives

$$\Sigma(r) = \Sigma_{in} \left(\frac{r}{r_{in}} \right)^{-p} , \tag{5.6}$$

where p ranges from 1 (assuming constant mass accretion rate at constant viscosity) to p= 1.5 as inferred for the MMSN (Minimum Mass Solar Nebula) (Weidenschilling, 1997) and assumed often as a basis in other disk models (e.g., Chiang and Goldreich (1997); Dullemond et al. (2001); Eisner et al. (2009)). Σ_{in} is related to the total mass amount of the dust. The mass of the dust is given by

$$M_{dust} = \int_0^{2\pi} \int_{r_{in}}^{r_{out}} \Sigma(r)\, \mathrm{d}r\mathrm{d}\theta \tag{5.7}$$

Combining Eq.(5.6) and Eq.(5.7) gives

$$\Sigma_{in} = \frac{M_{dust}}{2\pi r_{in}^2 f} , \tag{5.8}$$

where

$$f = \frac{1}{2-p} \left[\left(\frac{r_{out}}{r_{in}} \right)^{2-p} - 1 \right] \tag{5.9}$$

Combining Eq.(5.4) and Eq.(5.6) gives

$$\tau_\lambda(r) = \tau_{\lambda,in} \left(\frac{r}{r_{in}} \right)^{-p} , \tag{5.10}$$

where

$$\tau_{\lambda,in} = \Sigma_{in} \kappa_\lambda \tag{5.11}$$

We modeled the circumstellar Brγ emission by including additional flux at 2.165μm produced in the inner region of the disk as an optically thin isothermal gaseous disk. The flux received from Brγ emission is calculated as

$$B_\lambda \left[T(r) \right] \left[1 - exp \left(- \frac{\tau_\lambda(r)}{cos(i)} \right) \right] \left(\frac{s_{ring}}{d^2} \right) , \tag{5.12}$$

TABLE 5.2: The best parameters and their explored ranges for the one-component disk model.

Parameters	**Best-Values**	**Explored Ranges**	$\chi^2_{r\ total}$
M_{dust} **(a_{max}=10 μm)**	$2.4 \times 10^{-11}\ M_\odot$	10^{-12}...$10^{-7}\ M_\odot$	
M_{dust} **(a_{max}=50 μm)**	$0.5 \times 10^{-10}\ M_\odot$	10^{-12}...$10^{-7}\ M_\odot$	
M_{dust} **(a_{max}=200 μm)**	$10^{-10}\ M_\odot$	10^{-12}...$10^{-7}\ M_\odot$	12.75
p	1.5	0.1...1.98	
q	0.5	0.4...0.9	
r_{in}	0.27 AU	0.1...0.4 AU	

where s_{ring}/d^2 represents the solid angle of each surface area of the ring of Brγ emission seen at the distance d.

To minimize the parameters of our model, we used the parameters of Eisner et al. (2009) in order to reproduce the effect of Brγ in the Keck visibility. Therefore, we assumed that the emission arises from a gaseous ring with $\tau_{\lambda,in} \approx 0.08$ and $T(r_{in}) \approx 3500$K located in $r_{in} \approx 0.07$ AU. In our model, we assumed that the outer radius of the gaseous ring is 0.09 AU (Eisner et al., 2010), while in Eisner et al. (2009) the gaseous disk was extended until the sublimation radius. In fact, the Brγ emission may even arise from a more compact region, but we could not constrain such small size scales with the available angular resolution and the limitation of our model.

5.4.1 Application to the one-component disk model

The excess in the infrared for MWC480 has been modeled by Eisner et al. (2007). However, after considering a thick disk emission, a residual near-IR excess between $\sim$ 2–10 μm could not be explained. Eisner et al. (2009) then considered a gaseous disk plus a shell of dust to reproduce the whole infrared excess including the near-IR. We rather used an optically thin disk considering the temperature and surface density law according to Eq. (5.1) and Eq.(5.6).

For the SED, we considered only the SpeX and BASS data in 2007 for wavelengths 0.8–14 μm and ISO data in 1998 for wavelengths 15–200 μm and an over plot of total flux of MIDI data in 2007 for wavelengths 8–13.5 μm. In this model, the outer radius is fixed to a value of 80 AU (Mannings and Sargent, 1997). To minimize the number of free parameters, the inclination and P.A. of the disk have been kept unchanged with respect to previous studies. We fixed the inclination of the disk to the value derived from Simon et al. (2000), Piétu et al. (2006), Chapillon et al. (2012), namely i=37°. The position angle was fixed to the average disk semi-major axis P.A. of 57° derived from millimeter interferometry for an average of 5 CO and HCO+ transitions (Piétu et al.,

2007) and the P.A. of the jet obtained by Grady et al. (2010). In this model, we have four free parameters:

1) The dust mass for each maximum grain size M_{dust},

2) the surface density power-law exponent p,

3) the temperature power-law exponent q,

4) the inner radius r_{in},

- The effect of mass of the dust species:

The first important free parameter in our model is the total mass of the dust disk, M_{dust}. For three maximum sizes of grains in a size grain distribution, a_{max}=10 μm, a_{max}=50 μm and a_{max}=200 μm, we explored the total mass of the dust in the range $\approx 10^{-12}$–10^{-7} $M_{\odot}$. We derived the best value for each maximum sizes of grains (See Table 6.2). Increasing the mass of the dust further with respect to a_{max}, is not consistent with the SED in the range 2 μm to 10 μm, because larger masses cause an excess in the near-IR. However, it can roughly reproduce the flux of the SED in the range 10 μm to 200 μm. On the other hand, increasing the mass of the dust generates a decrease of the Keck and MIDI visibilities. Our model is formed by an unresolved star and a resolved disk surrounding. Increasing the dust mass increases thus the flux ratio of the disk to the star. Therefore, the Keck and MIDI visibility values decrease and disk becomes more resolved.

- The effect of the exponent of the surface density law, p:

The exponent of the surface density law, p, for a constant dust disk mass with respect to the maximum grain size (See. Table 5.2) was explored in the range 1-2. The best value we found was 1.5 as inferred for the protosolar nebula by Weidenschilling (1997). Increasing this exponent, meaning that the dust surface density decreases with a steeper slope, increases the flux of the SED just for the wavelengths from 1 μm to 13 μm. But it does not have any strong effect at longer wavelengths. Besides, it decreases the Keck visibilities and increases the MIDI visibilities.

- The effect of the exponent of the temperature law, q:

We have tested this exponent in the range 0.4-0.9. We derived the best value of $q = 0.5$. Increasing the exponent causes a decrease of the flux in the broad band SED especially at longer wavelengths. The Keck and MIDI visibilities both increase.

- The effect of the inner radius of the disk, r_{in}:

For a constant total mass of the disk with respect to the maximum grain size (See. Table 5.2), we derived an inner radius of r_{in}=0.27 AU, which is comparable to the one obtained by Eisner et al. (2009) for the dust sublimation radius. We explored this parameter in the range 0.1-0.4 AU. This parameter mostly affects the SED in the range 1–3 μm. Increasing r_{in} causes less flux in the range 1–3 μm and a shift of the maximum flux towards longer wavelengths. Besides, increasing r_{in} causes a decrease of both Keck and MIDI visibilities. But the effect of increasing r_{in} is more sensitive for the Keck visibility than for the MIDI ones. At 2 μm, the warm dust directly defines the inner rim.

As we explained in Chapter 3, to reduce the number of computed models, we started with a qualitative estimation of our free parameters. We explored the parameters starting from an existing solution based on a defined model basis and tried to narrow down the parameter estimations. The range of values, which have been explored and the values according to the best model are summarized in Table 5.2. The more sensitive parameters with respect to the visibilities are ranked first in this Table. We calculated a reduced χ^2, which corresponds to the best parameters can reproduce all our measurements. χ^2 is calculated by the sum of squared subtraction between the model and the data divided by the squared of the error bars of the data. The reduced χ^2, χ^2_r, is the χ^2 divided by the number of degrees of freedom, which is the subtraction between the number of data point and the number of free parameters. In Table 5.2, we show the χ^2_r for the best parameters. Taking into account the SED in calculation of χ^2, we find a χ^2_r equal to 12.75.

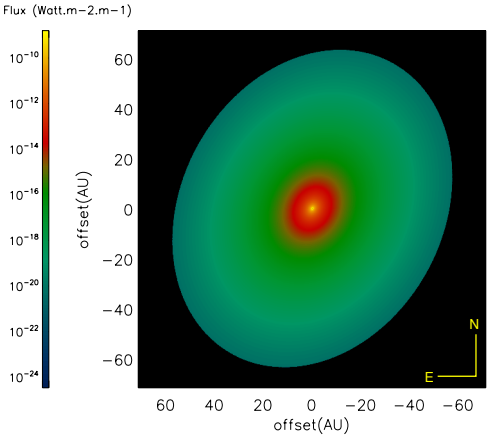

FIGURE 5.2: The synthetic image of MWC480 at λ=10 μm for the one-component disk model.

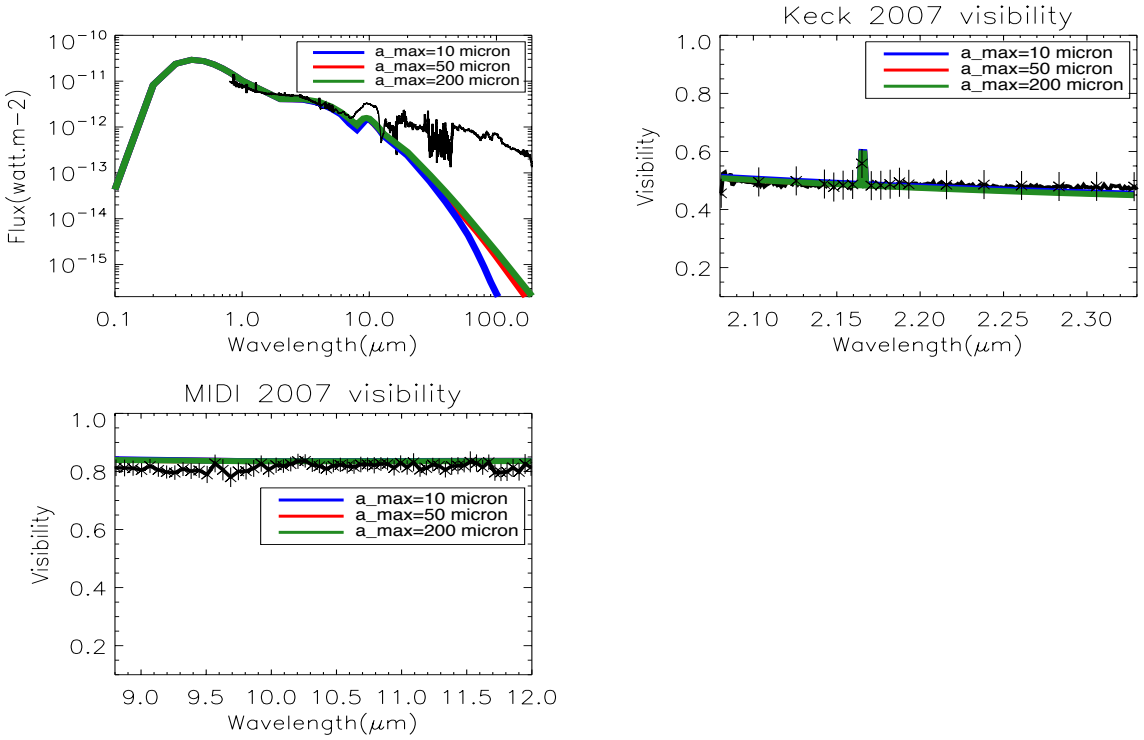

FIGURE 5.3: One-component disk model. The effect of the maximum grain size (a_{max} = 10 μm, a_{max}=50 μm and a_{max}= 200 μm) is compensated by an adjustment of the dust mass: M_{dust}=2.4× 10^{-11} $M_{\odot}$, M_{dust}=0.5× 10^{-10} $M_{\odot}$ and M_{dust}=10^{-10} $M_{\odot}$, respectively. The black solid lines in plots represents the observational data. For the SED, SpeX and BASS data for 0.8.-14 μm and ISO data in 1998 for 15–200 μm. MIDI uncorrelated spectrum between 8–13.5 μm.

5.4.1.1 Results

The one-component disk model reproduced simultaneously the SED from wavelengths 2 μm to 8 μm and the Keck and MIDI visibilities as well. In fact, an optically thin disk decreases the near-IR extra emission described in Eisner et al. (2007). In Fig. 5.2, we show the synthetic image of this model. In Fig. 5.3, we represent the SED, the Keck and the MIDI visibilities. According to Fig. 5.3, the maximum grain size of the dust has a weak influence on the near-IR emission. On the other hand, there is a small effect on the wavelengths 30–70 μm in the SED. MIDI visibilities does not change for the three maximum grain sizes. The maximum grain size of 50 and 200 μm are more consistent with the SED (See. Fig. 5.3).

There is, however, one issue in this model:

The model presented a deficit of the emission at wavelengths 8-200 μm. We then may need to use another component for the disk of MWC480 to compensate this lack of longer wavelengths emission.

TABLE 5.3: The best parameters and their explored ranges for the two-components disk model for the maximum grain size of 200 μm

	First component	
Parameters	**Best-Values**	**Explored Ranges**
M_{dust}	$0.9 \times 10^{-10}\ M_{\odot}$	$10^{-12}...10^{-7}\ M_{\odot}$
p	1.5	0.1...1.98
q	0.5	0.4...0.9
	Second component	
Parameters	**Best-Values**	**Explored Ranges**
M_{dust}	$1.25 \times 10^{-7}\ M_{\odot}$	$10^{-12}...10^{-7}\ M_{\odot}$
p	0.6	0.1...1.98
q	0.5	0.4...0.9
r_{in}	52 AU	10...60 AU
	$\chi^2_{r\ total}$	
	7.45	

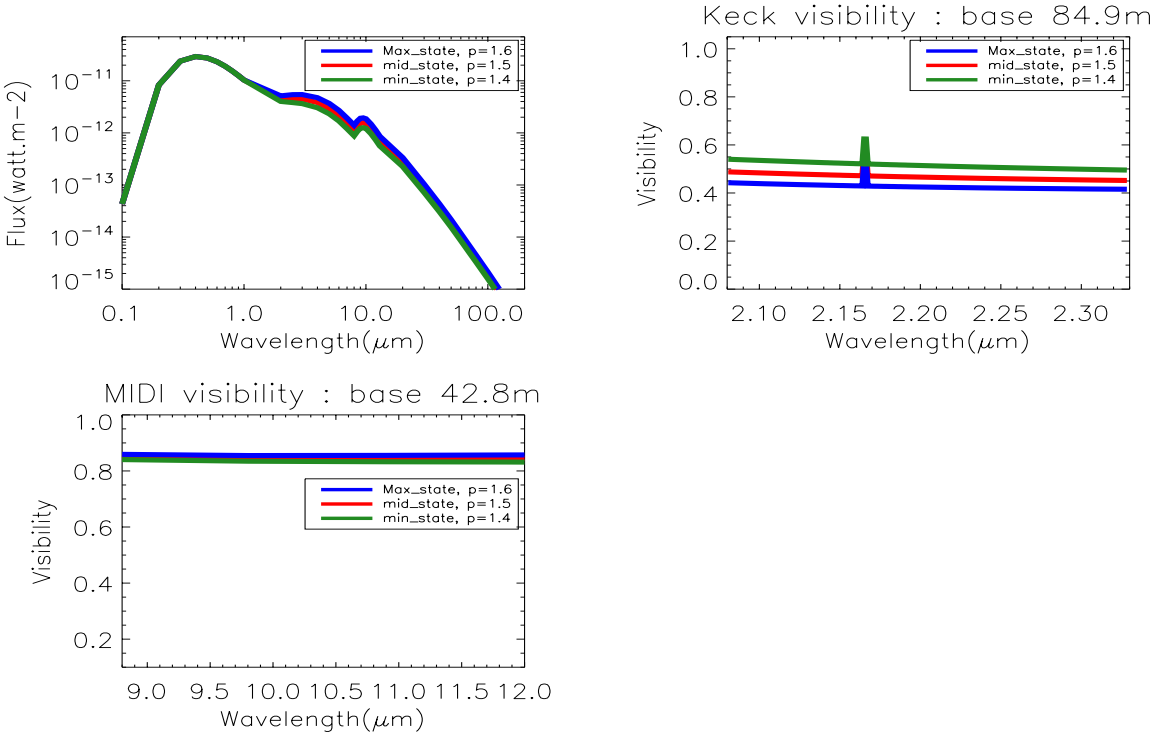

FIGURE 5.4: The effect of variability of the star in the near-IR in different brightness state for the maximum grain size of 200 μm in one-component disk model .

In Fig. 5.4, we modelled the variabilities assumed to be caused by the scale height of the inner disk. Different brightness state can be produced in the SED by modifying the exponent of the surface density law, p for constant dust mass and inclination. The p value is linked to the change of the scale height in the inner disk. The mid brightness state corresponds to the best parameter we found for p for the one-component disk model, which is almost consistent with the near-IR data in 2007. We show that the

variability of the scale height in the inner disk affects especially the Keck visibilities. In the maximum illumination state in the near-IR compared to mid and minimum one, there is more flux for the wavelengths from 1 μm to 13 μm. Besides, for the Keck visibilities, the maximum state has a lower visibility value compared to the mid and the minimum one, which means that the disk in the near-IR is more resolved for the maximum state. For the MIDI visibilities, the effect of brightness variability in the mid-IR induces a small change for the wavelengths 10–12 μm. Indeed, the disk in the mid-IR is more resolved when the source is in its minimum brightness state.

Since the variability of the source in the near-IR affects the visibilities, it is very important to use SED data that are taken at the same time as the interferometric observations.

However, even considering the variability in the near-IR as maximum or minimum illumination state, the lack of emission in the SED in the longer wavelengths ($\lambda >$ 10-20 μm) can not be explained by a one-component disk model.

5.4.2 Application to the two-component disk model

We found that using a second component in the disk of MWC480 is necessary since the one-component model for the disk of MWC480 could not reproduce the longer wavelengths emission. We considered a second component for the disk. We assumed that the first component is optically thin and the outer component is optically thick. The cool dust in the outer component of the disk emits at longer wavelengths which can compensate the lack of emission at longer wavelength in the SED.

The free parameters in this model are:

1) The total dust mass M_{dust} for the first component,

2) The total dust mass M_{dust} for the second component,

3) the surface density power-law exponent p for the first component,

4) the surface density power-law exponent p for the second component,

5) the temperature power-law exponent q for the first component,

6) the temperature power-law exponent q for the second component,

7) the inner radius r_{in} for the first component,

8) the inner radius r_{in} for the second component,

9) the outer radius r_{out} for the second component

We keep the inclination, P.A. and the outer radius of the disk identical to the values we considered for the one-component disk model.

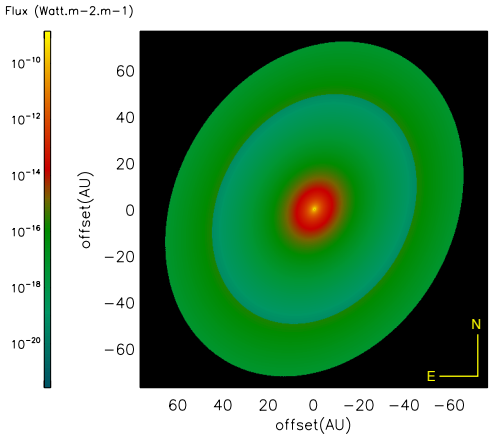

FIGURE 5.5: The synthetic image of MWC480 at λ=10 μm for the two-components disk model.

Since the two components of the disk are attached, then the outer radius of the first component is equal to the inner radius of the second component. To minimize our free parameters, we also keep the best value of the inner radius of the disk we found for the one-component disk model $r_{in} = 0.27AU$, which is comparable to the one obtained by Eisner et al. (2009) for the dust sublimation radius. Since in the one-component disk model, the maximum grain size of 200 μm is more consistent with the SED, we keep this value for the two- component disk model.

We explored all remaining free parameters to find the best model corresponding to our data. In Table 5.3, we summarize the best parameters. In Fig. 5.5, we show the synthetic image of this model. In Fig. 5.6, we represent the SED, the Keck and the MIDI visibilities for a maximum grain size of 200 μm.

In this model, we use the same method we used for the one-component disk model to find the reduced χ^2.

In Table 5.3, we show the reduced χ^2 for the two-component disk model.

5.4.2.1 Results

The two-component disk model could reproduce the deficit of the emission at wavelengths from 10-200 μm and the Keck and the 2007 MIDI visibilities. Although, at 10 μm still we have a minor deficit of the flux compared to the observations. Decreasing the inner radius of the second component less than 52 AU was not consistent with the

SED and visibilities.

One thing we should emphasize here is that the total dust mass, dominated by the second component, is about 1000 times smaller than the dust mass derived from continuum millimeter measurements. Mannings and Sargent (1997) using millimeter observations, found a dust mass of $2.4\times\ 10^{-4}$–$2.9\times\ 10^{-4}\ M_{\odot}$, whereas the dust disk mass derived in our study is $1.25\times\ 10^{-7}\ M_{\odot}$ only. Studying MWC480 in the millimeter wavelengths were done through continuum emittion of an optically thin medium (Mannings and Sargent, 1997). By observing an optically thin medium, it is possible to have a direct and real measure of the dust mass because we have access whole disk emission. We plot in Fig. 5.7, the vertical optical depth at 10 μm versus the distance from the central star for the two-component disk model. According to Fig. 5.7, since the optical depth of the first component is less than 1, then the value obtained for the mass of the dust is a real estimate of the total amount of the dust in this component. The optical depth of the second component of the disk is greater than 1. Increasing the mass of the dust for the second component more than $1.25\times\ 10^{-7}\ M_{\odot}$, which would contribute to the total dust mass, does not change the SED and the visibilities. The best value found for the dust mass of the second component in our model, indeed, is the minimum mass required for the dust for this component. It is thus possible to have more dust in the second component as well. .

We suspect that the disk around MWC480 may be a pre-transitional disk and the inner parts are (almost) depleted of material. Fig. 5.8 shows that there is a discontinuity in the transition between the two components of the disk of MWC480 in the surface density from 4×10^{-7} to $1.5 \times 10^{-3} kg/m^3$. In this figure, we compare the surface density of MWC 480 with the MMSN and the surface density of the pre-transitional disk of HD 100546. We wanted to only show a comparison between the jump in the surface density of MWC 480 and HD 100546 as a pre-transitional disk. Sitko (1981) noted that the energy distribution of MWC 480 is similar to that of classical Ae Herbig stars (e.g., AB Aur), except for the 9.7 μm silicate feature in the spectrum of MWC 480 being slightly weaker. This may be related to starting depleting the dust in Mid-Infrared emission region.

Tatulli et al. (2011) show the surface density jump between the two components of the disk of HD 100546 is an order of $\sim 10^{-4}$. However, the second component of HD 100546 considering the gap is located at 13 AU and the one MWC480 without gap is at 52 AU.

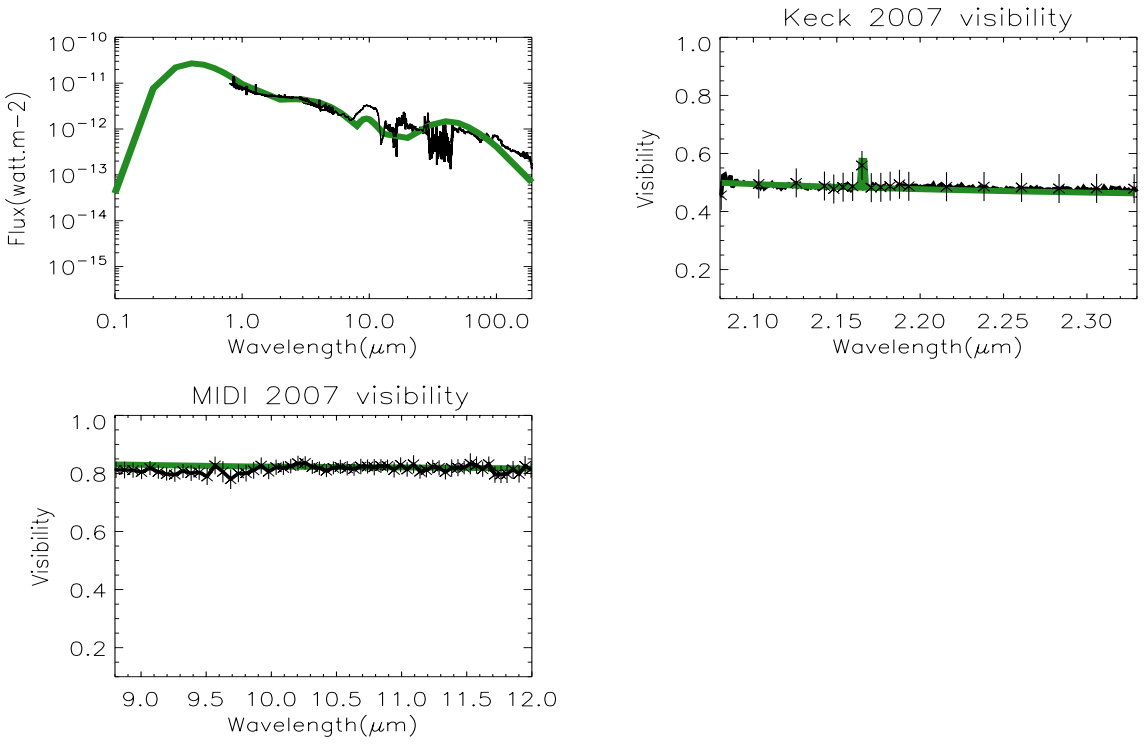

FIGURE 5.6: Two-component disk model for the maximum grain size of 200 μm. The black solid lines in plots represents the observational data. For the SED, SpeX and BASS data for 0.8.-14 μm and ISO data in 1998 for 15–200 μm. MIDI uncorrelated spectrum between 8–13.5 μm.

In the case of MWC480, although the inner component compared to the second one has significantly lower mass, there is no dip in the infrared emission of the SED. However, Espaillat et al. (2012) figuring out the status of the disks around 14 stars, showed that the dip in the infrared emission of SED of e.g., LRLL 37 is not obvious and on the other hand a full disk could not reproduce its SED. So they conclude that this could be a sign that LRLL 37 is a pre-transitional disk with a small gap that contains some small optically thin dust in the inner component.

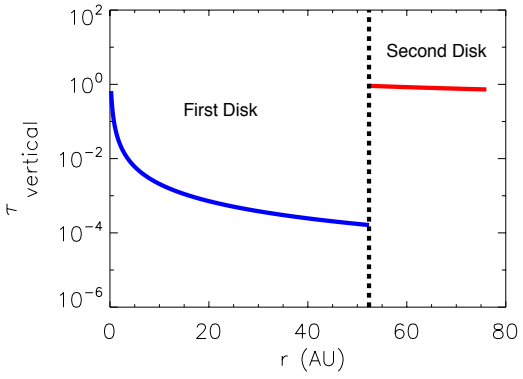

FIGURE 5.7: The vertical optical depth at wavelengths 10 μm versus the radius for the two-components disk model. The dashed line shows the transition between the two components.

We may assume that in the inner component the dust dissipation has started.

According to Table 5.3, the value of the reduced χ^2 for the two component disk models is smaller than the one for one component disk model. Therefore, the two-component disk model can better reproduce our data than one-component disk one.

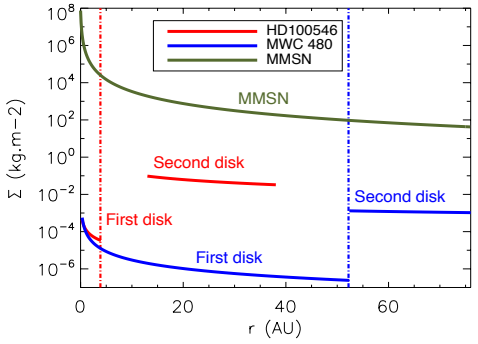

FIGURE 5.8: The surface density at wavelength 10 μm versus the radius for the two-components disk model. The dashed line shows the transition between the two components.

The only quantity that makes a difference between the two models is the SED especially at longer wavelengths.

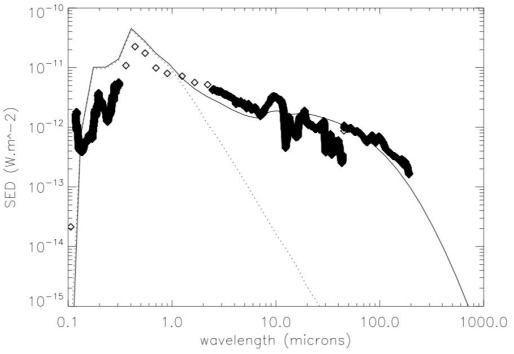

FIGURE 5.9: The plot of SED for a two-layer disk model including a mid-plane component. The bolded black line is observed data and thin black line is the best model.

5.5 Summary and perspectives

Using observations based on stellar interferometry in the mid-IR, we were able to resolve the circumstellar emission around the Herbig star MWC480. We performed a coherent modeling reproducing the SED and the visibility simultaneously. The modeling is based on a semi-analytical approach using a temperature and surface density-gradient laws. Our aim is to constrain the overall spatial structure of the inner disk region and explore the possible multi-component structure of the disk to better understand the condition of

disk structure in the inner region. In addition, we tried to use three different maximum grain sizes in a size distribution assumed to be of interstellar dust comprising silicate, probably amorphous and graphite composition (Laor and Draine, 1993). The maximum grain size of 200 μm assumed in the distribution was more consistent with the SED of the star. We conclude that:

- A two-component disk model could reproduce better the SED, the Keck and the MIDI visibilities simultaneously. In the one-component disk model, increasing the near-IR emission by exploring all free parameters was not consistent with the SED in the longer wavelengths. In fact, the second component of the disk mostly contributes to the emission at longer wavelengths. Then, the second disk component in our modeling is necessary to reproduce all our measurements simultaneously.

- We suspect that the disk around MWC480 may be a pre-transitional disk since the inner parts are (almost) depleted of material. The surface density distribution of MWC480 shows a jump in the transition between the two disk components, which is seen between disk components of many pre-transitional and transitional disks around Herbig stars. In the SED in the mid-IR wavelengths of MWC480 there is no significant dip. However, the dip in the infrared emission of e.g., LRLL 37 is not obvious, although the disk around this star is considered as a pre-transitional disk.

  We tested a two-component disk model with an outer disk with the aim to reproduce the far infrared and milimeter wavelength contributions to the SED. This cold (less than 100 K) outer disk component has an inner rim located at 52 AU corresponding to an angular size of 0.37 arcsec. It does not contribute to the K band and N band visibilities and therefore has no impact on our results based on the visibility modelling. However our conclusions on the possible pre- transitional nature of the MWC 480 disk (inner disk depleted in dust relative to the outer disk), see Fig. 5.8, which are based on this two-component disk model, should be taken with caution. Indeed, an alternative approach to reproducing the far infrared and milimeter contributions to the SED is to consider the disk mid- plane emission. As shown e.g. by Chiang Goldreich (1997), the cold midplane of the disk can be the source of the far infrared and milimeter emission. We have tested this possibility for MWC 480 by using a radiative transfer simulation based on the RADMC3D code (Dullemond Dominik, 2004). The far infrared and milimeter contributions of the SED (see Fig. 5.3) could be correctly reproduced by a two-layer disk model including a mid-plane component that contains 95 percents of the total dust disk mass that is comparable with our analytical model, which has 99 percent of its

mass in the outer disk (see Fig. 5.9). However, using two-layer disk model the near IR flux could not be well-reproduced.

- Many authors showed that MWC480 presents a time variability in the SED in the near-IR and mid-IR wavelengths. In this paper, first, we show that the total flux of the MIDI observations in 2007 is almost consistent with the BASS data in 2007 in N band. Figuring out the effect of time variability of the star MWC480 in the near-IR in our models, we found that the maximum or minimum brightness state affects on visibilities, especially the Keck ones. The effect on the SED is significant only for wavelengths 2–20 μm. For the maximum brightness state in the near-IR, the value of the Keck visibilities is less than for the minimum state. For MIDI visibilities, this variability in brightness in the near-IR is less significant. However, for the minimum brightness state, the disk in the mid-IR is more resolved than for the minimum state. Since variability of the star in the near-IR affects the visibilities, it is very important to use the data, which are taken at the same time as intereferometric observations.

- We are far from being able to claim that we fully understand the inner disk around the MWC480. For a better understanding of its system, it is crucial to repeat observations at near and mid-IR wavelengths. The MIDI observations have been obtained with only one configuration and one orientation.

Chapter 6

The possible asymmetrical models for explaining the inner disk structure of MWC480

6.1 Abstract

Studying the physical conditions structuring the young circumstellar disks is required for understanding the onset of planet formation. Of particular interest is the protoplanetary disk surrounding the Herbig star MWC480, which was discussed in Chapter. 5.

New observations are driving our study, in particular some recent Very Large Telescope Interferometer (VLTI)/MIDI data acquired in December 2013. Our two-component disks model could not reproduce simultaneously all our data : the Spectral Energy Distribution, the near-infrared Keck Interferometer data and the mid-infrared data obtained with the MIDI instrument. In order to explain all measurements and assuming that the structure of the disk of MWC480 has not varied with time, one possibility is to add an asymmetry in our two-component disks model. Several scenarios are tested, the one considering the presence of an azimuthal bright feature in the inner component of the disk model, provides a good fit of the data. However, other possibilities of the centro-symmetrical models may also reproduce our MIDI data as well.

TABLE 6.1: Log of long baseline interferometry observations. Our recent MIDI/VLTI observations with ATs (P.I.: Ratzka 2013) were conduced in December 2013. Past observations were made also with the MIDI instrument (P.I.: Di Folco) and with the Keck Interferometer (Eisner et al., 2009).

Instrument	**Date**	**Telescopes & Baselines**	B_p **[m]**	**P.A.** [°]
MIDI	2007–02–04	UTs: UT2-UT3	42.8	52°
KI/V2	2007–07–03	Keck1-Keck2	84.9	48°
MIDI	2013–12–29	ATs: K0-J3	28.6	330°

6.2 Introduction

To introduce the Herbig star MWC 480, I refer the reader to the Sect. 5.2 of Chapter. 5. Stellar interferometry is a key observational technique for the study of the inner region of the protoplanetary disks. It provides an angular resolution level of a few milliarcseconds that translates into sub-AU scales at the distance of MWC 480. Near- and mid-infrared emission originating inside 20 AU was probed by the Keck Interferometer (Eisner et al., 2009) and by our observations performed with the MIDI instrument at the VLTI. The two instruments are complementary in terms of spectral coverage and spectral resolution.

The previous axisymmetric models of MWC480 were sufficient to explain the existing observations acquired before December 2013 (Jamialahmadi et al., 2014) (see. Chapter. 5). However, considering the recent VLTI/MIDI observations of December 2013, taken at a perpendicular baseline compared to the previous ones, two-components disk model could not reproduce all the measurements. Several scenarios have been tested. One possibility to explain all data is, adding another component as an azimuthal asymmetry to the inner component of the disk assuming that the structure of the disk of MWC480 has not varied during two MIDI observations in 2007 and 2013. However, the centro-symmetrical models are not excluded yet by our work on this star since it is impossible to achieve this based on just few Interferometric measurements and without phase information. Azimuthal asymmetries in the brightness maps could be generated by a stellar companion, a wall-like emissive surface at the inner edge of the disk (Hashimoto et al., 2011), dust trapping in a vortex (Barge and Viton, 2004), a disk warping (Flaherty and Muzerolle, 2010), or even a spiral wave (Kraus et al., 2013). In this Chapter, Section 6.3 sammarizes the observations and the data processing. Section 6.4 describes our semi-analytical models and the related results. Section 6.5 includes a discussion on the modeling results and Section 6.6 summarizes our work and outlines some observational perspectives to validate the existence of azimuthal asymmetries in the disk.

6.3 Observations

6.3.1 MIDI observations

MWC480 has been observed in 2007 and in 2013 with the instrument MIDI of the VLTI (Leinert et al., 2003) of the ESO Paranal Observatory. The first observation was carried out on the 4th of February 2007 using two 8 m Unit Telescopes (UTs). The second observation was made on the 29th of December 2013 using two 1.8 m Auxiliary Telescopes (ATs). To explain the detailed observations and data reduction method, I refer the reader to Sect. 5.3 of Chapter 5. A summary of the observing log, containing the length of the projected baselines is shown in Table 6.1. The UV coverage of all the interferometric observations is shown in Fig. 6.1.

In order to calibrate the visibilities of the science source, we used the calibration star HD 50778 in 2013. This calibrator was selected from the SearchCal JMMC [1] tool.

As we can see in Fig. 6.1, representing the MIDI visibility in 2007, the source is close to being unresolved with a visibility level of 0.8. Furthermore, the visibility curve looks flat. In contrast, the MIDI visibility with a shorter baseline obtained in 2013 is roughly 0.7 for the wavelengths 8.7–10 μm, but for the wavelengths of 10–12 μm the source is more resolved and the visibility curve does exhibit a progressive drop-off down to 0.3. For the two different baseline orientations, which are almost perpendicular, these differences in the MIDI visibilities could be due to an asymmetry in the disk around the star.

As we showed in Chapter 5, MWC480 also was observed with the Keck Interferometer in the K band in the wavelengths range 2.08–2.33 μm (Eisner et al., 2009).

6.3.2 Spectroscopic observations with SpeX

We observed MWC 480 with the SpeX spectrograph on IRTF in parallel to the recent MIDI observations. The SpeX observations were made on 11th September 2013 using the cross-dispersed (hereafter XD) echelle gratings in both short-wavelength mode (SXD) covering 0.8–2.4 μm and long-wavelength mode (LXD) covering 2.3-5.4 μm (Rayner et al., 2009). The data were reduced using the Spextool software (Vacca et al., 2003; Cushing et al., 2004). Existing Spex data from 2007 by Sitko et al. (2007), second data set to cover the epoch of the first MIDI measurement.

We obtained the uncorrelated flux for each MIDI observations in 2007 and 2013. According to Fig. 6.1, the total flux obtained by the MIDI observations in 2007 and 2013

[1] http://www.mariotti.fr/

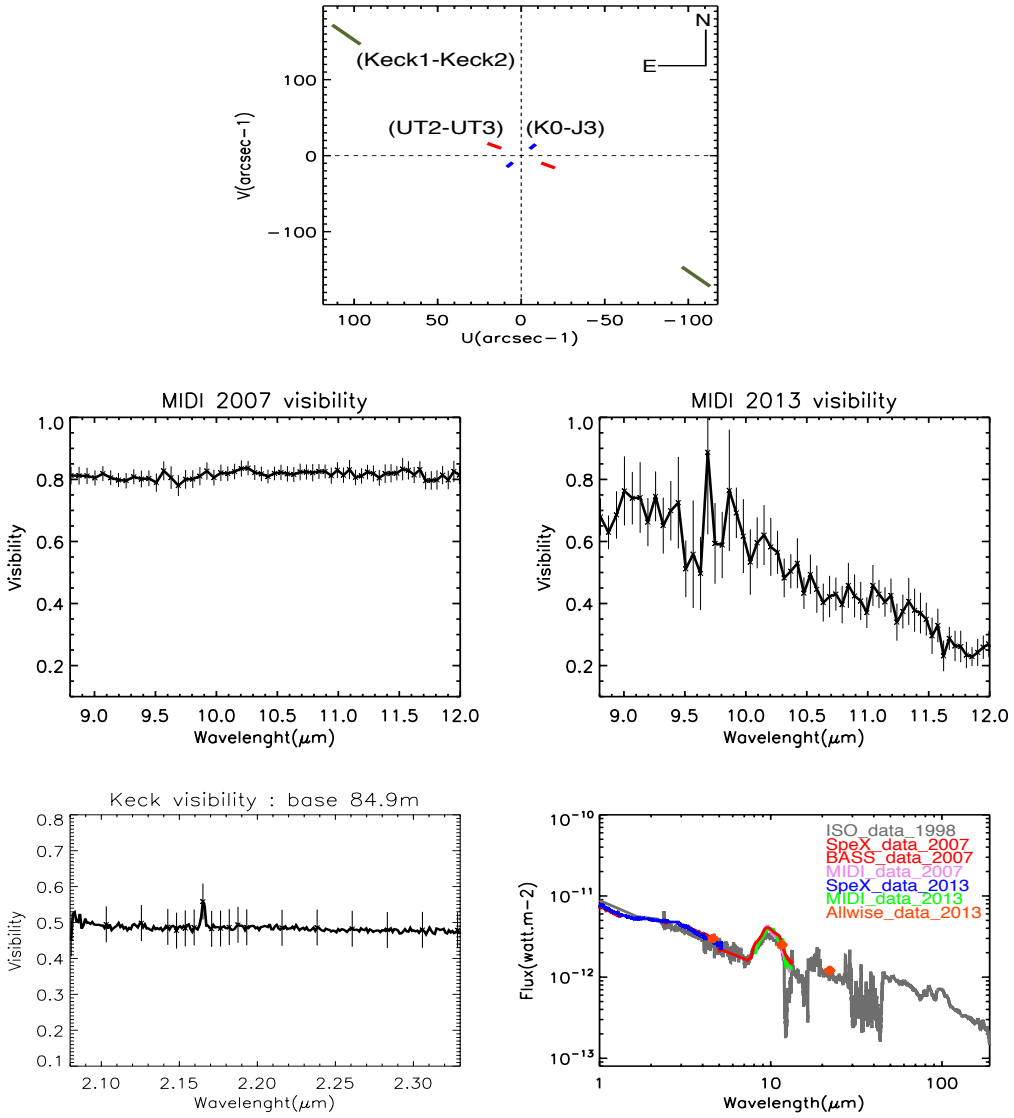

FIGURE 6.1: **Top**: UV coverage for the three sets Interferometric observations. **Middle-left**: Measured N-band visibility of MWC480 as a function of wavelength in 2007 with spectral resolution of R=30. **Middle-right**: Measured N-band visibility of MWC480 as a function of wavelength in 2013 with spectral resolution of R=30. **Bottom-left**: Measured K-band visibility of MWC 480 (the error bars are represented for a few points only). **Bottom-right**: ISO data for wavelengths 2.3–198 μm in 1998 (gray color), SpeX data and BASS data for wavelengths 0.8–5.4 μm and 5.5–14 μm in 2007 (red color), SpeX data for wavelengths 0.8–5.4 μm in 2013 (blue color), BASS data for wavelengths 5.5–14 μm in 2011 (blue color), Allwise photometric data in 2013 for the three 4.15, 11.5, 22 μm (orange red circle), the MIDI total flux for wavelengths 8–13.5 μm in 2007 (pink color) and in 2013 (green color).

are similar. The BASS data in 2007 and 2013 are similar to the flux of MIDI data obtained in 2007 and 2013 as well. In our previous study of MWC480, we figured out the effect of variability on our model (see. Jamialahmadi et al., 2014). Although MWC480 is variable in near and mid-IR wavelengths according to previous studies, we obtained nearly the same flux from 2007 and 2013 SpeX, BASS and MIDI observational data (see. Fig. 6.1).

6.4 Modeling

To interpret in a consistent approach all our observations, we use the same model introduced in Chapter 5 (Jamialahmadi et al., 2014).

A previous study (Jamialahmadi et al., 2014) (see. Chapter. 5), based on data not including the recent 2013 MIDI visibility, has shown that a cylindrically symmetrical disk model could explain consistently the SED, the Keck and the 2007 MIDI visibilities simultaneously for the maximum grain size of 200 μm. Such a symmetrical model could be comprised of a two-component disk with an inner optically thin disk compared to the outer disk (See Fig. 5.6 of Chapter 5). I showed that a two-layer disk using a radiative transfer code could also reproduce the Keck and the MIDI visibilities and the SED for loner wavelengths. However, in this model the SED for the near-IR wavelengths could not well reproduced. A two-component disk model appeared not to be anymore consistent when taking into account the 2013 MIDI visibility (See Fig. 6.2). I explored the free parameters of two-components disk model adding 2013 MIDI data. However, there was not significant changes compared to the best values I obtained for previous data. Therefore, I kept unchanged the best parameters I found for two-components disk model for previous data. In Table 6.2, I show the best set of parameters I could identify for this model, which although not providing a fit of the 2013 visibility, reproduce all the other data. The reduced χ^2 for this model is of 7.45. It is of interest to underline that the flatness of the 2007 Keck and MIDI visibilities were mostly constraining the flux ratio between a non-resolved disk component and an extended one, the second disk component itself. Indeed the second disk component with its inner rim at 52 AU (See Table 6.2) is fully resolved at the Keck and MIDI resolution. In this model we fixed the inclination and the position angle of the disk to the value of i=37° and 57° respectively (See. Chapter 5).

Taking into account the 2013 data, any attempt for a model adjustment with different inner radius of the outer disk has failed. In Fig. 6.3, I plot the SED and visibilities for different values of the inner radius of the outer disk. It can be noted that the 2013 MIDI

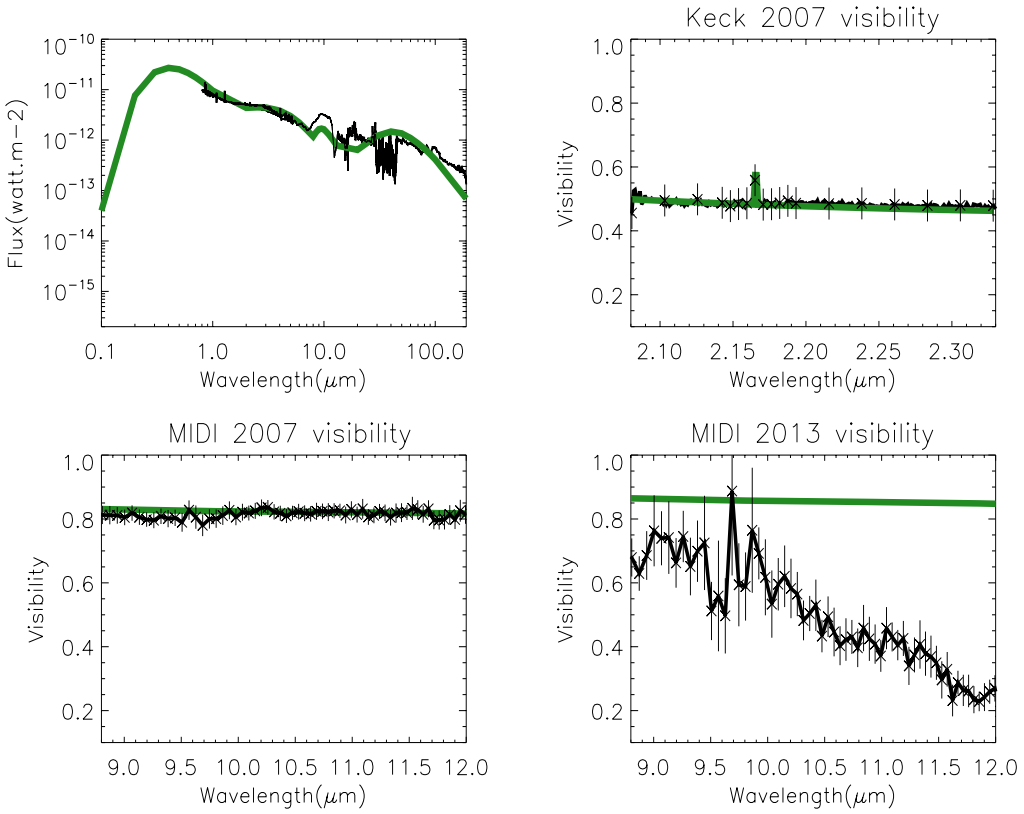

FIGURE 6.2: The two-component disk model for a maximum grain size of 200 μm. See caption of Fig. 5.6 of Chapter 5.

TABLE 6.2: The best parameters and their explored range for the two-component disk model for a maximum grain size of 200 μm.

First disk component			**Second disk component**		
Parameters	**Explored Ranges**	**Best-Values**	**Parameters**	**Explored Ranges**	**Best-Values**
M_{dust}	10^{-12}...10^{-7} $M_{\odot}$	0.9×10^{-10} $M_{\odot}$	M_{dust}	10^{-12}...10^{-7} $M_{\odot}$	1.25×10^{-7} $M_{\odot}$
p	0.1...1.98	1.5	**p**	0.1...1.98	0.6
q	0.4...0.9	0.5	**q**	0.4...0.9	0.5
r_{in}	0.4...0.9 AU	0.27 AU	r_{in}	1...60 AU	52 AU

visibility is bringing strong constraints on the 'green line' tentative model since the slope on the visibility holds information on the inner rim size of the second disk component.

Inclination of the disk itself can produce natural asymmetry in the data. In Fig. 6.5, I plot the inclined disk models from an inclination of zero degree to one close to 90 degrees. Inclination significantly changes the SED, the Keck and the MIDI 2007 visibilities but it does not affect the MIDI 2013 visibility. Since all attempts of modeling with two-components disk or natural asymmetrical models such as inclined disk models were unsuccessful, one additional component in the disk, generating an asymmetry in its brightness maps is included in our study. However, other possibilities of centro-symmetrical models may can reproduce our data. I consider that this component could

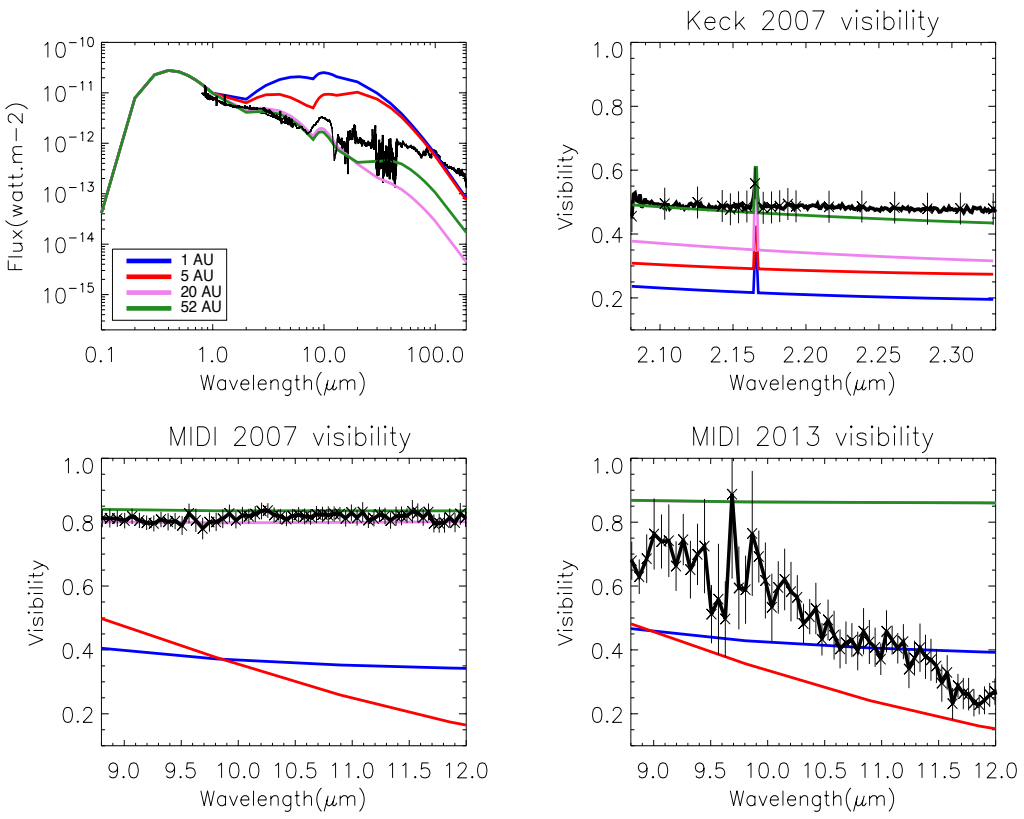

FIGURE 6.3: The effect of varying the inner radius of the outer disk on the SED and the visibilities. We assume an outer radius of the outer disk of 60 AU to speed up our running computing time.

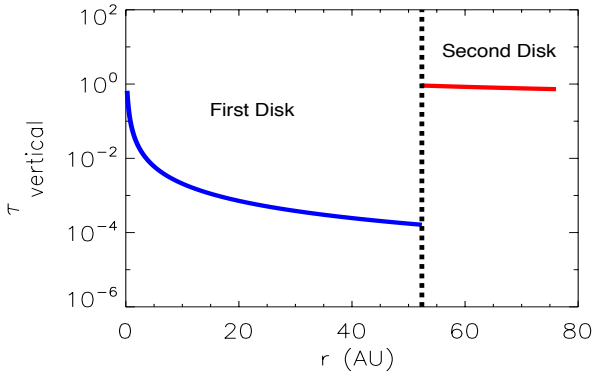

FIGURE 6.4: The vertical optical depth at 10 μm of wavelength versus the radius for the two-components disk model. The dashed line shows the transition between the two components.

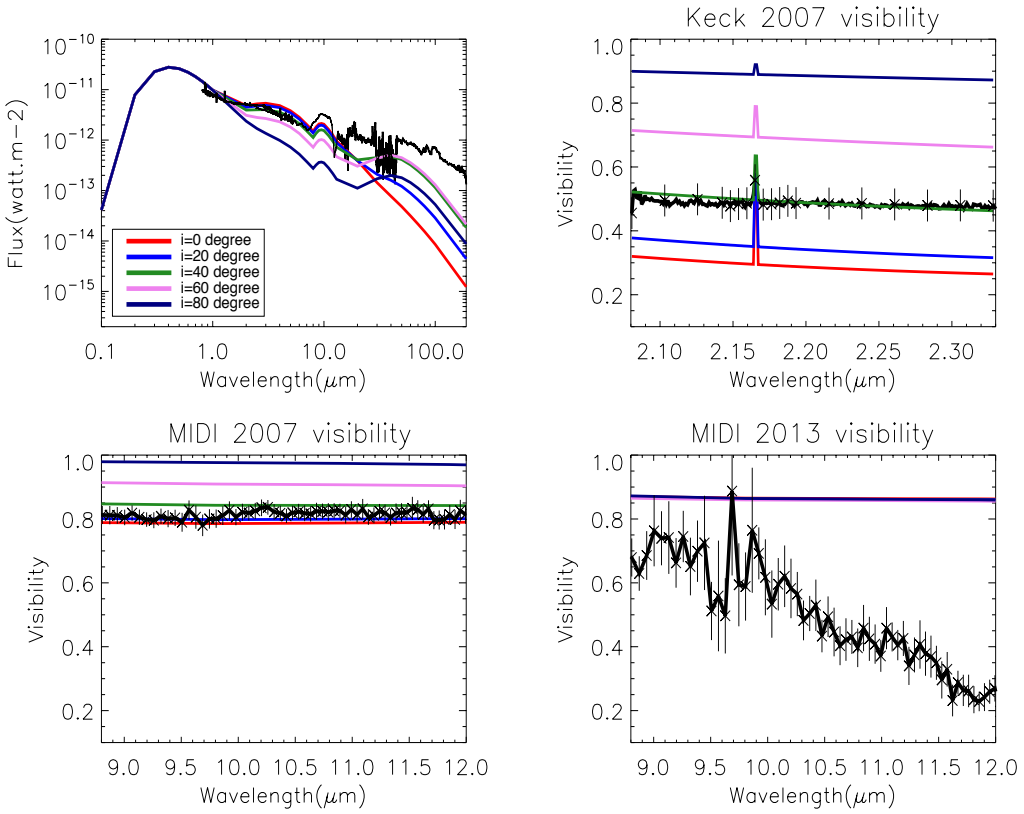

FIGURE 6.5: The effect of varying the inclination on the SED and the visibilities.

be a wall-like structure generated by the inner edge of the outer disk or a clump-like structure located in the optically thin inner disk.

6.4.1 Azimuthally asymmetric models

Two-components disk model could not reproduce the SED, the Keck and the MIDI visibilities simultaneously. Even inclined disk models with fix P.A. can not match our data. For this reason, I consider in the following, two situations that produce possible azimuthal asymmetries in the disk. In the two components of the disk model, we include:

- An atmosphere height increase at the interface between the two disks, which is producing a crescent shape aspect when the disk is inclined.

or

- A clump of dust in the inner disk, that increases its optical depth, enhances locally the disk brightness.

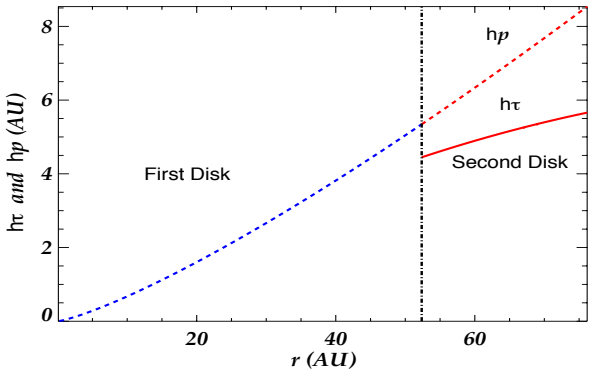

FIGURE 6.6: Structure of the two-component disk model with a wall: disk atmosphere height (solid line) and pressure scale height (dashed line). The atmosphere height is not defined for the first disk component since this component is optically thin.

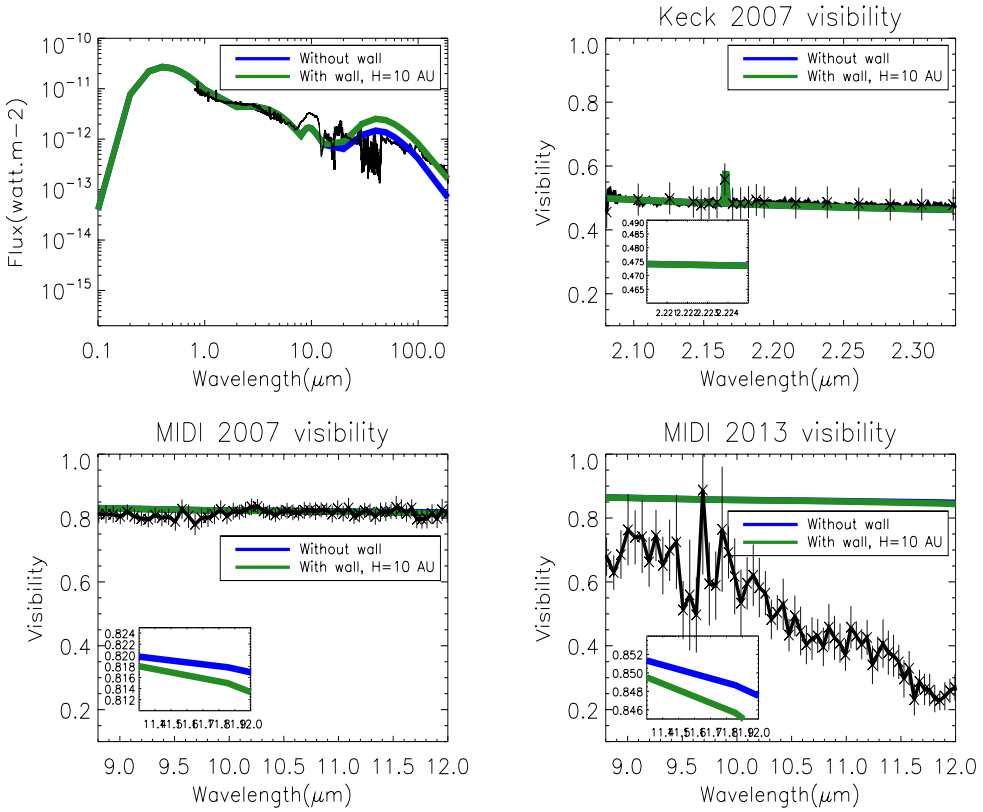

FIGURE 6.7: Two-component disk model with a wall. The black solid lines in the plots represents the observational data. See caption of Fig. 5.6 of Chapter 5.

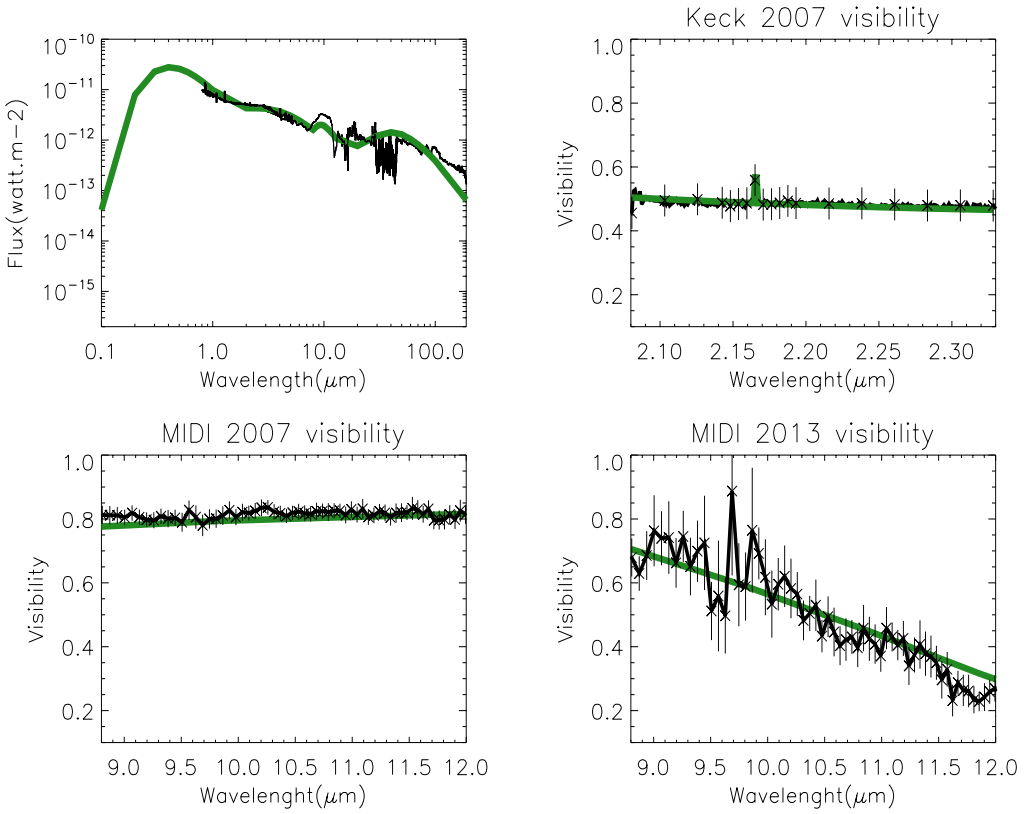

FIGURE 6.8: Two-component disk model with clump. The black solid lines in the plots represents the observational data. See caption of Fig. 5.6 of Chapter 5.

6.4.1.1 Two-component disk model with wall

A wall effect is generated at the inner edge of the second disk component due to a sudden optical depth variation between the first component and the second component of the disk. The inner disk edge of the second disk component is illuminated directly by the central star. In Fig. 6.6, we represent how h_p(r), the pressure scale height, and h_τ(r), the atmosphere height vary with the distance from the central star. A sharp transition of the surface density exist between the two disk components. Because of this transition, a difference in the atmosphere scale height at the junction of the two disks is expected. This difference in height produces a wall-like effect. In Sect. 1.3.2 of Chapter. 1, we detail the derivation of the atmosphere scale height. From this derivation, we find an atmosphere scale height of $\sim$ 5 AU at the junction between the two disk components, i.e., 52 AU.

If the disk is inclined, the observer sees this wall as a crescent shape, which makes an azimuthal asymmetry in the disk brightness map. Some authors have figured out the effect of such a wall in their model. For instance (Hashimoto et al., 2011) consider an asymmetrical structure in the inner edge of the disk around the Herbig star AB Aur.

TABLE 6.3: The best parameters and their explored ranges for the two-component disk model with clump for the maximum grain size of 200 μm. The quality of the model fitting gives a $\chi^2_{r\ total}$ for this model of 5.72

Parameters	**Best-Values**	**Explored Ranges**
d_{Cl}	6.5 AU	1–10 AU
r_{Cl}	0.8 AU	0.1–2 AU

The wall would emit a black body radiation according to

$$dF_{\lambda,wall} = B_\lambda\left[T_w(r_w)\right]\left[1 - exp\left(-\frac{\tau_\lambda(r_w)}{cos(i)}\right)\right]\left(\frac{ds_w}{D^2}\right), \tag{6.1}$$

where r_w is equal to inner radius of the outer disk component and T_w is calculated directly from Eq. (5.21) at r_w.

The inclination of the disk, i, has the effect to produce a crescent shape and to increase the apparent optical vertical depth $\tau_\lambda(r_w)$ for the observer. According to Fig. 6.4, the vertical optical depth at the inner edge of the second disk component is about 1 for a face on disk increases as 1/cos(i). We use the best explored parameters obtained for two-components disk model in Jamialahmadi et al. (2014) and summarized in Table 6.2. The 2 additional parameters that are related to the wall, i.e., $h_\tau(r_w)$, $T_w(r_w)$ are derived from Eq. 1.13 and Eq. 6.1 respectively. In Fig. 6.7, we present the SED, the Keck and the MIDI visibilities, while the synthetic image of this model is shown in Fig. 6.9.

Due to the disk inclination, the wall is seen as a crescent shape but not much contrasted, which produces as expected an azimuthal asymmetry in the image. However, as shown in Fig. 6.7, this did not allow to reproduce all our measurements simultaneously, especially the difference in slope and visibility level for the two MIDI measurements.

6.4.1.2 A two-component disk model with a bright feature

As I mentioned before, the inclusion of a bright feature along the direction of the 2013 baseline could produce an asymmetry that could explain the data. This feature could be a companion or a local dust concentration in a clump. I test here a clump of dust that may produce a significant effect in the modeled visibilities. The clump emission is modeled considering an optically thick clump and a black body emission $B_\lambda[T_{Cl}(d_{Cl})]$, where T_{Cl} is the temperature of the clump and d_{Cl} is the distance of the clump from the central star. For each surface area element of the clump, the observer receives

$$dF_{\lambda,clump} = B_\lambda\left[T_{Cl}(d_{Cl})\right]\left(\frac{ds_{Cl}}{D^2}\right). \tag{6.2}$$

In this model, we set the parameters obtained for the best two-components disk model of Jamialahmadi et al. (2014). We add 4 additional parameters, which are related to the clump:

- the P.A. of the clump,
- the distance of the clump from the central star (d_{Cl}),
- the mass of the clump,
- the radius of the clump (r_{Cl}).

The P.A. of this clump is set to the P.A. of the baseline used in 2013, i.e. 330° (see Table 6.1). Assuming that the clump is optically thick maximizes the contrast if the optically thick clump is located in the first optically thin disk component. Consequently, the parameters are limited to:

- the distance of the clump from the central star (d_{Cl}),
- the radius of the clump (r_{Cl}).

The distance d_{Cl} constrains the temperature of the clump from Eq. 6.1.

I present in Table 6.3, the best-fit values obtained for the two clump parameters, as well as the reduced χ^2. Fig. 6.8 presents the corresponding best-fit SED as well as the best-fit Keck and MIDI visibilities. The synthetic image for this best-fit model is shown in Fig. 6.9.

By offering more degree of freedom in the model, it appears that the inclusion of a dust clump, in the inner region of the two-component disk model is a possibility to reproduce the SED, the Keck and the MIDI visibilities simultaneously. As shown in Table 6.3, my best-fit solution of the two-component disk model with a clump gives the smallest total reduced χ^2 among all the models I considered.

6.5 Discussion

One possibility to reproduce the SED and the near-IR and mid-IR interferometric data of MWC 480 could be the existence of an asymmetric disk structure. However, I am aware that with few interferometric measurements and no phase information is not

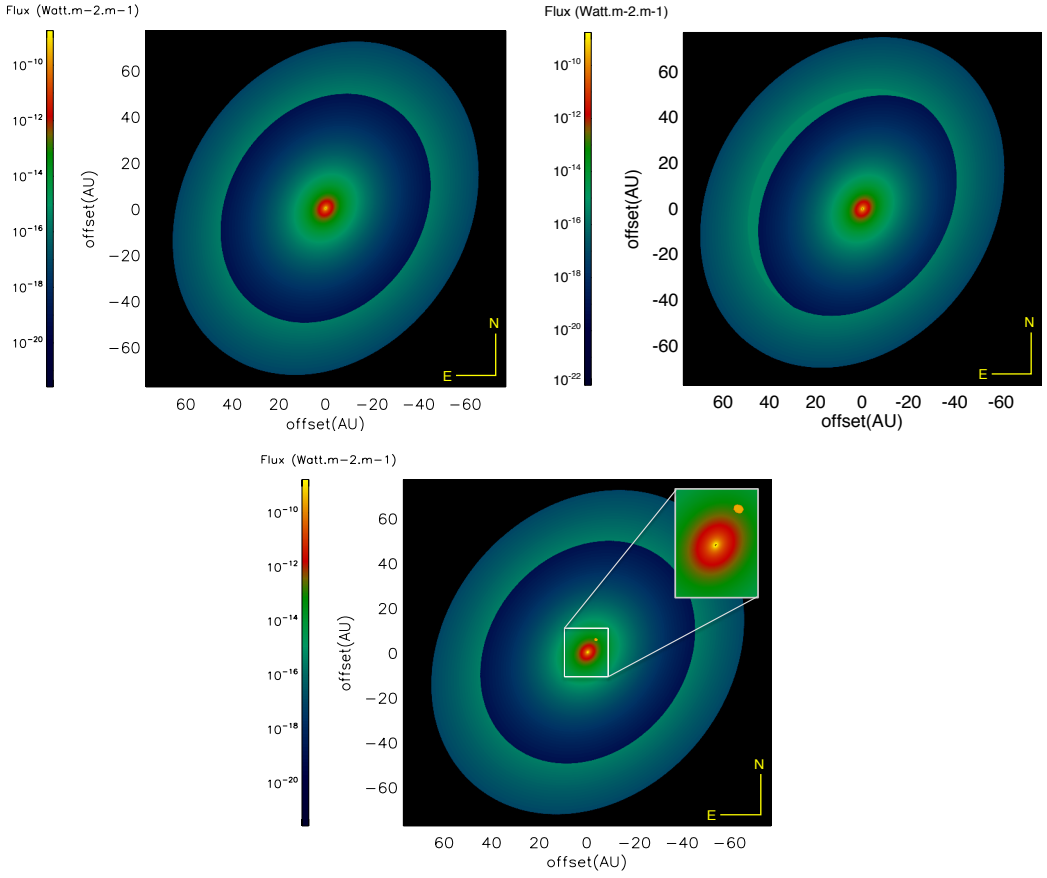

FIGURE 6.9: The synthetic image of MWC480 at λ=10 μm. Top-Left: Two-component disk model, Top-Right: Two-component disk model with wall, Bottom: Two-component disk model with clump.

possible to fully exclude centro-symmetrical models. For instance, two clumps with the star in between could have worked also to fit the data and would have preserved the centro-symmetry of the model.

If the bright feature is a clump of dust and If the clump has rotated, knowing the period of its movement is of importance. With a location of the clump found to be at 6.5 AU from the central star, and knowing the mass of the star $M_\star$=1.8 $M_\odot$ (Simon et al., 2000), the orbital period of this bright feature can be estimated to $\sim$ 7 yrs. This 7 yrs is also the time interval between the two MIDI observations.

The brightness ratio between the clump and its surrounding is nearly 2×10^3. The clump optical depth is about 1 while the disk optical depth is of the order of 4 $\times$ 10^{-3} at 10 μm and varies from 2 $\times$ 10^{-3} to 3 $\times$ 10^{-3} in the range 8-13 μm.

A binary star can also cause an asymmetry in the disk. I tested this possibility with my models. In order to resolve the disk in the direction corresponding the baseline orientation in 2013 and to decrease the visibility down to 0.3, I need a companion that

is bright enough in the N band. However, a stellar companion can be excluded due to the SED. Only a clump is cool enough to contribute mainly at mid-infrared and at longer wavelengths, i.e. without increasing the near-infrared flux significantly. A disk warping and spiral waves can make asymmetries in the disk as well. For instance, a disk warping was used by Kraus et al. (2013) to explain the asymmetries in the inner disk of the star V1247 Orionis. In this chapter, I did not figure out the effect of disk warping and spiral waves. I have plan to test these effects in the disk of MWC 480 as well.

6.6 Summary and perspectives

Using spectro-interferometry, I was able to resolve the circumstellar emission around the Herbig star MWC480. I performed a coherent modeling that aimed at reproducing the broadband SED, and the Keck and MIDI interferometric data. The modeling is based on a semi-analytical approach using a temperature and surface density-gradient two-component disk. My aim is to constrain the overall spatial structure of the inner disk region and explore the possible multi-component structure of the disk to better understand the conditions of planet formation in the inner region. In order to explain the existing measurements, I show that an azimuthal feature is one possibility to explain the data. I concluded that:

- Two-components disk model is not consistent with new MIDI data in 2013 in spite of exploring parameters.
- A two-component disk model with a wall-like emission at the inner rim of the outer component, generated by a jump in the surface density at the interface between the two components, could not reproduce all our measurements.
- A better agreement with all our data was finally obtained considering a bright feature such as a clump-like asymmetry in the inner component of the two-component disk model. I found that this putative clump could be located at 6.5 AU.

Chapter 7

Conclusion and future work

In my thesis, I study the circumstellar environments surrounding YSOs based on high resolution interferometric observations. My goal is to improve our understanding of the structure and the evolution of the circumstellar disks by determining their density distribution, their temperature distribution, the size and composition of the dust components and finally the kinematic of the gas. I have developed my thesis following three complementary wavelength domains: study of the photosphere of the star and its nearby gaseous disk through visible interferometry (Chapter 3), study of the radial and vertical structure of the inner rim of a pre-transitional disk at fractions of AU through near-IR interferometry (Chapter 4), and the characterization of the disk regions at fractions of AU and few AUs from the central star through spectroscopic and mid-IR interferometry (Chapter 5 and 6).

To analyze the observations, I have used several types of models and numerical tools: I used the LITpro2 model-fitting software developed by the Jean-Marie Mariotti Center (JMMC) to interpret the visible interferometric data in the continuum. To interpret the visible interferometric data in spectral lines, I used a kinematic model of an expanding and/or rotating thin equatorial disk. This model has been previously used for some classical Be stars and described in detail by Delaa et al. (2011). I successfully used a Monte-carlo radiative transfer code, called MCFOST, to model the dust in the inner structure of a pre-transitional disk and to interpret the near-IR interferometric data in the H band. I have developed a methodology to compute the interferometric observables from the MCFOST simulated images. I also developed a semi-analytical modeling tool. These semi-analytical models simulated the disk emission assuming different possible geometries and dust opacities and compared the model predictions with the data. With these models I interpret the near-IR and mid-IR observations.

7.1 The visible point of view

The analysis of visible interferometric observations of a young fast rotating star and its gaseous disk is described in Chapter 3. The environment of young stars is formed by a dusty and gaseous circumstellar disk in which the first stages of planet formation are thought to take place. The dynamics of the gaseous component, which dominates the total mass of the disk, control the accretion-ejection processes and will define the final architecture of forming planetary systems.

In Chapter 3, we studied **51 Oph**:

1) Stellar photosphere: in this study, we presented observations of 51 Oph with a spectro-interferometer operating at visible wavelengths, the VEGA instrument installed at the CHARA Array. This unique combination of spectrally and spatially resolved information allowed to resolve the photosphere of the star in the continuum. We derived, for the first time, the extension and flattening of 51 Oph photosphere. We found a major axis of θ_{eq}=8.08±0.70 $R_{\odot}$ and a minor axis of θ_{pol}=5.66±0.23 $R_{\odot}$. We used the LITpro2 model-fitting software to interpret our visible interferometric data in the continuum.

2) Spectrum: the VEGA spectrum of 51 Oph obtained during our observations exhibited an Hα emission line with a double-peak, which reflects the presence of the rotating circumstellar disk. The Hα profile wings clearly show that the disk is seen nearly edge-on.

Using spectro-interferometric measurements in the Hα line, we constrained the circumstellar environment geometry and kinematics and showed that the emission is produced in a 5.6 ± 2 $R_{\star}$ disk in Keplerian rotation. To do that, we used a simple kinematic model of an expanding and/or rotating thin equatorial disk, which is described in detail by Delaa et al. (2011).

7.2 The near- and mid-Infrared point of view

The analysis of near- and mid-IR interferometric observations are described in Chapter 4, 5 and 6. In these Chapters, I have focused my attention on two well known sources, HD 100546 and MWC 480.

- In Chapter 4, I studied the inner region of the planet-hosting, pre-transitional Herbig Ae/Be star **HD 100546** using PIONIER/VLTI at H band responsible to access the sub-AU scale from the central star, in which the accretion/ejection processes as well as planet formation are taking place. I have developed a model

based on a passive disk model using a 3D Monte-carlo radiative transfer code. We revisited the disk morphology and focused mostly on the inner rim of the inner disk to verify whether or not there is any asymmetry present in this region. I have used the radiative transfer code called MCFOST and I have developed some of the visualization tools to compute the interferometric observables, i.e., visibilities and closure phase.

We successfully reproduced with our model the SED (Spectral Energy Distribution) from the UV to the millimeter range simultaneously with the visibilities in the near-IR (NIR) but not the closure phase. The detection of non-zero closure phase at long baselines leads us to propose that the inner rim of the disk of HD 100546 might not be "smooth". The natural departure from centro-symmetrical disk models ,i.e., inclined disk models or the sharp inner rim edge of the disk could not explain the non-zero closure phase. We tested a hypothesis based on a clumpy structure in the inner rim. We could in this case successfully reproduce the closure phase, the visibilities and the SED simultaneously.

- In Chapters 5 and 6, I have studied **MWC 480**, a well studied peculiar Herbig Ae star. A variable emission line spectrum of the object was first described by Merrill et al. (1942). In Chapters 5 and 6, we investigated the inner structure and properties (e.g, temperature, mass) of the circumstellar dust disk of Herbig star MWC480 by near and mid-IR interferometry data and interpreted them using a consistent modeling reproducing the SED and the visibility simultaneously based on a semi-analytical approach using a temperature and surface density-gradient laws.

  Our aim was to constrain the overall spatial structure of the inner disk region and explore the possible multi-component structure of the disk to better understand the conditions of planet formation in the inner region.

  In Chapter 5, we presented a two-components disk model could better reproduce the SED and the Keck and the MIDI visibilities with one baseline. A one component disk model was not consistent with the SED in the longer wavelengths by exploring all free parameters. We suspected that the disk around MWC480 may be a pre-transitional disk since the inner parts are (almost) depleted of material. The surface density distribution of MWC480 showed a jump in the transition between the two disk components, which is seen between disk components of many pre-transitional and transitional disks around Herbig stars. Many authors showed that MWC480 presents a time variability in the SED in the near-IR and mid-IR wavelengths. In this Chapter, we modeled the variabilities assumed to be caused by the scale height of the inner disk modifying the exponent of the surface density

law, p for constant dust mass and inclination. We showed that the variability in the near-IR in the SED affects the near- and MIDI visibilities.

In Chapter 6, we showed that the best symmetrical two-component disk model of Chapter 5 appeared not to be anymore consistent when taking into account our new MIDI visibility, which was obtained in a perpendicular baseline orientation compared to the previous MIDI data. Even inclined disk models could not reproduce the two MIDI visibilities at once. One possible solution is to add additional component in the disk, generating an asymmetry in its brightness map. In this study, in the two-component disk model, we first included an atmosphere height increase at the interface between the two disks, which is producing a crescent shape aspect when the disk is inclined. A wall effect is generated at the inner edge of the second disk component due to the sudden optical depth variation between the first component and the second component of the disk. Due to the disk inclination, the wall is seen as a crescent shape but not much contrasted, which produces as expected an azimuthal asymmetry in the image. However, this did not allow us to reproduce all our measurements simultaneously, especially the difference in slope and visibility level for the two MIDI measurements. Another component that can produce asymmetry in the disk could be a bright feature in the inner disk with increased optical depth, which enhances locally the disk brightness.

The inclusion of a bright feature along the direction of the baseline of our new MIDI data could produce an asymmetry that could explain the data. This feature could be a companion or a local dust concentration in a clump. In Chapter 6, we tested that a clump of dust would produce a significant effects in the modeled visibilities. This clump appears brighter than its environment because the optical depth is less than one in the surrounding. This dust clump, in the inner region of the two-component disk model, allowed indeed to reproduce the SED, the Keck and the MIDI visibilities simultaneously. However, I am aware that with few interferometric measurements and no phase information is not possible to fully exclude centro-symmetrical models. For instance, two clumps with the star in between could have worked also to fit the data and would have preserved the centro-symmetry of the model.

7.3 Conclusions

In this thesis, I have demonstrated the power of interferometric technique to study the properties of the circumstellar gas and dust disks surrounding YSOs from visible to mid-IR spectral bands. Visible interferometric observations can probe the photosphere

of a resolved source in the continuum as well as the geometry and the kinematics of the gaseous disk producing the Hα line or Ca II triplet line on sub-AU scale. These observations allow us to derive the stellar parameters, e.g, diameter, mass, temperature and to constrain the extension of the emission line and to understand the physical process of the gas near the central star. Near-IR interferometric observations, probe the hot gas and dust distribution at a fraction of an AU from the central star and allow us to understand the kinematics of the gas and its physical processes responsible for the gas accretion on the star and the outflow mechanism, as well as hot dust properties and its physical mechanism for the disk evolution and the planet formation. Mid-IR interferometric observations mostly probe warm dust from the most inner region up to a few AU and allow to investigate the dust properties and their emission regime.

Because of limitations of the available interferometers from the visible to the mid-IR, direct observations of the inner gas and dust disk and study of the star itself have been limited so far to the bright objects. In my thesis, I worked on few YSOs, which were successfully observable with the current interferometers.

In the next section, I will discuss some ideas for future developments.

7.4 Future investigations

During my research, I faced some problems on either the modelling point of view, or the observational point of view. However, they never prompted me to give up my curiosity to better understand the initial condition of the planet formation. Instead, it raised many open questions in my mind that attracted my attention. For some ideas, I tried to write proposals to get observing time. However, a few of them are not carried out yet. In the following, I describe briefly some critical view either for modeling either for observations and the future developments aiming at improving the knowledge for each of object I studied in this thesis.

- I start with a peculiar object I studied in Chapter 3 using VEGA/CHARA observations at visible wavelengths. This object is called **51 Oph**. As I mentioned in Chapter 3, the evolutionary status of this star is not well-known yet. We concluded that from the visible point of view, 51 Oph presents all the features of a classical Be star: critical rotation, double-peaked Hα line in emission, and a circumstellar gas disk of a few stellar radii in Keplerian rotation.

  My future plan for 51 Oph is in the following:

  Understanding the origin and nature of the circumstellar disk orbiting 51 Oph is of importance.

Although from the visible point of view I concluded that this star could be a Be star, I need more observations in the other spectral ranges to confirm or not my conclusion. Recently, Thi et al. (2013) obtained continuum and line observations of 51 Oph with the PACS instrument on board the Herschel Space Observatory and continuum data at 1.2 mm with the IRAM 30 m telescope. They detected a strong emission by atomic oxygen [OI] at 63 microns, which probes warm gas using the Herschel Space Observatory. The [OI] emission at 145 microns, the [C II] emission at 158 microns, the high-J CO emissions, and the warm water emissions were not detected. They could well explain the continuum from the near- to the far-infrared and the [OI] emission by the emission from a compact (R_{out} = 10–15 AU) hydrostatic disk model with a gas mass of $5 \times 10 - 6$ M˙$\odot$, 100 times that of the solid mass. However, this model failed to reproduce the continuum millimeter flux, which hints at a cold outer disk with a mass in solids of $\sim 10^{-6}$ M˙$\odot$. This outer disk could either be free of gas and/or is too cold to emit in the [OI] line. A very flat extended disk model (R_{out} = 400 AU) with a fixed vertical structure and dust settling matched all photometric points and most of the [OI] flux. My future plan is to submit a proposal to observe 51 Oph in the (sub)-millimeter with ALMA, which would help me in constraining the cold gas and dust around this star and thus be able to conclude the precise status of this star.

Since this star is a bright object in the visible, it could be definitely a good candidate to image it using VEGA/CHARA observations in different baseline length and orientations to obtain a rich u-v coverage. I plan to propose this star to the VEGA group in Nice to be "imaged" with as many baselines as possible at visible wavelengths. This will put more constrains on the extension of the gas and thus the status of the star.

Since we could measure the flattening of 51 Oph, the estimation of the effective temperature of the star in the equator and in the pole is of importance. The effective temperature is an important parameter to characterize the central star in order to better understand its evolutionary stage and the connection between the star and the gaseous disk. To do so, I plan to use an interferometry-oriented code (Domiciano de Souza et al. 2002). This code includes radiation transfer, the von Zeipel law ($T_{eff} \propto g_{eff}^{0.25}$, T_{eff} and g_{eff} being the effective temperature and gravity, respectively), and the Roche approximation (e.g. Roche 1837; Kopal 1987).

- In Chapter 4, I studied the inner region of the pre-transitional Herbig Ae/Be star **HD 100546** using PIONIER/VLTI in H band. As I mentioned before, this star hosts at least two protoplanets located in the outer disk, at $\sim$ 50 AU and another

candidate in the disk gap at $\sim$ 10 AU. In this work, I mostly focus on the radial and vertical structure of the inner rim of the inner disk.

My future plan for HD 100546 is the following:

Collecting a coherent set of data in different spectral regions will allow us to better understand the inner rim edge structure of the inner and outer disk of HD 100546. Combining PIONIER data with new MIDI data obtained by Panic et al. 2013 will provide more constrains on the radial and the vertical structure and the shape of the inner rim of the outer disk.

As I discussed in Chapter 4, the natural departure from centro-symmetrical disk models ,i.e., inclined disk models or the sharp inner rim edge of the disk could not explain the non-zero closure phase for long baselines. We proposed that the presence of a clump of dust, related to planet formation could generate such an asymmetry. Adding the clump in the inner disk of HD 100546, we could successfully reproduce the closure phase plot. If the clump has rotated, the estimation of the period of the clump is of importance. We calculated the orbital period of the clump with respect to the central star. Our three days observations with long baselines are less than the period of the clump we obtained, T=0.38 $\pm$ 0.09 year. This shows that the clump can not be tracked by our observations. I would like to submit a proposal for this star to be observed again with PIONIER and mostly with intermediate and longer baselines to figure out whether or not I can track the movement of the clump around the central star at different observations epoches.

- In Chapters 5 and 6, I studied the inner region of the protoplanetary disk around the Herbig star **MWC 480** at a few AUs. Taking into account the Keck observation with one baseline in K band and the MIDI observation with two perpendicular baselines in N band plus SpeX spectrograph on IRTF data in the near-IR, we modeled the circumstellar disk of this star based on a semi-analytical models developed for symmetrical and asymmetrical dusty disk cases. We concluded that in order to fit the visibilties simultaneously with the SED, we need to add a bright feature along the same position angle that we observed our new MIDI data.

  In our best model including a bright feature, there is still a deficit of 10 μm emission. It does not seem that taking into account scattering, we would be able to reproduce this deficit, since scattering has mostly effects in the near-IR flux. Increasing the flux of the bright feature increases the flux at 10 μm but on the other hand, the SED in the near-IR and the MIDI visibilities can not be reproduced.

  My future plan for MWC480 is in following:

  Gas within 1 AU of young stars may reside in protoplanetary disks, infalling streams from inner disks onto the central stars, or in outflows. Observations of gas

and dust on sub-AU scales can thus constrain the composition and dynamics of inner disks, accretion flows, and outflows. The possible mechanism to explain all the star-disk interactions such as stellar winds (Thomas 1999), accretion (Eisner et al. 2009), disk wind (Tatulli et al. 2006) or hot gas (Tatulli et al. 2008) are still in debate. Visible and near-infrared interferometry enables spatially and spectrally resolved observations of sub-AU-sized regions of protoplanetary disks in nearby star-forming regions to probe directly star-disk interactions.

I also plan to submit a proposal to observe a near-IR Brγ line emission that is a trace of accretion/wind with AMBER/VLTI in high spectral resolution and for two perpendicular triplets. Brγ has been observed with Keck and PTI each with just one baseline in medium spectral resolution. Eisner et al. (2009) showed that there is additional flux, and accompanying broad features in V^2, at wavelengths < 2.1 μm. They showed that adding a single-temperature ring with the opacity of water vapor to the dust plus gas model of Eisner et al. (2009), they can fit this additional flux at ~ 2.1 μm. But Najita et al. (2009) presented high resolution K-band spectroscopy of MWC 480 and showed that the spectrum of this star except for Brγ is featureless. They concluded that the additional flux in the warmer side of Brγ has another origin and not water vapor. Also, the Brγ emission centroid are blueshifted from its systemic velocities by -6.8 km s^{-1} in high spectral resolution compared to medium resolution. Therefore, these features motivated me to submit a proposal to observe MWC 480 around Brγ emission using different baselines with different orientations to figure out the origin of the additional flux at ~ 2.1 μm as well as estimating more precisely the Brγ extension and its kinematics taking advantages of AMBER high spatial-spectral resolution.

Based on Keck observations at K band and MIDI observations at N band, we show that any attempts at reproducing our data with symmetrical models have failed. A hypothesis based on a bright feature added to our two-component disk model at a few AUs from the central star was successful to match all data at once. Reconstructing images of this disk with the upcoming second-generation VLTI instrument MATISSE constitutes a unique perspective to further assess the nature of the inner region of the disk around MWC480. MATISSE will recombine up to four telescopes in the mid-IR (from 3 to 13 μm) and will thus provide a more complete UV coverage with different baseline orientations, and, closure phase measurements, that will be used to reveal unambiguously brightness asymmetries.

Conclusion

Dans cette thèse, j'ai démontré la puissance de la technique interférométrique pour déterminer les propriétés des gaz et des poussières des disques circumstellaires autour de jeunes objets stellaires du visible à la bande spectrale du mid-IR. Les observations interférométriques visibles peuvent sonder la photosphère d'une source résolue dans le continuum ainsi que la géométrie et la cinématique du disque gazeux produisant la raie $H\alpha$ ou la raie du triplet Ca II à léchelle sous-UA. Ces observations permettent de tirer les paramètres stellaires, par exemple, le diamètre, la masse, la température, et de limiter l'extension de la ligne d'émission et de comprendre le processus physique du gaz à proximité de l'étoile centrale. Les observations interférométriques dans le proche infrarouge, sondent le gaz chaud et la distribution de la poussière à une fraction d'UA de l'étoile centrale et permettent de comprendre la cinématique du gaz et ses processus physiques responsables de l'accrétion de gaz sur l'étoile et le mécanisme de sortie ainsi que les propriétés et le mécanisme physique de la poussière chaude qui déterminent l'évolution du disque et la formation des planètes. Les observations interférométriques dans l'infrarouge moyen sondent la plupart de la poussière chaude de la région la plus inté jusqu'à quelques UA et permettent ainsi d'étudier les propriétés de la poussière et dans leur régime d'émission.

En raison des limitations des interféromètres disponibles du visible à l'infrarouge moyen, les observations directes du gaz et de poussière disque interne et l'étude de l'étoile elle-même ont été limités jusqu'ici aux objets lumineux. Lors de ma thèse, j'ai travaillé sur quelques questions, que rendait possible l'observabilité avec les interféromètres actuels.

J'analyse les observations interférométriques dans le visibles d'une jeune étoile à rotation rapide, 51 Oph, dans le continuum et la raie d'émission $H\alpha$. Je voulais résoudre spatialement la photosphère, et environnement gazeux de cette étoile. J'utilise la recombinaison de faisceaux visibles, VEGA installé sur le réseau CHARA, qui atteint une résolution en dessous de milliarcseconde. J'en est déduit pour la première fois, l'extension et l'aplatissement la photosphère de 51 Oph . J'ai trouvé un grand axe de $\theta_{\rm eq} = 8.08 \pm 0.70\, R_\odot$ et un petit axe de $\theta_{\rm pol}$=$5.66 \pm 0.23\, R_\odot$. Cette distorsion de la haute photosphère montre que l'étoile tourne près de sa vitesse critique. Enfin, en utilisant des mesures interféromètriques dans la raie $H\alpha$, a permis de contraindre la géométrie et la cinématique de l'environnement circumstellaire et montré que l'émission est produite dans un disque de $R_\star$ 5.2 $\pm$ 2 en rotation képlerienne . Dans le domaine visible, 51 Oph présente toutes les caractéristiques d'une étoile Be classique: rotation proche de la

vitesse critique et un double pic Hα en raie démission produite dans un disque gazeux en rotation képlerienne. Toutefois, cela n'explique pas la présence de poussière, comme on le voit dans le spectre infrarouge moyen et millimètrique, et le statut évolutif de 51 Oph reste non réglé.

J'analyse les observations interférométriques dans le proche infrarouge d'une étoile Herbig Be HD 100546 qui montre les signes d'un interstice qui serait situé à l'intérieur des 12 premières UA de son disque de pré-transitionnel. J'ai obtenu une grande quantité de nouvelles données interférométriques de l'instrument PIONIER / VLTI en bande H. La partie essentielle de l'émission provient de la poussière chaude situèe plus à l'intérieur du disque circumstellaire . En combinant les mesures d'observation interférométriques avec les observations photométriques, j'étudie l'environnement circumstellaire de HD 100546 en modélisant l'émission infrarouge du disque en utilisant un code de transfert radiatif Monte-Carlo 3D MCFOST. La détection d'un clôture de phase différente de zéro à longue ligne de base me conduit à proposer que le bord interne du disque de HD 100546 pourrait ne pas être lisse. L'écart de symétrie entre le modèle de disque centro-symétrique, i.e., du modèle d'un disque incliné ou le bord interne du disque abrupt ne peuvent expliquer une clôture de phase différente de zéro. J'ai testé une hypothése basée sur la présence d'un "blob" dans le bord interne, qui semble prometteuse mais nécessite d'autres investigations.

J'analyse les observations interférométriques dans l'infrarouge moyen d'une étoile Herbig Ae MWC 480. La structure interne et les propriétés (par exemple, la température, la masse) du disque circumstellaire de l'étoile Herbig MWC 480 sont étudiés par le biais de l'interférométrie stellaire infrarouge et sont interprétées en utilisant des modèles semi-analytiques. De ces modèles, la SED a été reproduite et la carte de l'intensité de la source a été calcul. La carte d'intensité est fournie en entrée pour la modélisation à partir des données de l'interféromètre Keck (KI) dans la proche infrarouge et des données de l'instrument MIDI dans l'infrarouge moyen installé au VLTI en 2007. Je conclue qu'avec mon ensemble limité de données, je peux reproduire la SED, les visibilités de MIDI et du Keck en utilisant un modèle de disque à deux composantes. De plus, je soupçonne que MWC480 possède un disque de poussière de transition. De nouvelles données me conduisent a étudié de particuliérement récentes données MIDI du Very Large Telescope Interferometer (VLTI) acquises en Décembre 2013. L'utilisation de modèles symétriques pour le disque pourrait ne pas simultanément reproduire toutes mes données: la distribution spectrale de l'énergie, les données proche infrarouge d'interférométre Keck et celles dans l'infrarouge moyen de l'instrument MIDI en 2007 et 2013. Afin d'expliquer toutes les mesures et en supposant que la structure du disque de MWC480 n'a pas varié avec le temps, l'utilisation de modèles asymétriques apparaît nécessaire. Plusieurs

scénarios sont testés, l'une d'eux considère la présence d'un élément azimutal brillant dans la composante interne du modèle du disque fournit un bon ajustement des données.

Appendix A

Papers

Published papers

My Chapter 3 and 5 have been published as following:

1) N. Jamialahmadi, Ph. Berio, A. Meilland, K.Perraut,... (2015) : The peculiar fast-rotating star 51 Oph probed by VEGA/CHARA Astronomy and Astrophysics (A&A), Volume 579, A81, July 2015

2) N. Jamialahmadi, B. Lopez, Ph. Berio, S.Flament, A. Spang (2014) Study of the inner disk of the Herbig star MWC480 Astrophysics and Space Sience (AP&SS), Volume 355, Issue 1, pp. 105-116

Submitted papers

My Chapter 6 has been submitted to Monthly Notice of the Royal Astronomical Socity (MNRAS).

In preparation

My Chapter 4 will be submitten soon to Monthly Notice of the Royal Astronomical Socity (MNRAS).

Bibliography

A.-K. M. Tannirkulam. *A comprehensive study of proto-planetary disks around Herbig Ae stars using long-baseline infrared interferometry.* PhD thesis, University of Michigan, 2008.

D. Bonneau, J.-M. Clausse, X. Delfosse, D. Mourard, S. Cetre, A. Chelli, P. Cruzalèbes, G. Duvert, and G. Zins. SearchCal: a virtual observatory tool for searching calibrators in optical long baseline interferometry. I. The bright object case. *A&A*, 456:789–789, September 2006. doi: 10.1051/0004-6361:20054469.

J. A. Eisner, L. A. Hillenbrand, R. J. White, J. S. Bloom, R. L. Akeson, and C. H. Blake. Near-Infrared Interferometric, Spectroscopic, and Photometric Monitoring of T Tauri Inner Disks. *ApJ*, 669:1072–1084, November 2007. doi: 10.1086/521874.

J. A. Eisner, J. R. Graham, R. L. Akeson, and J. Najita. Spatially Resolved Spectroscopy of Sub-AU-Sized Regions of T Tauri and Herbig Ae/Be Disks. *ApJ*, 692:309–323, February 2009. doi: 10.1088/0004-637X/692/1/309.

T. Birnstiel, C. P. Dullemond, and F. Brauer. Gas- and dust evolution in protoplanetary disks. *A&A*, 513:A79, April 2010. doi: 10.1051/0004-6361/200913731.

F. H. Shu, F. C. Adams, and S. Lizano. Star formation in molecular clouds - Observation and theory. *araa*, 25:23–81, 1987. doi: 10.1146/annurev.aa.25.090187.000323.

S. E. Strom. Optical and Infrared Observations of Young Stellar Objects - an Informal Review. *PASP*, 84:745, December 1972. doi: 10.1086/129375.

M. A. Pogodin, S. Hubrig, R. V. Yudin, M. Schöller, J. F. González, and B. Stelzer. Measuring the mass accretion rates of Herbig Ae/Be stars with X-shooter. *Astronomische Nachrichten*, 333:594–612, August 2012. doi: 10.1002/asna.201211706.

B. Zuckerman. Dusty Circumstellar Disks. *araa*, 39:549–580, 2001. doi: 10.1146/annurev.astro.39.1.549.

C. Marois, B. Macintosh, T. Barman, B. Zuckerman, I. Song, J. Patience, D. Lafrenière, and R. Doyon. Direct Imaging of Multiple Planets Orbiting the Star HR 8799. *Science*, 322:1348–, November 2008. doi: 10.1126/science.1166585.

J. Carson, C. Thalmann, M. Janson, T. Kozakis, M. Bonnefoy, B. Biller, J. Schlieder, T. Currie, M. McElwain, M. Goto, T. Henning, W. Brandner, M. Feldt, R. Kandori, M. Kuzuhara, L. Stevens, P. Wong, K. Gainey, M. Fukagawa, Y. Kuwada, T. Brandt, J. Kwon, L. Abe, S. Egner, C. Grady, O. Guyon, J. Hashimoto, Y. Hayano, M. Hayashi, S. Hayashi, K. Hodapp, M. Ishii, M. Iye, G. Knapp, T. Kudo, N. Kusakabe, T. Matsuo, S. Miyama, J. Morino, A. Moro-Martin, T. Nishimura, T. Pyo, E. Serabyn, H. Suto, R. Suzuki, M. Takami, N. Takato, H. Terada, D. Tomono, E. Turner, M. Watanabe, J. Wisniewski, T. Yamada, H. Takami, T. Usuda, and M. Tamura. Direct Imaging Discovery of a "Super-Jupiter" around the Late B-type Star κ And. *ApJ*, 763:L32, February 2013. doi: 10.1088/2041-8205/763/2/L32.

S. J. Weidenschilling. Dust to planetesimals - Settling and coagulation in the solar nebula. , 44:172–189, October 1980. doi: 10.1016/0019-1035(80)90064-0.

J. B. Pollack, O. Hubickyj, P. Bodenheimer, J. J. Lissauer, M. Podolak, and Y. Greenzweig. Formation of the Giant Planets by Concurrent Accretion of Solids and Gas. , 124:62–85, November 1996. doi: 10.1006/icar.1996.0190.

E. Chiang and A. N. Youdin. Forming Planetesimals in Solar and Extrasolar Nebulae. *Annual Review of Earth and Planetary Sciences*, 38:493–522, May 2010. doi: 10.1146/annurev-earth-040809-152513.

A. Morbidelli and D. Nesvorny. Dynamics of pebbles in the vicinity of a growing planetary embryo: hydro-dynamical simulations. *A&A*, 546:A18, October 2012. doi: 10.1051/0004-6361/201219824.

L. Hartmann, N. Calvet, E. Gullbring, and P. D'Alessio. Accretion and the Evolution of T Tauri Disks. *ApJ*, 495:385–400, March 1998. doi: 10.1086/305277.

D. Lynden-Bell and J. E. Pringle. The evolution of viscous discs and the origin of the nebular variables. *MNRAS*, 168:603–637, September 1974.

J. E. Pringle. Accretion discs in astrophysics. *araa*, 19:137–162, 1981. doi: 10.1146/annurev.aa.19.090181.001033.

N. I. Shakura and R. A. Sunyaev. Black holes in binary systems. Observational appearance. *A&A*, 24:337–355, 1973.

S. P. Ruden and J. B. Pollack. The dynamical evolution of the protosolar nebula. *ApJ*, 375:740–760, July 1991. doi: 10.1086/170239.

S. J. Weidenschilling. When the dust settles - Fractal aggregates and planetesimal formation. In *Lunar and Planetary Science Conference*, volume 28 of *Lunar and Planetary Inst. Technical Report*, page 1517, March 1997.

C. Hayashi. Structure of the Solar Nebula, Growth and Decay of Magnetic Fields and Effects of Magnetic and Turbulent Viscosities on the Nebula. *Progress of Theoretical Physics Supplement*, 70:35–53, 1981. doi: 10.1143/PTPS.70.35.

S. J. Kenyon and L. Hartmann. Spectral energy distributions of T Tauri stars - Disk flaring and limits on accretion. *ApJ*, 323:714–733, December 1987. doi: 10.1086/165866.

E. I. Chiang and P. Goldreich. Spectral Energy Distributions of T Tauri Stars with Passive Circumstellar Disks. *ApJ*, 490:368–376, November 1997.

D. Watson. Mineralization, Grain Growth, and Disk Structure: Observations of the Evolution of Dust in Protoplanetary Disks. In T. Henning, E. Grün, and J. Steinacker, editors, *Cosmic Dust - Near and Far*, volume 414 of *Astronomical Society of the Pacific Conference Series*, page 77, December 2009.

A. Juhász, J. Bouwman, T. Henning, B. Acke, M. E. van den Ancker, G. Meeus, C. Dominik, M. Min, A. G. G. M. Tielens, and L. B. F. M. Waters. Dust Evolution in Protoplanetary Disks Around Herbig Ae/Be Starsthe Spitzer View. *ApJ*, 721:431–455, September 2010. doi: 10.1088/0004-637X/721/1/431.

K. Miyake and Y. Nakagawa. Effects of particle size distribution on opacity curves of protoplanetary disks around T Tauri stars. , 106:20, November 1993. doi: 10.1006/icar.1993.1156.

J. B. Pollack, D. Hollenbach, S. Beckwith, D. P. Simonelli, T. Roush, and W. Fong. Composition and radiative properties of grains in molecular clouds and accretion disks. *ApJ*, 421:615–639, February 1994. doi: 10.1086/173677.

B. T. Draine and K. Allaf-Akbari. X-Ray Scattering by Nonspherical Grains. I. Oblate Spheroids. *ApJ*, 652:1318–1330, December 2006. doi: 10.1086/508133.

M. Min, L. B. F. M. Waters, A. de Koter, J. W. Hovenier, L. P. Keller, and F. Markwick-Kemper. The shape and composition of interstellar silicate grains. *A&A*, 462:667–676, February 2007. doi: 10.1051/0004-6361:20065436.

M. Min, J. W. Hovenier, and A. de Koter. Modeling optical properties of cosmic dust grains using a distribution of hollow spheres. *A&A*, 432:909–920, March 2005. doi: 10.1051/0004-6361:20041920.

S. K. Dunkin, M. J. Barlow, and S. G. Ryan. High-resolution spectroscopy of Vega-like stars - I. Effective temperatures, gravities and photospheric abundances. *MNRAS*, 286:604–616, April 1997a. doi: 10.1093/mnras/286.3.604.

H. A. Abt and N. I. Morrell. The Relation between Rotational Velocities and Spectral Peculiarities among A-Type Stars. *ApJ*, 99:135, July 1995. doi: 10.1086/192182.

H. A. Abt, H. Levato, and M. Grosso. Rotational Velocities of B Stars. *ApJ*, 573: 359–365, July 2002. doi: 10.1086/340590.

G. van Belle, D. R. Ciardi, R. R. Thompson, R. L. Akeson, and E. A. Lada. Altair's Oblateness and Rotation Velocity from Long-Baseline Interferometry. In *American Astronomical Society Meeting Abstracts #198*, volume 33 of *Bulletin of the American Astronomical Society*, page 881, May 2001.

J. P. Aufdenberg, A. Mérand, V. Coudé du Foresto, O. Absil, E. Di Folco, P. Kervella, S. T. Ridgway, D. H. Berger, T. A. ten Brummelaar, H. A. McAlister, J. Sturmann, L. Sturmann, and N. H. Turner. First Results from the CHARA Array. VII. Long-Baseline Interferometric Measurements of Vega Consistent with a Pole-On, Rapidly Rotating Star. *ApJ*, 645:664–675, July 2006. doi: 10.1086/504149.

D. M. Peterson, C. A. Hummel, T. A. Pauls, J. T. Armstrong, J. A. Benson, G. C. Gilbreath, R. B. Hindsley, D. J. Hutter, K. J. Johnston, D. Mozurkewich, and H. R. Schmitt. Vega is a rapidly rotating star. *nat*, 440:896–899, April 2006. doi: 10.1038/nature04661.

A. Domiciano de Souza, P. Kervella, S. Jankov, L. Abe, F. Vakili, E. di Folco, and F. Paresce. The spinning-top Be star Achernar from VLTI-VINCI. *A&A*, 407:L47–L50, August 2003. doi: 10.1051/0004-6361:20030786.

J. D. Monnier, M. Zhao, E. Pedretti, N. Thureau, M. Ireland, P. Muirhead, J.-P. Berger, R. Millan-Gabet, G. Van Belle, T. ten Brummelaar, H. McAlister, S. Ridgway, N. Turner, L. Sturmann, J. Sturmann, and D. Berger. Imaging the Surface of Altair. *Science*, 317:342–, July 2007. doi: 10.1126/science.1143205.

M. E. van den Ancker, G. Meeus, J. Cami, L. B. F. M. Waters, and C. Waelkens. The composition of circumstellar gas and dust in 51 Oph. *A&A*, 369:L17–L21, April 2001. doi: 10.1051/0004-6361:20010245.

G. Meeus, L. B. F. M. Waters, J. Bouwman, M. E. van den Ancker, C. Waelkens, and K. Malfait. ISO spectroscopy of circumstellar dust in 14 Herbig Ae/Be systems: Towards an understanding of dust processing. *A&A*, 365:476–490, January 2001. doi: 10.1051/0004-6361:20000144.

K. Malfait, E. Bogaert, and C. Waelkens. An ultraviolet, optical and infrared study of Herbig Ae/Be stars. *A&A*, 331:211–223, March 1998a.

W. F. Thi, F. Ménard, G. Meeus, A. Carmona, P. Riviere-Marichalar, J.-C. Augereau, I. Kamp, P. Woitke, C. Pinte, I. Mendigutía, C. Eiroa, B. Montesinos, S. Britain, and W. Dent. Nature of the gas and dust around 51 Ophiuchi. Modelling continuum and Herschel line observations. *A&A*, 557:A111, September 2013. doi: 10.1051/0004-6361/201221002.

M. G. Berthoud. *Carbon monoxide emission from the inner disk around intermediate-mass stars*. PhD thesis, Cornell University, 2008.

E. Tatulli, F. Malbet, F. Ménard, C. Gil, L. Testi, A. Natta, S. Kraus, P. Stee, and S. Robbe-Dubois. Spatially resolving the hot CO around the young Be star 51 Ophiuchi. *A&A*, 489:1151–1155, October 2008. doi: 10.1051/0004-6361:200809627.

D. Mourard, J. M. Clausse, A. Marcotto, K. Perraut, I. Tallon-Bosc, P. Bério, A. Blazit, D. Bonneau, S. Bosio, Y. Bresson, O. Chesneau, O. Delaa, F. Hénault, Y. Hughes, S. Lagarde, G. Merlin, A. Roussel, A. Spang, P. Stee, M. Tallon, P. Antonelli, R. Foy, P. Kervella, R. Petrov, E. Thiebaut, F. Vakili, H. McAlister, T. ten Brummelaar, J. Sturmann, L. Sturmann, N. Turner, C. Farrington, and P. J. Goldfinger. VEGA: Visible spEctroGraph and polArimeter for the CHARA array: principle and performance. *A&A*, 508:1073–1083, December 2009. doi: 10.1051/0004-6361/200913016.

D. Mourard, P. Bério, K. Perraut, R. Ligi, A. Blazit, J. M. Clausse, N. Nardetto, A. Spang, I. Tallon-Bosc, D. Bonneau, O. Chesneau, O. Delaa, F. Millour, P. Stee, J. B. Le Bouquin, T. ten Brummelaar, C. Farrington, P. J. Goldfinger, and J. D. Monnier. Spatio-spectral encoding of fringes in optical long-baseline interferometry. Example of the 3T and 4T recombining mode of VEGA/CHARA. *A&A*, 531:A110, July 2011. doi: 10.1051/0004-6361/201116976.

T. A. ten Brummelaar, H. A. McAlister, S. T. Ridgway, W. G. Bagnuolo, Jr., N. H. Turner, L. Sturmann, J. Sturmann, D. H. Berger, C. E. Ogden, R. Cadman, W. I. Hartkopf, C. H. Hopper, and M. A. Shure. First Results from the CHARA Array. II. A Description of the Instrument. *ApJ*, 628:453–465, July 2005. doi: 10.1086/430729.

F. van Leeuwen. Validation of the new Hipparcos reduction. *A&A*, 474:653–664, November 2007. doi: 10.1051/0004-6361:20078357.

A. Meilland, F. Millour, S. Kanaan, P. Stee, R. Petrov, K.-H. Hofmann, A. Natta, and K. Perraut. First spectro-interferometric survey of Be stars. I. Observations and constraints on the disk geometry and kinematics. *A&A*, 538:A110, February 2012. doi: 10.1051/0004-6361/201117955.

S. K. Dunkin, M. J. Barlow, and S. G. Ryan. High-resolution spectroscopy of Vega-like stars - II. Age indicators, activity and circumstellar gas. *MNRAS*, 290:165–185, September 1997b.

I. Hubeny. Non-LTE line-blanketed model atmospheres of hot stars. In K. L. Chan, K. S. Cheng, and H. P. Singh, editors, *1997 Pacific Rim Conference on Stellar Astrophysics*, volume 138 of *Astronomical Society of the Pacific Conference Series*, page 139, 1998.

A. Meilland, O. Delaa, P. Stee, S. Kanaan, F. Millour, D. Mourard, D. Bonneau, R. Petrov, N. Nardetto, A. Marcotto, A. Roussel, J. M. Clausse, K. Perraut, H. McAlister, T. ten Brummelaar, J. Sturmann, L. Sturmann, N. Turner, S. T. Ridgway, C. Farrington, and P. J. Goldfinger. The binary Be star δ Scorpii at high spectral and spatial resolution. I. Disk geometry and kinematics before the 2011 periastron. *A&A*, 532:A80, August 2011. doi: 10.1051/0004-6361/201116798.

O. Delaa, P. Stee, A. Meilland, J. Zorec, D. Mourard, P. Bério, D. Bonneau, O. Chesneau, J. M. Clausse, P. Cruzalebes, K. Perraut, A. Marcotto, A. Roussel, A. Spang, H. McAlister, T. ten Brummelaar, J. Sturmann, L. Sturmann, N. Turner, C. Farrington, and P. J. Goldfinger. Kinematics and geometrical study of the Be stars 48 Persei and ψ Persei with the VEGA/CHARA interferometer. *A&A*, 529:A87, May 2011. doi: 10.1051/0004-6361/201015639.

W.-F. Thi, B. van Dalen, A. Bik, and L. B. F. M. Waters. Evidence for a hot dust-free inner disk around 51 Oph. *A&A*, 430:L61–L64, January 2005. doi: 10.1051/0004-6361:200400132.

C. C. Stark, M. J. Kuchner, W. A. Traub, J. D. Monnier, E. Serabyn, M. Colavita, C. Koresko, B. Mennesson, and L. D. Keller. 51 Ophiuchus: A Possible Beta Pictoris Analog Measured with the Keck Interferometer Nuller. *ApJ*, 703:1188–1197, October 2009. doi: 10.1088/0004-637X/703/2/1188.

C. Martin-Zaïdi, M. Deleuil, J. Le Bourlot, J.-C. Bouret, A. Roberge, C. P. Dullemond, L. Testi, P. D. Feldman, A. Lecavelier Des Etangs, and A. Vidal-Madjar. Molecular hydrogen in the circumstellar environments of Herbig Ae/Be stars probed by FUSE. *A&A*, 484:225–239, June 2008. doi: 10.1051/0004-6361:20079325.

J. A. Valenti, A. A. Fallon, and C. M. Johns-Krull. An IUE Atlas of Pre-Main-Sequence Stars. III. Co-added Final Archive Spectra from the Long-Wavelength Cameras. *ApJ*, 147:305–336, August 2003. doi: 10.1086/375445.

R. M. Cutri, M. F. Skrutskie, S. van Dyk, C. A. Beichman, J. M. Carpenter, T. Chester, L. Cambresy, T. Evans, J. Fowler, J. Gizis, E. Howard, J. Huchra, T. Jarrett, E. L. Kopan, J. D. Kirkpatrick, R. M. Light, K. A. Marsh, H. McCallon, S. Schneider,

R. Stiening, M. Sykes, M. Weinberg, W. A. Wheaton, S. Wheelock, and N. Zacarias. VizieR Online Data Catalog: 2MASS All-Sky Catalog of Point Sources (Cutri+ 2003). *VizieR Online Data Catalog*, 2246:0, June 2003.

P. Ábrahám and M. Kun. Isophot-S Spectral Atlas of Young Stellar Objects. *Baltic Astronomy*, 13:464–469, 2004.

P. E. Clegg, P. A. R. Ade, C. Armand, J.-P. Baluteau, M. J. Barlow, M. A. Buckley, J.-C. Berges, M. Burgdorf, E. Caux, C. Ceccarelli, R. Cerulli, S. E. Church, F. Cotin, P. Cox, P. Cruvellier, J. L. Culhane, G. R. Davis, A. di Giorgio, B. R. Diplock, D. L. Drummond, R. J. Emery, J. D. Ewart, J. Fischer, I. Furniss, W. M. Glencross, M. A. Greenhouse, M. J. Griffin, C. Gry, A. S. Harwood, A. S. Hazell, M. Joubert, K. J. King, T. Lim, R. Liseau, J. A. Long, D. Lorenzetti, S. Molinari, A. G. Murray, D. A. Naylor, B. Nisini, K. Norman, A. Omont, R. Orfei, T. J. Patrick, D. Pequignot, D. Pouliquen, M. C. Price, Nguyen-Q-Rieu, A. J. Rogers, F. D. Robinson, M. Saisse, P. Saraceno, G. Serra, S. D. Sidher, A. F. Smith, H. A. Smith, L. Spinoglio, B. M. Swinyard, D. Texier, W. A. Towlson, N. R. Trams, S. J. Unger, and G. J. White. The ISO Long-Wavelength Spectrometer. *A&A*, 315:L38–L42, November 1996.

K. Malfait, C. Waelkens, L. B. F. M. Waters, B. Vandenbussche, E. Huygen, and M. S. de Graauw. The spectrum of the young star HD 100546 observed with the Infrared Space Observatory. *A&A*, 332:L25–L28, April 1998b.

I. Mendigutía, W. J. de Wit, R. D. Oudmaijer, J. R. Fairlamb, A. C. Carciofi, J. D. Ilee, and R. G. Vieira. High-resolution Br γ spectro-interferometry of the transitional Herbig Ae/Be star HD 100546: a Keplerian gaseous disc inside the inner rim. *MNRAS*, 453:2126–2132, October 2015. doi: 10.1093/mnras/stv1777.

S. D. Brittain, J. R. Najita, and J. S. Carr. Near infrared high resolution spectroscopy and spectro-astrometry of gas in disks around Herbig Ae/Be stars. *apss*, 357:54, May 2015. doi: 10.1007/s10509-015-2260-4.

C. Leinert, U. Graser, F. Przygodda, L. B. F. M. Waters, G. Perrin, W. Jaffe, B. Lopez, E. J. Bakker, A. Böhm, O. Chesneau, W. D. Cotton, S. Damstra, J. de Jong, A. W. Glazenborg-Kluttig, B. Grimm, H. Hanenburg, W. Laun, R. Lenzen, S. Ligori, R. J. Mathar, J. Meisner, S. Morel, W. Morr, U. Neumann, J.-W. Pel, P. Schuller, R.-R. Rohloff, B. Stecklum, C. Storz, O. von der Lühe, and K. Wagner. MIDI - the 10 \mum instrument on the VLTI. *apss*, 286:73–83, 2003. doi: 10.1023/A:1026158127732.

W. J. Jaffe. Coherent fringe tracking and visibility estimation for MIDI. In W. A. Traub, editor, *New Frontiers in Stellar Interferometry*, volume 5491 of *Society of Photo-Optical Instrumentation Engineers (SPIE) Conference Series*, page 715, October 2004.

N. Kusakabe, C. A. Grady, M. L. Sitko, J. Hashimoto, T. Kudo, M. Fukagawa, T. Muto, J. P. Wisniewski, M. Min, S. Mayama, C. Werren, A. N. Day, L. C. Beerman, D. K. Lynch, R. W. Russell, S. M. Brafford, M. Kuzuhara, T. D. Brandt, L. Abe, W. Brandner, J. Carson, S. Egner, M. Feldt, M. Goto, O. Guyon, Y. Hayano, M. Hayashi, S. S. Hayashi, T. Henning, K. W. Hodapp, M. Ishii, M. Iye, M. Janson, R. Kandori, G. R. Knapp, T. Matsuo, M. W. McElwain, S. Miyama, J.-I. Morino, A. Moro-Martin, T. Nishimura, T.-S. Pyo, H. Suto, R. Suzuki, M. Takami, N. Takato, H. Terada, C. Thalmann, D. Tomono, E. L. Turner, M. Watanabe, T. Yamada, H. Takami, T. Usuda, and M. Tamura. High-contrast Near-infrared Polarization Imaging of MWC480. *ApJ*, 753:153, July 2012. doi: 10.1088/0004-637X/753/2/153.

M. L. Sitko, W. J. Carpenter, R. L. Kimes, J. L. Wilde, D. K. Lynch, R. W. Russell, R. J. Rudy, S. M. Mazuk, C. C. Venturini, R. C. Puetter, C. A. Grady, E. F. Polomski, J. P. Wisnewski, S. M. Brafford, H. B. Hammel, and R. B. Perry. Variability of Disk Emission in Pre-Main-Sequence and Related Stars. I. HD 31648 and HD 163296: Isolated Herbig Ae Stars Driving Herbig-Haro Flows. *ApJ*, 678:1070–1087, May 2008. doi: 10.1086/529003.

C. A. Grady, K. Hamaguchi, G. Schneider, B. Stecklum, B. E. Woodgate, J. E. McCleary, G. M. Williger, M. L. Sitko, F. Ménard, T. Henning, S. Brittain, M. Troutmann, B. Donehew, D. Hines, J. P. Wisniewski, D. K. Lynch, R. W. Russell, R. J. Rudy, A. N. Day, A. Shenoy, D. Wilner, M. Silverstone, J.-C. Bouret, H. Meusinger, M. Clampin, S. Kim, R. Petre, M. Sahu, M. Endres, and K. A. Collins. Locating the Accretion Footprint on a Herbig Ae Star: MWC 480. *ApJ*, 719:1565–1581, August 2010. doi: 10.1088/0004-637X/719/2/1565.

A. Tannirkulam, T. J. Harries, and J. D. Monnier. The Inner Rim of YSO Disks: Effects of Dust Grain Evolution. *ApJ*, 661:374–384, May 2007. doi: 10.1086/513265.

M. J. Creech-Eakman, E. I. Chiang, R. M. K. Joung, G. A. Blake, and E. F. van Dishoeck. ISO LWS Spectra of T Tauri and Herbig AeBe stars. *A&A*, 385:546–562, April 2002. doi: 10.1051/0004-6361:20020157.

J. R. Houck, T. L. Roellig, J. Van Cleve, W. J. Forrest, T. L. Herter, C. R. Lawrence, K. Matthews, H. J. Reitsema, B. T. Soifer, D. M. Watson, D. Weedman, M. Huisjen, J. R. Troeltzsch, D. J. Barry, J. Bernard-Salas, C. Blacken, B. R. Brandl, V. Charmandaris, D. Devost, G. E. Gull, P. Hall, C. P. Henderson, S. J. U. Higdon, B. E. Pirger, J. Schoenwald, G. C. Sloan, K. I. Uchida, P. N. Appleton, L. Armus, M. J. Burgdorf, S. B. Fajardo-Acosta, C. J. Grillmair, J. G. Ingalls, P. W. Morris, and H. I. Teplitz. The infrared spectrograph on the Spitzer Space Telescope. In J. C. Mather, editor, *Optical, Infrared, and Millimeter Space Telescopes*, volume 5487 of *Society*

of Photo-Optical Instrumentation Engineers (SPIE) Conference Series, pages 62–76, October 2004. doi: 10.1117/12.550517.

S. V. W. Beckwith, A. I. Sargent, R. S. Chini, and R. Guesten. A survey for circumstellar disks around young stellar objects. *AJ*, 99:924–945, March 1990. doi: 10.1086/115385.

C. P. Dullemond, C. Dominik, and A. Natta. Passive Irradiated Circumstellar Disks with an Inner Hole. *ApJ*, 560:957–969, October 2001. doi: 10.1086/323057.

W.-F. Thi, E. F. van Dishoeck, K. M. Pontoppidan, and E. Dartois. Evidence for episodic warm outflowing CO gas from the intermediate-mass young stellar object IRAS 08470-4321. *MNRAS*, 406:1409–1424, August 2010. doi: 10.1111/j.1365-2966.2010.16509.x.

A. Dutrey, S. Guilloteau, L. Prato, M. Simon, G. Duvert, K. Schuster, and F. Menard. CO study of the GM Aurigae Keplerian disk. *A&A*, 338:L63–L66, October 1998.

A. Dutrey, V. Wakelam, Y. Boehler, S. Guilloteau, F. Hersant, D. Semenov, E. Chapillon, T. Henning, V. Piétu, R. Launhardt, F. Gueth, and K. Schreyer. Chemistry in disks. V. Sulfur-bearing molecules in the protoplanetary disks surrounding LkCa15, MWC480, DM Tauri, and GO Tauri. *A&A*, 535:A104, November 2011. doi: 10.1051/0004-6361/201116931.

J. A. Eisner, J. D. Monnier, J. Woillez, R. L. Akeson, R. Millan-Gabet, J. R. Graham, L. A. Hillenbrand, J.-U. Pott, S. Ragland, and P. Wizinowich. Spatially and Spectrally Resolved Hydrogen Gas within 0.1 AU of T Tauri and Herbig Ae/Be Stars. *ApJ*, 718: 774–794, August 2010. doi: 10.1088/0004-637X/718/2/774.

V. Mannings and A. I. Sargent. A High-Resolution Study of Gas and Dust around Young Intermediate-Mass Stars: Evidence for Circumstellar Disks in Herbig Ae Systems. *ApJ*, 490:792–802, December 1997.

M. Simon, A. Dutrey, and S. Guilloteau. Dynamical Masses of T Tauri Stars and Calibration of Pre-Main-Sequence Evolution. *ApJ*, 545:1034–1043, December 2000. doi: 10.1086/317838.

V. Piétu, A. Dutrey, S. Guilloteau, E. Chapillon, and J. Pety. Resolving the inner dust disks surrounding LkCa 15 and MWC 480 at mm wavelengths. *A&A*, 460:L43–L47, December 2006. doi: 10.1051/0004-6361:20065968.

E. Chapillon, S. Guilloteau, A. Dutrey, V. Piétu, and M. Guélin. Chemistry in disks. VI. CN and HCN in protoplanetary disks. *A&A*, 537:A60, January 2012. doi: 10.1051/0004-6361/201116762.

V. Piétu, A. Dutrey, and S. Guilloteau. Probing the structure of protoplanetary disks: a comparative study of DM Tau, LkCa 15, and MWC 480. *A&A*, 467:163–178, May 2007. doi: 10.1051/0004-6361:20066537.

E. Tatulli, M. Benisty, F. Ménard, P. Varnière, C. Martin-Zaïdi, W.-F. Thi, C. Pinte, F. Massi, G. Weigelt, K.-H. Hofmann, and R. G. Petrov. Constraining the structure of the planet-forming region in the disk of the Herbig Be star HD 100546. *A&A*, 531: A1, July 2011. doi: 10.1051/0004-6361/201016165.

C. Espaillat, L. Ingleby, J. Hernández, E. Furlan, P. D'Alessio, N. Calvet, S. Andrews, J. Muzerolle, C. Qi, and D. Wilner. On the Transitional Disk Class: Linking Observations of T Tauri Stars and Physical Disk Models. *ApJ*, 747:103, March 2012. doi: 10.1088/0004-637X/747/2/103.

A. Laor and B. T. Draine. Spectroscopic constraints on the properties of dust in active galactic nuclei. *ApJ*, 402:441–468, January 1993. doi: 10.1086/172149.

N. Jamialahmadi, B. Lopez, P. Berio, S. Flament, and A. Spang. Study of the inner disk of the Herbig star MWC480. *apss*, December 2014. doi: 10.1007/s10509-014-2155-9.

J. Hashimoto, M. Tamura, T. Muto, T. Kudo, M. Fukagawa, T. Fukue, M. Goto, C. A. Grady, T. Henning, K. Hodapp, M. Honda, S. Inutsuka, E. Kokubo, G. Knapp, M. W. McElwain, M. Momose, N. Ohashi, Y. K. Okamoto, M. Takami, E. L. Turner, J. Wisniewski, M. Janson, L. Abe, W. Brandner, J. Carson, S. Egner, M. Feldt, T. Golota, O. Guyon, Y. Hayano, M. Hayashi, S. Hayashi, M. Ishii, R. Kandori, N. Kusakabe, T. Matsuo, S. Mayama, S. Miyama, J.-I. Morino, A. Moro-Martin, T. Nishimura, T.-S. Pyo, H. Suto, R. Suzuki, N. Takato, H. Terada, C. Thalmann, D. Tomono, M. Watanabe, T. Yamada, H. Takami, and T. Usuda. Direct Imaging of Fine Structures in Giant Planet-forming Regions of the Protoplanetary Disk Around AB Aurigae. *ApJ*, 729:L17, March 2011. doi: 10.1088/2041-8205/729/2/L17.

P. Barge and M. Viton. A Dusty Vortex around KH 15D ? In J. Beaulieu, A. Lecavelier Des Etangs, and C. Terquem, editors, *Extrasolar Planets: Today and Tomorrow*, volume 321 of *Astronomical Society of the Pacific Conference Series*, page 317, December 2004.

K. M. Flaherty and J. Muzerolle. Modeling Mid-infrared Variability of Circumstellar Disks with Non-axisymmetric Structure. *ApJ*, 719:1733–1749, August 2010. doi: 10.1088/0004-637X/719/2/1733.

S. Kraus, M. Ireland, M. Sitko, J. Monnier, N. Calvet, C. Espaillat, C. Grady, T. Harries, S. Hoenig, R. Russell, D. Kim, J. Swearing, C. Werren, and D. Wilner. Resolving

the gap and AU-scale asymmetries in pre-transitional disks with multi-wavelength interferometry. In *Protostars and Planets VI Posters*, page 51, July 2013.

J. T. Rayner, M. C. Cushing, and W. D. Vacca. The Infrared Telescope Facility (IRTF) Spectral Library: Cool Stars. *ApJ*, 185:289–432, December 2009. doi: 10.1088/0067-0049/185/2/289.

W. D. Vacca, M. C. Cushing, and J. T. Rayner. A Method of Correcting Near-Infrared Spectra for Telluric Absorption. *PASP*, 115:389–409, March 2003. doi: 10.1086/346193.

M. C. Cushing, W. D. Vacca, and J. T. Rayner. Spextool: A Spectral Extraction Package for SpeX, a 0.8-5.5 Micron Cross-Dispersed Spectrograph. *PASP*, 116:362–376, April 2004. doi: 10.1086/382907.

M. L. Sitko, W. J. Carpenter, R. L. Kimes, J. L. Wilde, D. K. Lynch, R. W. Russell, R. J. Rudy, S. M. Mazuk, C. C. Venturini, R. C. Puetter, C. A. Grady, S. M. Brafford, and R. B. Perry. Time Variability of the Inner Dust Zone in Pre-Main Sequence Disk Systems. *Meteoritics and Planetary Science Supplement*, 42:5284, August 2007.